

**UNIVERSITÀ  
DEGLI STUDI  
DI PADOVA**

Sede Amministrativa: Università degli Studi di Padova

Dipartimento di Tecnica e Gestione dei Sistemi Industriali (DTG)

CORSO DI DOTTORATO DI RICERCA IN:

***INGEGNERIA MECCATRONICA E DELL'INNOVAZIONE MECCANICA DEL PRODOTTO***

CURRICOLO: ***MECCANICA DEI MATERIALI***

CICLO: ***XXXIV***

## **ENERGY PREDICTION AND MINIMIZATION APPROACHES FOR METAL FORMING AND FORGING PROCESSES**

**Coordinatrice:** Ch.ma Prof.ssa Daria Battini

**Supervisore:** Ch.mo Prof. Roberto Caracciolo

**Co-Supervisore:** Ch.mo Prof. Luca Quagliato

**Dottorando:** Irene Mirandola



# Abstract

The prediction and minimization of energy consumption have become an essential part of process planning for the XXI century manufacturing industries due to cost-saving policies and environmental regulations. The ever-growing attention on energy-saving and process optimization requires a deep analysis of the production processes to provide more accurate predictive models: every process parameter has to be studied under a magnifying lens to understand its influence on energy consumption.

Based on this background, the research work presented in this thesis is related to the development of predictive models for the estimation of the energy consumption in metals forming processes, and in particular, the study is focused on the radial-axial ring rolling (RARR) process for the production of rings. In the RARR process, the ring size varies from a few hundred millimeters to two or three meters depending on the application.

The most common applications for rings manufactured by the ring rolling process are the heavy machinery industry, wind turbine towers, and rotors and bearing systems. In addition to that, although the model presented in this research has been developed considering the ring rolling process, additional validation steps have been carried out to prove their applicability also to different metal forming processes. In fact, the developed algorithms have been implemented in such a way that they can be easily extended also to different industrial processes, even not necessarily metal forming or forging.

The research work is subdivided into various sections, as hereafter summarized. In the first section, the preliminary investigation relevant for the development of regression models, based on residual minimization, is presented and shows the limitation of this type of approach when applied to energy prediction and minimization of complex manufacturing processes involving geometrical and thermo-mechanical interaction among the considered variables. Although energy prediction models can be developed based on the first, second, and third-order polynomial equations, the number of equations terms is impractical for real industrial use, and the accuracy of the prediction drops if the model is utilized near the boundary of the training data set.

For these reasons, after this initial assessment, the focus has been shifted towards a more complex and yet more accurate model, based on artificial intelligence algorithms. To define the database to be used for the training and validation of the implemented machine learning models, radial-axial ring rolling (RARR) finite element method (FEM) simulations have been implemented in the commercial software MSC Simufact

Forming. From both setting data and results, a data set composed of 380 rows has been developed and contains data relevant for the process settings, the initial and final geometries of the ring, the considered material properties, and, as a result, the integral of the mandrel forming force over the relevant process time (FIOT).

The FIOT parameter allows assessing the amount of force impulse required during the process and has been utilized as a sort of measurement of the energy required for the forming of the ring. Up to this point the developed machine learning application has been utilized only for the reliable prediction of the energy consumption during the RARR process of flat rings and, from the results of the investigation, the Gradient Boosting (GB) algorithms, belonging to the ensemble category, showed the best accuracy being its maximum and average residuals equal to 9.03 % and 3.18 %, in a wide range of final ring outer diameters ( $650 \text{ mm} < D_f < 2000 \text{ mm}$ ). The developed model has been also validated by means of additional FEM simulations, not utilized for the training of the machine learning models, and by means of laboratory experiments, both own and from the literature. The own experiments have been carried out at the Net Shape Manufacturing Laboratory of Sogang University (Seoul, South Korea) on a small-scale ring rolling mill. The experimental verifications allowed achieving similar maximum and average residuals, proving once more the reliability of the developed GB algorithm-based machine learning solution in being able to accurately predict the energy consumption during the ring rolling process. Moreover, considering the complexity of the design and process parameters involved in the RARR process, the proposed approach can easily be extended to relatively simpler forming and forging processes, such as shape rolling, roll forming, or closed-die forging.

By means of the trained Gradient Boosting (GB) algorithm, the training database has been expanded from the original 380 rows to 760 data and utilized as training and validation data set for the second of the developed machine learning model. The aim of this second model is the minimization of the energy consumption for a specific combination of the final shape, material, and processing temperature. To prove the reliability and, at the same time, demonstrate the applicability of the proposed solution also to different manufacturing processes, the energy minimization algorithm has been also applied to the deep drawing process, in collaboration with the Sogang University, to maximize the geometrical accuracy and minimize the after-forming earing, normally caused by the wrong design of the sheet blank (preform).

As concerns the profiled ring rolling process, the academic literature on this topic, especially concerning the process set-up and control, is quite limited thus, as the first step, starting from the existing literature model for the flat ring and adapting it to the more complex profiled ring, a new analytical model for the prediction of the profiled ring evolution has been developed. The proposed model allows predicting the redistribution of the material from the original preform shape, which can be considered as a flat or an already profiled ring, and links it to the progressive variation of the ring inner and outer diameters. The proposed set-up and geometry prediction model has been validated against literature and own FEM and experimental results, showing its reliability in predicting the final geometry of the ring for a large variety of initial and final shapes, among them internal and external C-shape and L-shape rings. Subsequently, by following a similar approach to those utilized for the flat rings, the developed GB algorithm has been utilized for the prediction of the energy consumption of profiled rings.

On the other hand, as previously mentioned, the energy minimization algorithm has been applied to the flat ring rolling and to the deep drawing processes and, at the time this thesis is being written, is being validated also for the case of the profiled ring rolling process. The two completed validation, carried out on the two above-mentioned processes, allowed concluding that the implemented machine learning (Gradient Boosting, GB)-based solution is able to suggest the combination of design and process parameters that, for a specific final product, grants minimizing the required process energy, for the flat ring rolling process, and geometrical accuracy and absence of post-forming earing for the case of the deep drawing process. As concerns the energy minimization algorithm, the comparison between predicted (algorithm) and calculated (FEM) solutions showed a maximum equal to 8.95%, proving the reliability and generality of the proposed solution.



# Acknowledgments

I dedicate this space to the people who, with their support, have helped and supported me in this path of personal and professional study.

First of all, I wish to address my first thoughts to my mother, my father, and my brother who have always been close to me and who have supported me throughout my life during the difficulties. Thanks for having been always there for me.

I also would like to thank my loving partner Mattia, who has always been at my side with patience, and who gave me the strength to face the difficulties I encountered in these three years. Thanks to his unshaken support and trust in me I could reach the end of my doctorate path.

Another special thank goes to my supervisor and friend Prof. Luca Quagliato who, during these three years, guided me in my research and helped me develop the research hereby presented. Moreover, I also would like to thank Prof. Caracciolo, who gave me the opportunity of pursuing my Ph.D. and, without whose support, I would not have been able to successfully carry out my research.

I also wish to thank Prof. Naksoo Kim of Sogang University (South Korea) for his hospitality during the months I spent in his laboratory. In fact, thanks to Prof. Kim and his support I could enhance my understanding of the ring rolling process and carry out useful experiments I used in my research. At the same time, I also wish to thank all the staff of the Net Shape Manufacturing Lab of Sogang University for their kindness and especially Mr. Seungro Lee for his precious help in developing some of the algorithms relevant to my research.

Finally, I would like to thank all my friends for all the times they listened to me during these challenging years, sharing with me my success as well my concerns. Thank you for having had the strength and patience of sharing all of this with me, I love you all.





# Ringraziamenti

Questo spazio lo dedico alle persone che, con il loro supporto, mi hanno aiutata e sostenuta in questo percorso di approfondimento personale e professionale.

Come prima cosa, un ringraziamento speciale a mia madre, mio padre e mio fratello che mi sono sempre stati vicini e che mi hanno appoggiata in tutta la mia vita durante le difficoltà. Grazie per esserci sempre stati.

Ringrazio infinitamente il mio compagno di vita Mattia che mi è sempre stato accanto con infinita pazienza e che mi ha trasmesso la forza e il coraggio per affrontare le difficoltà, soprattutto nei momenti di sconforto. È grazie a lui se oggi sono riuscita a raggiungere questo traguardo.

Un altro ringraziamento particolare va al mio Supervisore e amico, il Prof. Luca Quagliato, che in questi tre anni di lavoro ha saputo guidarmi con suggerimenti pratici nella ricerca e nello sviluppo della presente ricerca.

Devo altresì ringraziare il Prof. Caracciolo che mi ha dato l'opportunità di entrare a contatto con il mondo della ricerca. Senza il suo sostegno non avrei mai potuto intraprendere questo percorso.

Voglio inoltre ringraziare il Prof. Naksoo Kim dell'Università di Sogang (Corea del Sud) per la sua ospitalità durante il mio periodo all'estero. Infatti, grazie al suo supporto ho potuto svolgere tre mesi in Corea nei quali ho approfondito, con esperimenti in laboratorio, l'argomento di dottorato ed acquisito nuove skills tecniche. Un ulteriore ringraziamento va a tutto lo staff del "Net Shape Manufacturing Lab" con il quale ho collaborato ed in particolare al mio collega Seungro Lee.

Ringrazio i miei amici per tutte le volte che mi hanno saputo ascoltare e che hanno condiviso con me gioie e fatiche. Grazie per aver condiviso con me in questi tre anni le esperienze più importanti, vi voglio bene.



# Contents

<b>ENERGY STARVATION APPROACHES FOR INDUSTRIAL METAL FORMING AND FORGING PROCESSES</b> .....	i
<b>Abstract</b> .....	iii
<b>Acknowledgments</b> .....	vii
<b>Ringraziamenti</b> .....	ix
<b>Chapter 1:</b> .....	3
<b>Research background and implementation strategy</b> .....	3
1.1 The radial-axial ring rolling process.....	3
1.2 Research implementation and topics organization strategy.....	5
<b>Chapter 2:</b> .....	9
<b>Introduction, literature survey, and research needs</b> .....	9
2.1 Flat ring rolling process literature survey .....	10
2.1.1 Process set-up and control .....	10
2.1.2 Force prediction and finite element modeling .....	12
2.1.3 State-of-the-art summary .....	15
2.2 Profiled ring rolling process literature survey .....	15
2.2.3 State-of-the-art summary .....	18
2.3 Energy prediction models literature survey.....	18
2.4 Research needs and main research achievements summary .....	19
<b>Chapter 3:</b> .....	23
<b>Process energy prediction models: application to the flat ring rolling process</b> .....	23
3.1 Process parameters identification .....	24
3.2 Flat ring rolling process set-up .....	25
3.3 Finite element model setting.....	26
3.4 Thermo-mechanical FEM models results .....	30
3.4.1 Numerical model simulation results .....	30
3.4.2 FEM validation .....	32
3.5 Multi-variable regression model evolution.....	34
3.5.1 Regression model definition.....	34
3.5.2 Model development and results .....	35
3.6 Machine learning models definition .....	38
3.6.1 Multiple Linear Regression method .....	38
3.6.2 Kernel method .....	39
3.6.3 Ensemble method .....	40
3.6.4 Neural Network method .....	42

3.7	Energy prediction model result and validation.....	43
3.7.1	Data pre-processing and machine learning algorithm training.....	43
3.7.2	Model results and validation.....	44
3.8	Chapter 3 summary and highlights.....	48
<b>Chapter 4</b>	.....	<b>49</b>
<b>Process control, geometry, and energy prediction models for profiled rings</b>	.....	<b>49</b>
4.1	Process parameters identification .....	50
4.2	Profiled ring rolling process set-up and analytical model .....	52
4.3	Finite element model implementation .....	55
4.3.1	Model setting .....	55
4.3.2	Validation of the FEM model .....	57
4.3.3	FEM investigation cases set up .....	61
4.4	FEM and model validation results.....	65
4.5	Process energy prediction for the profiled ring rolling process.....	73
4.6	Chapter 4 summary and highlights.....	75
<b>Chapter 5</b>	.....	<b>77</b>
<b>Energy minimization model development and validation</b>	.....	<b>77</b>
5.1	Definition of energy minimization model .....	78
5.2	Differential Evolution implemented method.....	79
5.3	Differential evolution model validation .....	80
5.4	Chapter 5 summary and highlights.....	85
<b>Chapter 6</b>	.....	<b>87</b>
<b>Conclusions and on-going work</b>	.....	<b>87</b>
<b>Appendix 1</b>	.....	<b>91</b>
<b>Appendix 2</b>	.....	<b>93</b>
<b>Appendix 3</b>	.....	<b>103</b>
<b>References</b>	.....	<b>107</b>





# Chapter 1:

## Research background and implementation strategy

### 1.1 The radial-axial ring rolling process

Since most of the research work is relevant to the radial-axial ring rolling process, this initial section aims to provide some basics on this process in order to enhance to understandability of the research implementation strategy, presented in the following sub-section 1.2. The radial-axial ring rolling (RARR) is a metal forming process in which a circular blank is deformed both vertically and axially for producing a variety of seamless rings with a desired final geometry and good mechanical proprieties. The process involves 4 tools, namely main roll, mandrel, axial rolls, and guide rolls, as schematically reported in Fig. 1a.

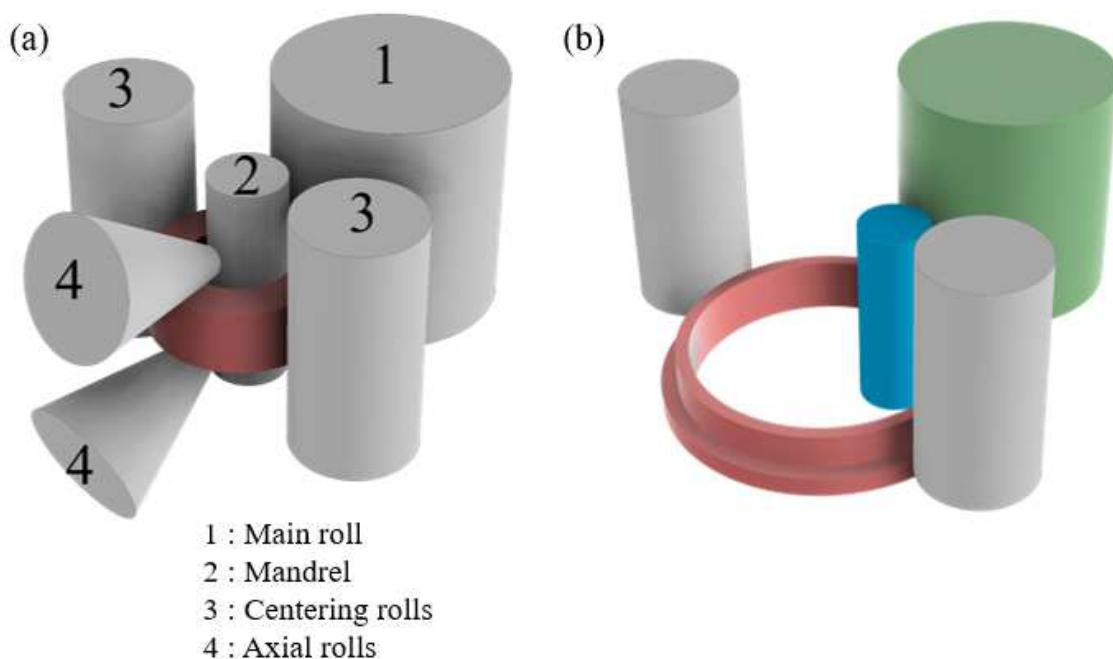


Figure 1 – (a) Flat and (b) profiled ring rolling process configuration.

The tools are common for both flat and profiled ring rolling process but, for the latter case, either the mandrel or the main roll present a non-flat (grooved or protruded) shape, which allows the creation of grooves or protrusion on the ring.

In the RARR process, the thickness of the ring is progressively reduced by the pressure of the mandrel towards the main roll, as well as the height is reduced by the vertical action of the upper axial roll towards the lower one. By means of these two deformations, both ring thickness and height are reduced, granting an enlargement in the ring diameters. It must be noted that the vertical deformation carried out by the axial rolls is not mandatory, and, in some cases, it is only employed to control the height of the ring rather than reduce it. This is particularly true for the case of the profiled ring rolling process, Fig. 1b, where the main focus is oriented towards the material redistribution from the initial ring cross-section to the final flanged shape.

The last of the tools normally available in a ring rolling are the guide rolls that help to control the circularity and keep the ring centered during the progress of the process, thus helping to maintain the stability of the ring during the process.

The RARR process allows producing flat and flanged final rings with different final shapes (e.g. flat, T-shape, L-shape, C-shape). Examples of initial ring and final rings, flat and profiled, are shown in Fig. 2.

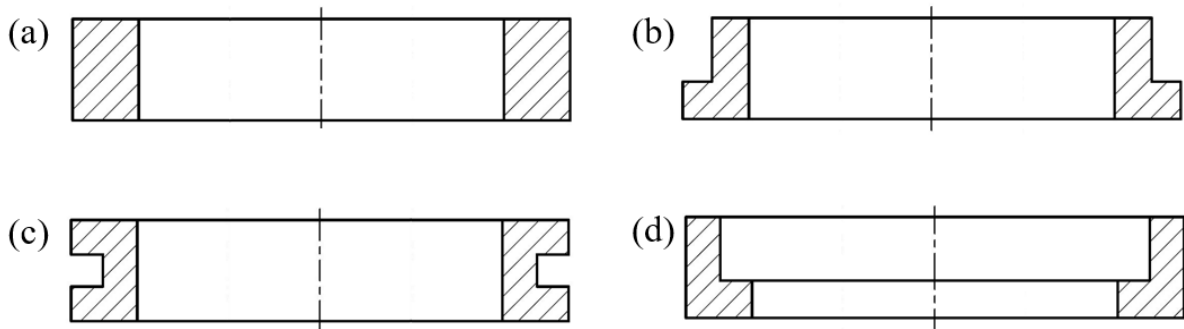


Figure 2 – Various common final (a) flat and profiled ring shapes. For the profiled rings, common final geometries are (b) outer L-shape ring, (c) C-shape shape ring, and (d) internal L-shape ring.

Due to the precise tolerance that could be obtained, rolled rings are used in different industrial fields such as automotive (e.g. bearings, automobile transmissions, gears, etc.), wind power, oil, and gas generation (e.g. flanges, valves, etc.), and aerospace with the production of aircraft turbine engine components [1, 2].

In the ring rolling process a large variety of metal alloys can be employed, such as steel, aluminum, titanium alloys, and other special alloys (such as the Inconel material) with high performances, allowing ring manufacturers high manufacturing flexibility and a quick response to the market demands.

Furthermore, the high degree of control applicable to the process through the tools of the ring rolling mill allows a high geometrical precision, reducing the cost of the post-operations [3, 4]. On the other hand, although the ring rolling process is normally carried out at a high temperature, which implies a high energy consumption for the initial heating-up phase of the ring preform, the high temperature and low processing time allow obtaining good grain microstructure (grain size pattern), thus good and uniform mechanical properties in the final component [5, 6].



## 1.2 Research implementation and topics organization strategy

This research is subdivided into several sections, which all together allowed achieving the goal of defining efficient and precise models for the prediction and the minimization of the energy in metal forming processes.

As previously mentioned, the energy prediction and minimization algorithms have been defined considering the ring rolling process but, in the final chapter of the thesis, they have been also applied to a different metal forming process (sheet metal deep drawing), showing the generality of the implemented solutions. The overall research implementation flowchart is reported in Fig. 3.

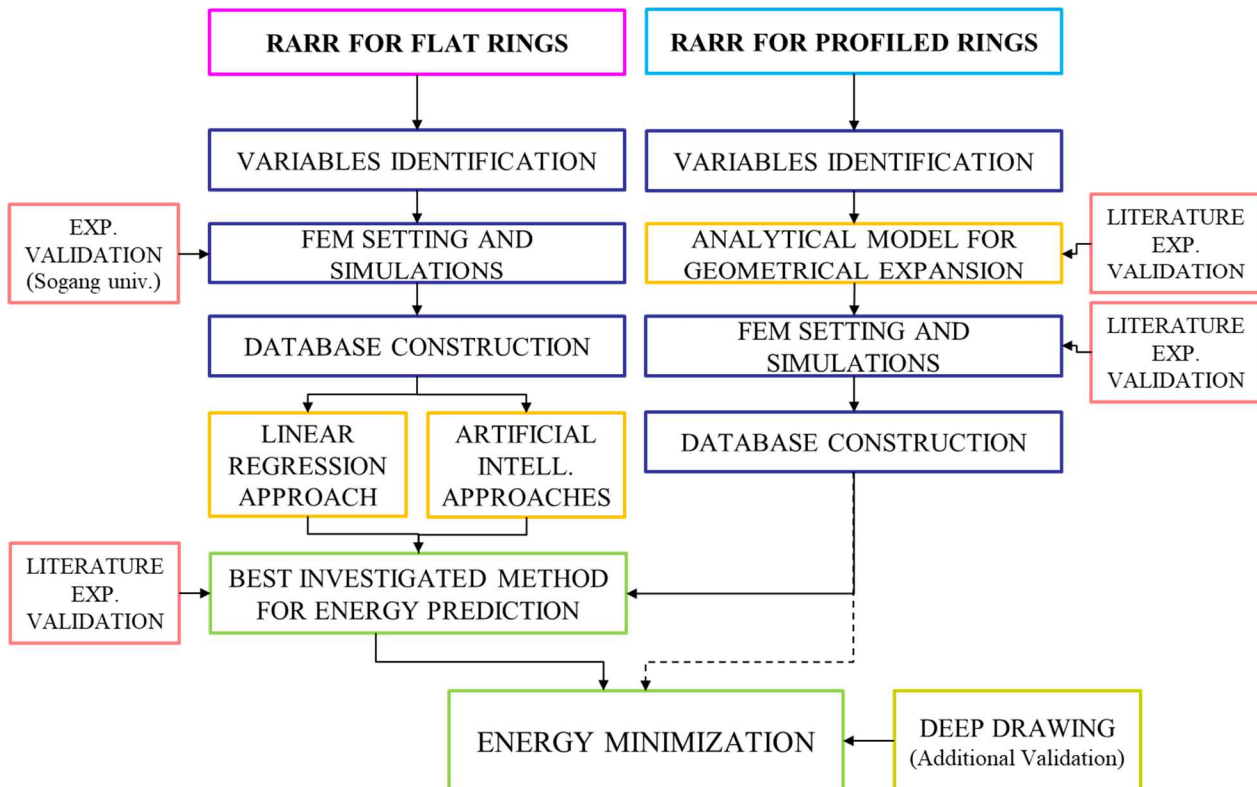


Figure 3 – Flow chart of the research.

In order to properly identify the process and design variables to consider in the variable identification phase, an extensive literature review has been carried out considering the most important contributions dealing with the ring rolling process published in the last 50 years. Considering that the different level of technology development and research contributions, flat ring rolling process and profiled ring rolling process has been analyzed in separate sections (2.1 and 2.2 respectively) to highlight the specific features of each process.

The contributions relevant for the flat ring rolling process have been organized in two different sub-sections dealing with i) process set-up and control (2.1.1) and ii) force prediction and finite element modeling (2.1.2). Since the number of research papers dealing with the profiled ring rolling process is far lower than that of the flat ring rolling, they have been organized in a single sub-section (2.2). Contributions including experimental verifications, both from lab-scale and industrial-scale, have been added in the relevant section. Moreover, since

a contribution may deal with more than one subject, for instance, analytical and FEM modeling at the same time, the organization strategy follows a chronologic and topic ordering, showing the progressive improvement in the knowledge on the considered process. At the end of each one of the two sub-sections dealing with both flat and profiled ring rolling process, a brief state-of-the-art summary has been added to show the main achievement and the main limitations relevant to the topics. In addition to the literature contributions dealing with the ring rolling process, an additional section has been added in order to summarize the state of the art for energy prediction and minimization models, focusing more on those developed and applied to the metal forming processes. As will be highlighted in section 2.3, although energy prediction and minimization algorithms have indeed been applied to metal forming processes, their application is carried out in a study case-like fashion, making it difficult to extend them to different processes or manufacturing conditions.

At the end of the literature survey chapter, a summary of the main aspects missing from the literature contribution and their link to the implemented research shall be presented, section 2.4, to enhance the understandability of the novelty of the research work as well as its applicability in both academia and industrial environments.

The following three chapters of the thesis comprise the main research topics, relevant for the development of energy prediction models for flat rings (chapter 3), the analytical model for the process set-up and control of the geometrical expansion of profiled rings (chapter 4), and the process energy minimization, applied to flat rings, profiled ring and deep drawing process (chapter 5).

In chapter 3, based on the summary of the literature investigations, the main process inputs and outputs are defined and considered throughout the chapter as variables for the developed energy prediction models (section 3.1). Afterward, an initial summary of the research work concerning the process set-up and control for the flat ring rolling process is presented (section 3.2) and utilized for the setting of the FEM simulation models, summarized in section 3.3, and implemented by means of the commercial software Simufact Forming 15. Based on the results of the implemented FEM simulations, for a total of 380 cases ranging from  $650 \text{ mm} < D_f < 2000 \text{ mm}$  ( $D_f$ : Final ring shape outer diameter), polynomial regression functions have been first defined and investigated in section 3.5, where their limitations in predicting the process energy are also highlighted. Afterward, in sections 3.6 and 3.7 the details of the implemented machine learning-based algorithms are presented, highlighting their differences and the requirement for pre- and post-processing as well as their relevant accuracy in the prediction of the integral of the mandrel forming force over the process time.

On the other hand, chapter 4 is focused on the developed analytical model utilized for the set-up and control of the profiled ring rolling process. In this chapter, the analytical formulation of the above-mentioned model is firstly presented and discussed in detail, highlighting the importance of the volume conservation principle, the main roll rotational speed, and the mandrel feeding speed on the geometrical evolution of the ring. In addition to that, the attention is also placed on the importance of the initial ring shape (preform) on the material redistribution, a fact which was also highlighted in some of the investigated reference contributions, but never explicitly clarified from an analytical point of view. At the end of chapter 4, the Gradient Boosting method,

defined in section 3 as the approach which allows minimizing the prediction errors when applied for the estimation of the mandrel forming force integral over processing time (FIOT), has been applied also to the profiled ring rolling process, allowing to prove once again its reliability in the prediction of the energy consumption. The FIOT parameter has been considered as representative of the energy trend since the force integral over time manage better the instantaneous force peaks and so avoid incorrect readings. Moreover, for developing the predicting algorithm, an average mandrel feeding speed has been considered, thus using the FIOT permits to use less variables. This second validation allows appreciating the generality of the implemented solution, which is not limited to the flat ring rolling process. Finally, in chapter 5, the model developed for the minimization of the energy consumption is firstly presented and discussed in detail and is afterward applied to the flat ring rolling and to the deep drawing process. For the first case, the target function is set to the minimization of the FIOT parameter, identified as the main source for the energy consumption in the process, for the latter case, the optimization is carried out considering the combinations of geometrical and process parameters those allow achieving geometrical accuracy of the final shape while avoiding post-forming earing in the edge regions of the part. Same concerning chapters 3, 4, and 5, due to the large amount of data and results available, only a small but still relevant fraction of the results in presented in the core of the thesis, whereas the remaining information is summarized in dedicated appendices and the end of the manuscript.

In order to provide critical insight on the main achievement and results summarized in this thesis, the detailed comments of the results are separated from the results sections of chapters 3, 4, and 5 and are detailed in section 6. In this section, the interconnections between the different aspects introduced and presented in the previous three chapters are highlighted to show how the developed algorithms and procedure can be applied alone, or combined, exploiting their features to minimize the energy consumption or, in general, to optimize a specific user-defined multi-variable target function.

Moreover, in section 6, a brief introduction of the on-going activities is presented to highlight the remaining research activities being carried out at the moment this thesis is being written and that will complete the work on the machine learning models for process optimization, defined and validated for the flat ring rolling process and the deep drawing process in section 5.



## **Chapter 2:**

### **Introduction, literature survey, and research needs**

Radial axial ring rolling process is a versatile forming process that allows producing annular-shaped products as well as profiled rings: this advanced process permits to realize a seamless product, shorten the production time of large-scale rings compared to other process solution, and control orientation and size of the grain to obtain improved mechanical properties [3-6]. Components manufactured with the RARR process are used in the last years in several industrial fields such as automotive, wind power, aerospace, agriculture, and piping [1, 2]. Therefore, to satisfy the growing market demands, several researchers investigated procedures and methodologies to optimize this complex process, in terms of tolerances, surfaces quality, mechanical properties, production cost, and time. These topics are discussed in the relevant sub-sections, both concerning the flat ring rolling as well as the profiled ring rolling process.

Furthermore, the constantly growing computational power and the developments of various numerical simulation software aided the ring rolling process research, allowing to obtain advantages of time and cost compared to the experimental tests. In fact, finite element method (FEM) simulations allow studying the evolution of the ring and to analyze the working forces during the process time for different process configurations and are far less expensive than industrial-scale or lab-scale experiments. For these reasons, several authors also developed ad-hoc simulation programs based on both standard finite element theory or developed analytical models to study the ring evolution in the pre-production phase as well as the optimal working conditions with the aim to minimize the production defects and enhance the production performances.

In the following paragraphs, a summary of the present literature concerning the flat and profiled ring rolling process aims to provide an overview of the available knowledge on process set-up, control, FEM, and force modeling for these processes, aiming to highlight the state-of-the-art and, at the same time, the areas where more studies ought to be focused. In addition to that, the following two sections are dedicated to two additional topics related to this research, namely the energy prediction models and machine learning models. For the

former, a broad literature review has been carried out in order to investigate the available literature modeling procedures and algorithms, even not strictly related to industrial forming processes. The latter sub-section is, instead, dedicated to the summary of the available categories of machine learning models to present their strengths and weaknesses and also to provide an overview of the state-of-the-art of their applications into manufacturing processes in general.

## 2.1 Flat ring rolling process literature survey

In this section, the main contributions dealing with the ring rolling process of flat rings are summarized starting from the most iconic and cited ones, on which most of the following contributions are based. In addition to that, also the most recent and most industrially relevant contributions are summarized as well. This section aims to provide a clear background on the RARR process of flat rings, which is also subsequently summarized in the last section 2.1.3.

### 2.1.1 Process set-up and control

The starting point for the modeling of the process control in the ring rolling process is most likely the work of Hua and Zhao [7] from 1995, where the penetration and biting-in conditions have been defined. The penetration conditions are regarded as the minimum thickness draft that is required to be applied to the ring thickness in order to achieve plastic deformation throughout the whole thickness. On the other hand, the biting-in conditions defined the other extreme of the range, thus the maximum thickness draft that can be applied to the ring, beyond which the friction force becomes too high, and the ring is stuck into the deformation gap.

From the kinematic point of view, the plastic deformation through the thickness of the ring has been investigated by several authors by means of the slip line theory [8], a powerful mathematic tool that allows calculating the force required to deform a bulk material section based on a specific set of material, geometrical and velocity boundary conditions. By means of the slip line theory, firstly Mamalis et al. [9] and, more recently Quagliato and Berti [10, 11] defined analytical models for the estimation of the strain field distribution in the cross-sections of flat rings with the aim of calculating the process force evolution throughout the process, on the basis of the material properties, considered as perfectly plastic, and the process parameters, mainly in terms of velocity field and mandrel feeding speed (thickness draft per ring revolution).

Based on the initial modeling proposed by Hua and Zhao [7], several authors proposed improvements and further expanded it considering the mutual influence between radial and axial deformations, as hereafter summarized. Yan et al. [12] defined an algorithm for the definition of the mandrel feeding speed during the process based on a pre-selected ring growth speed, with the aim of maximizing productivity while reducing forming defects, such as the fishtail effect [13]. Subsequently, Guo and Yang [14] presented the first contribution dealing with the steady forming conditions for the radial-axial ring rolling process and introduced a process control algorithm that allows calculating the process parameters that grant a constant growth of the ring throughout the process. It is important to remark that, to achieve stability during the ring rolling process,

after the initial phase in which the ring is put into a steady rotation by the main roll, the expansion of its diameters should follow a quasi-linear law. This steady forming condition allows achieving a uniform redistribution of the material in the cross-section as well as avoids instability problems, such as the lack of circularity of the ring or excessive dynamic instability (ring oscillation and vibrations).

Up to 2011, the most complete contribution concerning the development of algorithms for the set-up of the flat ring rolling process is due to Zhou et al. [15]. In their contribution, a clear correlation between the mandrel feeding speed and the upper axial roll feeding speed was established, allowing the definition of a range for the mandrel feeding speed and based on it, the calculation of the feeding speed range for the upper axial roll. Although this contribution defined the starting point of the identification of the so-called feasible ranges for the main process parameters in the ring rolling process, the consideration of a constant feeding speed for the mandrel remained a strong limitation. In fact, considering a constant mandrel feeding speed during the ring rolling process neglects the intrinsic temperature loss and relevant increase in the material flow stress of the ring, a fact which makes the maximum force to be reached towards the final stages of the process, where the ring should have already reached a shape close to its final one. To avoid this inconvenience, Berti and Quagliato proposed a methodology that defines two different feasible ranges for the mandrel feeding speed, one for the onset velocity and one for the final velocity, interpolated considering a linearly decreasing law [16]. This innovative approach allowed overcoming all the limitations of the previous models, allowing a steady growth of the ring during the process. In addition to that, the application of a higher mandrel feeding speed at the beginning of the process allows achieving most of the deformation in the first rounds of the process thus maximizing the exploit of low material flow resistance granted by the higher ring temperature. On the other hand, the progressive reduction of the mandrel feeding speeding allows following the natural decrease in the ring temperature and the consequent increase in its material flow stress. The algorithm proposed by Berti and Quagliato has also been utilized in the following research [17] to determine the evolution of the 3D strain field in the ring throughout the ring rolling process. The consideration of the evolution of the 3D strain tensor during the process allows recalculating the material redistribution in the ring cross-section, enhancing once more the capability in the estimation of the ring geometrical evolution during the process.

As far as concerns the set-up and control of the flat ring rolling process, the analytical model proposed in Berti and Quagliato [16] still represents the state-of-the-art and, for this reason, it has been utilized also in this research for the set-up phase of the FEM simulations utilized for the creation of both training and validation data sets utilized for the energy prediction and minimization algorithms.

For the sake of enhancing the understandability of the developed models, the main equations relevant for the above-mentioned model [16], both in terms of estimation of the ring initial preform and the calculation of the main roll, mandrel, and upper axial roll speed ranges, are summarized in section 3.2.

### 2.1.2 Force prediction and finite element modeling

As concerns analytical modeling for the estimation of the process force and torque in the ring rolling process, some work has been carried out in the '70s of the previous century and, more recently by two different research groups. The reason for this relatively low number of contributions on the analytical modeling for the force and torque is given by the widespread use of FEM simulations, starting from the early '80s onwards, which made the estimation of these parameters easier and somehow more reliable. However, as will be also highlighted in this section of the thesis, an accurate estimation by FEM simulations requires an intensive pre-processing phase, to properly set-up the FEM model, apply to correct process set-up and boundary conditions as well as temperature- and strain rate-dependent material properties. In fact, the utilization of FEM simulations for the estimation of the process in metal forming processes, and especially in the RARR process, is a double edge sword. On one hand, several important process outputs, such as ring geometry, strain field, stress field, process force, and torque, and so on can be estimated with exceptional accuracy but, on the other hand, this accuracy is strongly connected to a remarkably high computational time. If some simplifications are applied to the FEM model to reduce its computational time, or ad-hoc FEM solutions are implemented with the aim of reducing the number of equations to be solved by the FE solver, the resulting accuracy is not far from that of an analytical solution which is, instead, computed in real-time.

In a 1973 work, Hawkyard [18] developed an analytical model, translated into operating charts, which linked the projected contact length between the ring and forming tools with the forming force and the rolling torque, parameterized with respect to the yield strength and by considering a perfectly plastic material. The implemented solution is based on the slip line field theory and allows a direct estimation of the radial force and torque, with a maximum deviation calculated in 15%, in comparison to the relevant lab-scale experiment.

In a following work, Yang and Ryou [19, 20] investigated the influence between the radial forming force and the torque transferred from the main roll to the ring during the process by defining an equivalent coefficient of friction. Afterward, they defined a upper bound correlation between radial force, torque, and equivalent coefficient of friction and investigated its influence on various ring shapes, and considering different process parameters. More recently, Parvizi et al. [21] and Parvizi and Abrinia [22] utilized a SLAB analysis and the Upper Bound method for the estimation of the radial forming force in the ring rolling process and validated them by comparing their results with those of FEM simulations and experiments. It is interesting to notice that both SLAB and Upper Bound models should define a sort of safe / non-safe region around the true solution but, as shown in Quagliato et al. [23] both solutions tend to strongly underestimate both experimental and FEM results when applied to relatively large-scale rings. This fact has been investigated in Quagliato [23] where the reason for the underestimation of the radial forming force has been identified in an underestimation of the contact length between mandrel, main roll, and the inner and outer diameters of the ring, a fact which makes the solutions estimated in [21, 22] to underestimate the real force values.

Another interesting aspect is related to the fact that, in the literature, only two contributions seem to deal with the estimation of the axial forming forces. In the considered work by Wang [24] the Keaton's rule [5]



correlating the radial and axial deformations, in terms of thickness and height drafts, has been considered to define an analytical model for the prediction of the axial forming force. The results of this investigation seem to predict a sort of lower bound of the axial forming force but, as also mentioned in the paper, they tend to underestimate the experimental results. In addition to that, the second contribution dealing with the estimation of the axial forming force is due to Kalyani et al. [25] and presents an algorithm, based on the SLAB method, for the estimation of both contact length between axial rolls and the ring and another one for the analytical estimation of the axial forming force. The prediction carried out by the former algorithm has been compared with the experimental results of a specific study case showing a deviation in the estimation of the maximum axial force equal to 16.9%. However, as demonstrated in Quagliato and Berti [26], both algorithms presented in [24] and [25] are affected by the same issue related to the estimation of the contact length and, for this reason, they both tend to underestimate the forming force. For this reason, in [26], Quagliato applied the slip line field theory for the estimation of the axial forming force and shown that, as was also true for the radial forming force, also for the case of the axial force the correct estimation of the contact length between the forming tools and the ring is the key aspect in the accuracy of the force estimation.

As concerns FEM modeling of the radial-axial ring rolling process of flat rings, both commercial software, as well as dedicated solution algorithms, have been developed over the years to achieve both accuracy in the prediction as well as reductions of the computational time. Since these two aspects are normally in conflict with each other, authors have concentrated either on high prediction accuracy or on computational time reduction, as hereafter summarized.

As concerns the utilization of commercial software, Qian and Pan [27], Qian et al. [28], and Zhou [29] developed finite element method (FEM) models employing the ABAQUS/Explicit environment and coupled these numerical investigations with laboratory experiments and analytical models. The target of the developed models was to investigate specific interactions between the process tools and the ring during the process, such as the blank size (ring preform) effects [28] or to investigate the heating process of the ring preform from the initial blank operation to create the inner diameter to the end of the ring rolling process (multi-stage finite element analysis). On the other hand, ABAQUS/Explicit has also been utilized by Guo and Yang [14] for the validation of the developed analytical model, showing good agreement between these two solutions.

In an interesting work focused only on FEM modeling, Wang et al. [30] defined an approach for the optimization of the flat ring rolling process based on a numerical solution that optimizes the control parameters for the ring rolling mill and obtained a reduction in the rolling time equal to 28% in comparison to traditionally employed approaches. Considering a different commercial software, Sun et al. [31] developed a thermo-mechanical FEM simulation model in DEFORM-3D and investigated the effect of the process parameters on the quality of the resulting ring and the expansion dynamic of the process, in terms of its stability. The main target of this research was the definition of the optimum process parameters in the flat ring rolling process.

It is important to highlight that, although the process optimization can be carried out by means of FEM simulations, an initial pre-screening operation by means of analytical models is required to limit the overall

computational time. If this initial pre-operation is not carried out, the time required to achieve a reasonable improvement in comparison to the starting point of the optimization becomes a strong limitation for academic research and, especially, for an industrial environment. A similar investigation on the effect of the process parameters on the strain field distribution in the ring during the process has been carried out by Zhou et al. [32] but, although accurate, it is affected by the same drawback relevant to the computational time.

On the other hand, in an interesting work by Zhou et al. [33], the effect of the axial rolls on the process stability has been investigated and some process control rules have been proposed. The role of the axial rolls in the rolling process is not to apply deformation to the ring but, instead, to control the overall stability of the process. For this reason, since the analytical modeling of this interaction is not simple, FEM models provide useful insight on the dynamic of the process and cast light on some aspects that can be employed in the real production for an improvement of the control of the process.

In addition to the two commercial FEM software mentioned above, the Simufact Forming program has been utilized throughout the years by several scholars in relation to the ring rolling process [10, 11, 16, 17] and also other for other application of forming, welding and additive manufacturing [34-41] thanks to its accuracy as well as for the powerful explicit solver (based of the MARC® architecture). For this reason, as also carried out in previous researches, this commercial simulation software has also been utilized for the implementation of the FEM simulations implemented in this research.

As concerns more customized finite element approaches, Lim et al. [42] employed a material mesh and a computational mesh system in which the former is only utilized to transfer the node-based information from a time step to the following one whereas the latter is used in the actual computations. The consideration of the material mesh allows limiting the number of computations carried out at each integration step since it considers only the region of the ring where the deformation is carried out, either in the main roll-mandrel or in the axial rolls deformation gaps. Although this approach is promising, the pre-processing operation and the actual programming required to properly compute both mesh systems in all the integration steps limits the applicability of this approach to most of the users.

In addition to that, Davey and Ward [43] introduced the possibility of remeshing the portion of the ring not subjected to deformation in the considered integration step with a coarser mesh, and to remesh them with the original fine mesh right before they enter the deformation gap. A similar approach has also been employed by Kim et al. [44], obtaining some reduction in the computational time but the procedure tends to achieve lower accuracies for high rolling velocities. This fact can be explained by the intrinsic nature of the explicit solver solution, where the time step selection is related to the inputted speeds. For the case of the ring rolling process, the main driving force is related to the rotational speed of the main roll, thus a higher value of this parameter requires a lower time step setting. For low time step values, the time required for the remeshing of the regions of the ring not directly subjected to deformation in the considered time step requires more time than the time step itself, making this approach to become impractical.

In addition to that, Yea et al. [45] and Kim et al. [46] introduced the self-developed program SHAPE-RR® and compared its performances, both in terms of estimation of the process forces and computational time, with the results of other commercial software showing the improvement. More specifically, in [46], the authors developed a specific plug-in for the developed SHAPE-RR® software to automatically calculate the process parameters that allow minimizing the maximum forging load. The procedure is based on the combination between FEM simulations and DoE analysis, based on the Taguchi technique and shown to be able to provide a solution that is in good agreement with the experimental results and, at the same time, allows a reduction in the maximum mandrel force.

### 2.1.3 State-of-the-art summary

As summarized so far, in the last five decades, the ring rolling process of flat rings has been extensively analyzed by different scholars from the analytical, finite element, and experimental points of view. At the present stage, as pointed out in the contributions of Berti and Quagliato [16], the radial-axial ring rolling process of flat rings can be set-up with relative ease and the influence of the chosen process parameters on the geometrical evolution as well as on the strains and forces developing during the process can be assessed via an accurate analytical solution. In addition to that, as pointed out in Quagliato [23, 26], the analytical estimation of the process forces, both radial and axial, is strongly influenced by the accurate estimation of the contact arc length created between the tools and the ring during the process and can be estimated by the slip line theory, as largely discussed in [11]. For these reasons, considering the extensive research work carried out between the years 2000 and 2018, no new contributions dealing with analytical modeling for the flat ring rolling process are available in the literature. On the other hand, finite element simulations still remain a useful, yet high time-consuming technique, for the analysis of the variable involved in the ring rolling process and, for this reason, several commercial software are employed both in the academia as well as in the industry for the thermo-mechanical process investigation.

## 2.2 Profiled ring rolling process literature survey

The aim of this section is remarkably different from that of the flat rings, as hereafter explained. Most contributions dealing with the profiled ring rolling process aimed to the investigations of the variation of the ring geometrical expansions when different combinations of process parameters are applied to the forming tools, mainly the main roll rotational speed and the mandrel feeding speed. The reasoning behind this case study-like is given by the fact that no contribution deals with the kinematic analysis of the influence of the process variables onto the geometrical expansions of the ring. For this reason, one of the main efforts of this research has been the definition of an analytical model able to define a correlation between these two above-mentioned inputs and output of the process. On the other hand, the presence of several scholars dealing with experiments relevant for the profiled ring rolling process allowed verifying the proposed model with respect to various geometrical and material configurations, allowing to strengthen its generality and reliability.

Finally, being the literature contributions dealing with the profiled ring rolling process far less than those relevant for the flat ring rolling process they are all summarized in this section of the paper and are not separated into specific sub-sections.

The first contribution investigating the profiled ring rolling process dates back to 1976 and is due to Mamalis et al. [47]. In their research, the authors investigate the effect of the rolling parameters on the spread of rings manufactured by employing tellurium lead and aluminum alloy. The extensive work allowed showing the plastic flow pattern in the cross-section of the manufactured rings and showed that the slip line field, estimated by the implemented algorithm, and also considered in previously mentioned researches [7, 9, 10, 11] is able to properly predict the real redistribution of the material in its cross-section.

As concerns additional analytical investigations, Zhou investigated the expansion of profiled rings by defining an algorithm for the prediction of its wall diameter, identified as the portion of the ring where the deformation is applied in the mandrel-main roll deformation gap. Although the charts showing the comparison between experimental and FEM ring growths show a reasonable accuracy, the evolution of the inner diameter of the ring as well as of the flange diameter are not discussed and a quantitative investigation of the model accuracy is not provided. On the other hand, Qian et al. [48] investigated the above-mentioned penetration and biting-in conditions for the case of a C-shape (Fig. 2c) grooved ring and showed that the balance between penetration and sufficient ring rotation, also valid for flat rings, is a key aspect in the uniform growth of both wall and flange of the ring.

Besides, most of the relatively recent contributions dealing with the profiled ring rolling process deal with a combination of FEM, analytical-empirical and experimental analyses, as hereafter summarized.

In an interesting work from 2014, Berti and Monti [13] considered the whole operations required for the production of an industrial case relevant for a profiled ring and optimized both the initial piercing operation of the annular blank, namely the initial shaping into the profiled preform, as well as the profiled ring rolling process by means of simulations implemented in the commercial SW Simufact Forming. Besides, Hua et al. [49] utilized the commercial SW ABAQUS for the investigation of the deformation behavior of outer L-shape rings (Fig. 2b) and showed that the plastic deformation is not uniform in the cross-section of profiled rings but, instead, it propagates from the outer-top and -bottom surfaces to the center of the ring. Differently from the flat ring rolling process, in the profiled ring rolling the presence of one or more protrusions in the flanging tools, makes the strain, and stress fields, to be non-uniform along the ring cross-section as well as along its height. This issue makes it difficult to predict the plastic material redistribution in the cross-section of the ring but, as it will be shown in section 4 of the paper, it has been successfully modeled in the proposed algorithm.

As concerns finite element modeling of the profiled ring rolling process, in an interesting contribution due by Kim et al. [50] the MSC SuperForm commercial software has been utilized for the investigation of the evolution of the cross-section of profiled rings showing its progressive evolution in a sort of flower-pattern, showing good agreement with the relevant experimental results. In addition to that, Davey and Ward [51] employed an arbitrary Lagrangian-Eulerian update strategy combined with the successive preconditioned

conjugate gradient method in order to reduce the computational time required for the solution of profiled ring rolling FEM models. As also carried out by the same authors in a contribution dealing with the flat ring rolling process [43], also in this work the authors subdivided the ring into two sections: the section being deformed in one of the two deformation gaps, and the section simply rotating. For the former section, a finer mesh is applied in order to estimate accurate results whereas in the latter a coarser mesh is considered in order to reduce the computational time. Although the implemented solution is in good agreement with the literature experimental results considered in the paper, the complexity of the profiled ring rolling process, in comparison to the flat one, makes the reduction of the computational time to be lower than expected.

In recent years, Cleaver et al. [52-55] employed low flow resistance alloys and clay materials in lab-scale experiments in order to investigate the deformation behavior of profiled rings and also to define process guidelines to apply to industrial processes. Most of the work is based on well-detailed experiments and, for this reason, some of the experiments included in the above-mentioned contributions have been utilized in this research for the validation of the profiled rings geometry prediction algorithm presented in section 4.

Furthermore, additional work has been carried out in the direction of optimizing specific industrial processes, in a case-study research approach, as hereafter summarized. Oh et al. [56] investigated, by means of both experiments and finite element simulations, the main defects arising in the profiled ring rolling process, such as ring undergrowth and lack of filling in certain regions of the final shape. Park et al. [57] investigated the effect of the process parameters and initial blank shape on the production defects of an L-shape ring utilized in construction machines. Besides, Lee et al. [58] utilized a case study, based on an excavator idle rim, to define a methodology for the multi-stage profiled ring rolling process. This concept of subdividing the process into several stages has been also investigated by Kim and Quagliato [59] for the case of the flat ring rolling process with the aim of achieving different expansion growth rates during the same ring rolling process. The possibility of utilizing different tools during the same process is interesting, since it allows a progressive shaping of the profiled shape of the ring, but its complexity is beyond the scope of the present research since aspects related to re-heating and microstructure changes cannot be neglected. More recently, Liang et al [60] investigated the influence of the preform definition for C-grooved rings to obtain a precise forming and defined a correlation with the so-called pulling coefficient.

Same concerning case studies relevant for the profiled ring rolling process, Tani et al. [61] investigated the geometrical evolution of a profiled Ti-6Al-4V ring utilized in a turbo fan engine. Thanks to the implemented case-study analysis the authors could achieve a higher net-shape dimensions accuracy as well better mechanical properties by controlling the process parameters and their influence on the microstructure.

Finally, as concerns contributions mainly dealing with profiled ring rolling process control, Li et al. [62] investigated the role of the axial rolls in the profiled ring rolling by means of FEM simulations implemented in ABAQUS/Explicit and defined a plug-in algorithm which calculated the instant position of the guide rolls during the process in order to be always in contact with the ring, thus enhancing the process stability and geometrical accuracy. On the other hand, Kang [63] investigated the role of the ring preform in the

filling/unfilling behavior of profiled rings and showed that the design of the initial ring preform is essential to achieve the desired final shape and avoid process defects.

As concerns this last statement, although the initial preform shape cannot be excluded from the parameters influencing the geometrical accuracy of the final ring shape, as it will be shown in section 4, the influence of the process parameters, in terms of main roll rotational speed and mandrel feeding speed, is far greater. In fact, if the initial ring preform is reasonably designed, the required geometrical accuracy can be achieved by a careful selection of the above-mentioned process parameters.

### 2.2.3 State-of-the-art summary

As summarized in the previous sub-section, most of the contributions dealing with the ring rolling of flat rings are based on experimental results and can hardly be extended to different processes if the geometry or the process/material variables are changed. In addition to that, although some authors defined the main process and geometrical variables influencing this process, a clear and quantitative connection between these two aspects is yet to be properly established. For this reason, in this research, an analytical model for the estimation of the geometrical evolution of profiled rings is proposed and validated by comparing its prediction with those of literature experiments [51, 55, 56, 63]. In addition to that, thanks to implemented analytical and FEM solutions, the influence of the main process and ring dimensions (initial and final) on the geometrical evolution and on the energy consumption during the process have been investigated as well.

This combined analytical-FEM investigation shall cast the light on the strong influence that processing parameters have on the geometrical evolution of the ring during the process which has shown to be almost independent of the considered material, making the kinematic assumption, on which the model has been developed, to be reasonably true.

## 2.3 Energy prediction models literature survey

As concerns energy estimation and starvation algorithms for industrial processes, due to the strong influence of the energy demand on production planning and control [64], several authors focused their attention on methods for the estimation and the minimization of the energy consumption, as hereafter summarized. Unver and Kara [65] introduced a decision support tool called HORUS 5.0 to determine the lowest energy-consuming route within the scope of sustainable energy efficiency. Meissner et al. [66] developed an indicator system considering the impact of the materials, energies, and economic attributes of energy efficiency, concluding that, in the manufacturing sector, strategic decision-making concerning energy optimization is important to be competitive. Hasanbeigi et al. [67], worked on the estimation of the cost of the energy consumption considering a constant energy price to overcome day-by-day energy cost fluctuations.

As concerns energy estimation in forming and forging processes, Larkiola et al. [68] investigated the role of energy efficiency in the rolling processes using an ANN-based approach. The application of this method allowed achieving an improvement estimated in 1.8% of the overall energy efficiency. Giorleo et al. [69]

compared simulation analyses with an industrial case to evaluate the effect of utilizing different ring preform geometries with the aim of reducing the total energy required during the process. However, the analysis is based on a single set of material properties and process parameters, thus the applicability of this procedure to other cases is not certain and is more focused on the fishtail defect and the material scrap reduction rather than on the energy estimation. In addition to that, Xinglin et al. [70] established a model for optimizing the feed trajectory based on the necessity to reduce surface defects for Inconel 718 alloy rings and established a model based on the surface response method (RSM). Allegri et al. [71] defined a main roll speed law that allows maintaining a constant ring angular velocity and, by means of the developed procedure, achieved a 35% reduction of the fishtail defect and a 9% reduction of the energy consumption.

In addition to that, in recent years, machine learning and deep learning algorithms have been utilized for data monitoring, collection, and energy forecasting in the manufacturing sector in order to optimize decision-making strategies [72] and to develop and improve manufacturing plants towards the so-called smart factory systems [73]. More specifically, Nguyen [74] applied an archive-based micro-genetic algorithm (AMGA) for the minimization of the energy required for the machining of the SKD61 material while also considering the influence of the adopted process conditions on surface roughness and production rate. Same concerning the machining process, Brillinger et al. [75] applied three different machine learning models, belonging to the ensemble category, namely the Decision Tree, the Random Forest, and the Boosted Random Forest, for the energy prediction during the process and verified the deviations by comparisons with predictions with industrial and experimental results. Geng et al. [76] applied machine learning algorithms, combined with interpretative surface structural and analytic hierarchy process, for the reduction of the energy consumption in ethylene production, showing good agreement with experimental results.

Finally, Wang et al. [77] developed and applied a novel extreme learning machine integrating Monte Carlo algorithm for the prediction and maximization of the energy production in hydropower plants, showing how a relatively small initial data set can be expanded by the utilization of a well-trained algorithm, in a sort of a two-stage machine learning models application. This approach has been also utilized in this research, as it will be presented in section 5.

## 2.4 Research needs and main research achievements summary

Considering altogether the literature review presented in the previous four sub-sections, some important remarks must be pointed out, as hereafter summarized.

- As concerns the flat ring rolling process, although several contributions deal with the process set-up and control and with the energy prediction, almost all of the contributions dealt with the development of FEM models, which are complex to set-up and are high time consuming;
- In addition to that, from the extensive literature review presented in this chapter, no contributions seem to deal with the utilization of machine learning models for the prediction of the energy consumption neither in the ring rolling process nor in other metal forming processes;

- No contributions deal with analytical modeling of the correlation between process parameters and kinematic expansion of profiled rings. This is a considerable issue, which affects the accuracy of the process set-up and limits the possibility of a deep and thorough understanding and control of the process;
- Finally, when it comes to energy minimization, most of the models available in the literature have been developed considering either a specific process or a quite narrow process variable range and, for this reason, as also stated by the authors, they are not easily applied to different manufacturing conditions or different processes.

These issues and missing investigations from the literature have been successfully overcome in the research topics presented in the following sections of the paper and allowed:

- Proving the limitations of the utilization of polynomial regression function when utilized for the prediction of parameters relevant for complex thermo-mechanical process, such as the ring rolling process;
- Investigating the accuracy of different machine learning models, based on different target functions and learning techniques, in predicting one or more process variables for the case of complex thermo-mechanical process, such as the ring rolling process;
- Enhancing the understanding of the kinematic correlation between process conditions and geometrical expansion of the ring in the profiled ring rolling process. As it will be shown in section 4.4, the importance of this aspect is strongly related to the connection between the main roll rotation, the mandrel feeding speed, and the redistribution of the material in the cross-section of the ring during the process, which ultimately influences its final geometrical accuracy;
- Defining a machine learning model which can automatically augment its training dataset but employing a prediction algorithm, as the first stage, and afterward predict a combination of geometrical and process parameters those allow minimizing the required process energy when a certain combination of final geometry, material, and initial temperature are considered. Concerning this last point, in order to prove the generality of the proposed approach, the developed prediction-minimization algorithm has been applied to i) flat ring rolling, ii) profiled ring rolling, and iii) deep drawing process showing its accuracy and generality, thus superseding the limitations of the previous models available in the literature.

The main research achievement, and relevant performances, of the developed models and methodologies presented throughout the paper, can be summarized as follows:

- The investigation of the performances of various machine learning models in predicting the mandrel force integral over time allowed concluding that the Gradient Boosting method, when



applied to the flat ring rolling process, has a maximum and average errors equal to 9.03% and 3.18%, both when applied to FEM and experimental results not utilized during the training phase;

- The developed process set-up and control algorithm, developed for the profiled ring rolling process, allows precise estimation of the material redistribution in the cross-section of rings during the process and, at the same time, it allowed understanding the importance of each one of the main process parameters on the geometrical accuracy and energy consumption during the process. As concerns the developed model, the accuracy has been estimated in 4.9% as the maximum error in the estimation of the three main diameters of the considered profiled rings, namely inner diameter, wall diameter, and flange diameter;
- Thanks to the generality of the formulation of the developed process variables minimization algorithm, the energy consumption (in terms of FIOT parameters) for the flat and profiled ring rolling process, and the manufacturing quality (in terms of after-forming earing) for the deep drawing process could be optimized and showed the applicability of the developed solution to a generical metal forming process for the optimization of one or more process variables. In order to assess the accuracy of the predicted solutions, the results have been compared with FEM results showing maximum deviations equal to 8.95%. In addition to that, additional FEM analyses have been carried out in order to verify that the estimated combination of geometrical and process parameters, as estimated by the minimization algorithm, is the real minimum of the considered target function. This second analysis allowed concluding that the implemented solution is indeed capable of finding the minimum of the considered target function, for both the FIOT values (flat and profiled ring rolling) as well as for the deep drawing process, in terms of post-forming earing minimization.



## Chapter 3

# Process energy prediction models: application to the flat ring rolling process

In this chapter, a deep analysis of the process parameters involved in the ring rolling process of flat rings and on the geometrical evolution of the ring is presented with the aim of defining their influence on energy consumption. Afterward, different predictive models based on different approaches, mainly regression polynomial functions and machine learning, are going to be presented in order to define the optimal industrial solution to analyze and minimize the energy consumption in the ring rolling process of flat rings.

In the RARR process, a preform is incrementally deformed for achieving a desired final ring. For obtaining a better precision of the final shape in terms of geometrical accuracy it is important to choose input for the process, mainly in terms of geometrical and process parameters. The literature algorithms concerning the choice of initial size and the calculation of the motion law ranges have been considered as the starting point for developing the energy consumption prediction model. In fact, in the first step, the correlation between process and geometry parameters has been studied for understanding the inputs to be considered in the model to obtain the desired output. FEM simulations of the RARR process with different conditions have been set, run and post-processed, to construct a database of values used in this analysis. The FEM model for the flat ring RARR process has been validated using a previous experiment test made in Sogang University.

Once the inputs have been chosen, the first developed model presented is multi-variable regression, a statistical approach. This approach permits to predict the values of dependent variables based on the value of an independent variable, as it will be explained in detail in the specific paragraph 3.2. For the validation, the results of the regression model have been compared with the solutions provided by FEM simulations. The resulting equation presents an average deviation between predicted and measured results of 5.9%. The built regression model can have an industrial application for energy starvation, but it is limited to the small range set of parameters utilized for the development. To amplify the input parameters ranges it is necessary to rebuild

the regression equation and so provide a new regression model: in this way also the model complexity augments, making the model hard to use. For this reason, different approaches based on artificial intelligence have been considered in order to increase the input range, defined in terms of the geometrical shape of the final ring, also considering the average and maximum prediction error within the considered range.

The training database considered for the energy prediction models is composed of 380 FEM simulations constructed considering a 650 mm < DF < 2000 mm range for the outer diameter of the final ring shape. In order to perform a reliable validation of the performances of the implemented prediction models, 80% of the 380 results have been utilized for the training whereas the remaining 20% for its validation.

In section 3.5 the polynomial regression function utilized has been presented whereas in the following section 3.6 the eight considered machine learning models have been summarized. The accuracy, advantages, and limitations of both formulations are discussed within the above-mentioned two sections.

### 3.1 Process parameters identification

The first step of this research is the identification of the significant process variables of the RARR process of flat rings: the following selection of process parameters has been focused and designed specifically for the energy predictive model development, meaning that for a different investigation different set of variables could be more relevant. Considering the flat ring rolling process, the process variables identified can be subdivided into 4 macro groups that are the speed parameters SP, initial and final ring geometries RG, material properties MP, and process condition PC as resumed in Fig. 4.

#### Model input for flat ring model

<p>i) <b>Initial/final Speed parameters (SP)</b></p> <ul style="list-style-type: none"> <li>- Main roll rotational speed;</li> <li>- Mandrel feeding speed;</li> <li>- Upper axial roll feeding speed;</li> <li>-</li> </ul>	<p>iii) <b>Initial/final ring geometries (RG)</b></p> <ul style="list-style-type: none"> <li>- Inner diameter;</li> <li>- Outer diameter;</li> <li>- Height.</li> </ul>
<p>ii) <b>Material properties (MP)</b></p> <ul style="list-style-type: none"> <li>- Flow stress (<math>\epsilon, \dot{\epsilon}, T</math>) dependence;</li> <li>- Yield strength (YS) and Young's Modulus (E) influence.</li> </ul>	<p>iv) <b>Processing conditions (PC)</b></p> <ul style="list-style-type: none"> <li>- Ring initial temperature (uniform);</li> <li>- Friction (constant);</li> <li>- Tools temperature (constant).</li> </ul>

Figure 4 – Process variable analyzed for implementing the flat ring model.

Speed parameters group SP is composed of the initial and final values of main roll rotational speed, mandrel feeding speed, and axial roll feeding speed: with these 6 values, all the process tool speeds are settled. The rotational speed of the main roll is chosen from a range of previous literature studies [4, 16], while the mandrel speed is defined by ring and tools geometry, as well as the axial rolls speeds. All the considerations and the main formulations utilized will be explained in the next section 3.2. Concerning the geometrical parameters of the ring RG, this group is composed of initial and final values of inner diameter, outer diameter, and height:

initial geometry parameters are linked to the desired final geometry by volume conservation principle: so, 1 of the 6 geometrical variables is redundant. The material properties group contains parameters that are temperature-dependent: these are Flow stress, Yield strength (YS), and Young's modulus (YM). Once the initial process temperature is set, the YS value and the YM value are directly estimated from the material flow stress, considering a perfectly plastic flow stress model. Moreover, these 3 variables define uniquely a specific material at a specific temperature. The initial value of each of them has been considered as representatives: the materials considered in this research are steel alloy 42CrMo4, super alloy Inconel 718, and aluminum alloy AA6082. All these materials are largely used in the ring rolling process [18, 70, 78]. Finally, the process condition PC group is composed by the ring initial temperature, considered as uniform on ring volume, the friction value between ring and tools, and the constant tools temperature: these 3 parameters define univocally the ring growth condition.

Starting from these 18 process parameters, a set of 380 different and unique RARR process cases has been developed, varying differently the process parameters: in the following section, the analytical process for ring evolution estimation and the speed laws used for calculating each process parameter will be explained.

### 3.2 Flat ring rolling process set-up

The geometrical expansion of the ring is defined by two assumptions: the empirical Keeton's rule [5] presented in Eq. (1) and the volume conservation, utilized by Qian et al. [28] as an assumption for the calculation of the blank size starting from the dimensions of the final ring. These two assumptions permit to find a correlation between initial and final ring geometry and have been applied to each one of the above-mentioned 380 cases.

$$h_0^2 - s_0^2 = h_F^2 - s_F^2 \quad (1)$$

Eq. (1) defines that the squared difference between the initial height and thickness of the ring must be the same as that of the final geometry. By applying this geometry evolution constancy principle, a uniform and stable evolution of the ring, throughout the whole process, can be achieved.

Concerning the main roll rotational speed  $\omega_R$ , the following formula defines a range that allows establishing the optimal value in terms of process stability: this practical rule is suggested by Zhou et al. in [4, 32], it is a function of the main roll radius  $R_R$  value and it is based on practical experience under the hypothesis of no slippage between the ring and main roll.

$$1.2 \cdot R_R \leq \omega_R \leq 1.4 \cdot R_R \quad (2)$$

Concerning mandrel speed and taking into account Berti and Quagliato [16] assumptions, initial  $v_{M0}$  and final  $v_{MF}$  mandrel speed of every set of analysis has been calculated inside the ranges:

$$\frac{\omega_R \cdot R_R \cdot 6.55 \cdot 10^{-3} \cdot (R_0 - r_0)^2 \cdot S_1}{2\pi \cdot R_0} < [v_M]_0 < \frac{\omega_R \cdot R_R \cdot \beta_R^2 \cdot S_1}{\pi \cdot R_0 \cdot (S_3)^2} \quad (3)$$

$$\frac{\omega_R \cdot R_R \cdot 6.55 \cdot 10^{-3} \cdot (R_F - r_F)^2 \cdot S_2}{2 \cdot \pi \cdot R_F} < [v_M]_F < \frac{\omega_R \cdot R_R \cdot \beta_R^2 \cdot S_2}{\pi \cdot R_F \cdot (S_3)^2} \quad (4)$$

$$\text{where } S_1 = \frac{1}{R_R} + \frac{1}{R_M} + \frac{1}{R_0} + \frac{1}{r_0} ; S_2 = \frac{1}{R_R} + \frac{1}{R_M} + \frac{1}{R_F} + \frac{1}{r_F} ; S_3 = \frac{1}{R_R} + \frac{1}{R_M} \quad (5)$$

In Eqs. (3)-(5),  $R_0$ ,  $r_0$ ,  $R_F$  and  $r_F$  are the initial and final outer and inner radii of the ring,  $R_R$  and  $R_M$  are the radii of the main roll and of the mandrel, and  $\beta_R$  is the friction angle.

During the process, also the upper and lower axial rotational rolls are involved, and their feeding speed has been calculated according to Eqs. (6)-(7). A complete description of the calculation and the assumptions are presented in Berti et al. [16].

$$\frac{\omega_R R_R \frac{0.0131 \cdot h_0^2}{\left(L_0 - \frac{S_0}{2}\right) \tan\left(\frac{\theta}{2}\right)}}{2\pi R_0} < [v_A]_0 < \frac{4\omega_R R_R 4\beta_A^2 \left(L_0 - \frac{S_0}{2}\right) \tan\left(\frac{\theta}{2}\right)}{2\pi R_0} \quad (6)$$

$$\frac{\omega_R R_R \frac{0.0131 \cdot h_F^2}{\left(L_F - \frac{S_F}{2}\right) \tan\left(\frac{\theta}{2}\right)}}{2\pi R_F} < [v_A]_F < \frac{4\omega_R R_R 4\beta_A^2 \left(L_F - \frac{S_F}{2}\right) \tan\left(\frac{\theta}{2}\right)}{2\pi R_F} \quad (7)$$

In Eqs. (6)-(7),  $\theta$  is the vertex angle of the cone,  $\beta_A$  is the frictional angle defined as  $\beta_A = \tan^{-1} \mu_A$  with  $\mu_A$  the Coulomb friction coefficient, and  $L_0$ ,  $L_F$  are the initial and final distance between the vertex of the axial roll and the outer radius of the ring. The setting of these two distances depends on the configuration adopted during the process: if the ring has a small size, the axial rolls are not moving and  $L_F > L_0$ , while if the ring is big,  $L$  is considered constant and  $L_F = L_0$ .

### 3.3 Finite element model setting

The aim of this research is to find the process parameters correlation to consider for developing an energy consumption model: in order to do this, a database has been created considering various combinations of the input parameters described in sections 3.1 and 3.2. Due to the numerous columns and rows contained on the database table that contains 380 flat RARR process combinations, the totality of the input parameters has been listed in a summarized Table 1. Each one of these process combinations has been set and run with a FE model, using the commercial SW Simufact Forming 15 specific for different forming manufacturing processes. In particular this software permits to simulate the considered bulk deformation process on the three dimensions and it relies on realistic elastoplastic material modeling. For this specific research on RARR processes, the finite element simulations results to be reliable and precise thanks to the possibility to use a dedicated module

namely “Rolling module”, allowing to represent the reality of the process and the unique process modeling with rigid body motions, ensures the simulation of workpiece movements very close to reality. At first, only a portion of the generated database has been used to implement the linear regression model, and then the total dataset has been used for the training and the validation of the machine learning-based force integral over time (FIOT): all these aspects will be presented and explained in section 3.4 and 3.5.

As illustrated in Table 1 a total of 16 different preform rings have been combined with the considered six final outer diameters ( $D_F$ ), chosen in the range  $650 \text{ mm} < D_F < 2000 \text{ mm}$ . The three materials reported in section 3.1 and considered in the analysis have different characteristics in terms of mechanical behavior: this allows to extend the range of validity of the proposed study and the developed predictive model. For the definition of the plastic material behavior, the Hansel-Spittel flow stress model has been considered and reported in Eq. (8):

$$\sigma_F = C_1 \cdot e^{(C^2 \cdot T)} \cdot \varepsilon^{(n_1 \cdot T + n_2)} \cdot e^{\left(\frac{L_1 \cdot T + L_2}{\varepsilon}\right)} \cdot \dot{\varepsilon}^{(m_1 \cdot T + m_2)} \quad (8)$$

where  $\sigma_F$  is the flow stress,  $\varepsilon$  the strain,  $\dot{\varepsilon}$  the strain rate and  $T$  is the deformation temperature. The constant parameters are specific for a given material: in Table 2 are reported the specific values for steel alloy 42CrMo4, super alloy IN-718, and aluminum alloy AlMgSi1. Thermal and mechanical material properties and flow curves have been taken from MATILDA® (Material Information Link and Database Service) archive, available in the Simufact Forming 15 database: this package permits to simulate the behavior of materials in forming processing at different working temperatures. The main properties of the considered materials are summarized in Table 3, while their trend is reported in Appendix 1.

Table 1 – Summary of the 380 combinations.

		42CrMo4			AlMgSi1			IN-718			
		T [°C]									
		900	1050	1200	300	375	450	980	1025	1070	
$\omega_R$ [rad/s]	$\bar{v}_M$ [mm/s]	$D_0$ [mm]	$D_F$ [mm]			$D_F$ [mm]			$D_F$ [mm]		
2	2.05	944.7	2000	2000	2000	-	-	-	-	-	-
	2.17	944.7	-	-	-	2000	2000	2000	2000	2000	2000
	2.24	897.7	1700	1700	1700	1700	1700	1700	1700	1700	1700
	2.55	909.3	1400	1400	1400	1400	1400	1400	1400	1400	1400
	2.56	876.2	1400	1400	1400	1400	1400	1400	1400	1400	1400
	2.75	549.3	650	650	650	650	650	650	650	650	650
	3.11	621.6	1100	1100	1100	1100	1100	1100	1100	1100	1100
	3.37	897.7	1700	-	-	-	-	-	-	-	-
	3.60	550.9	800	800	800	800	800	800	800	800	800
	4.09	575.3	1100	1100	1100	1100	1100	1100	1100	1100	1100
	4.88	518.9	800	800	800	800	800	800	800	800	800
	5.65	490.5	650	650	650	650	650	650	650	650	650
	5.67	897.7	1700	-	-	-	-	-	-	-	-
	5.70	490.5	650	650	650	650	650	650	650	650	650
5.73	490.5	650	650	650	650	650	650	650	650	650	

			42CrMo4			AlMgSi1			IN-718		
		T [°C]	900	1050	1200	300	375	450	980	1025	1070
$\omega_R$ [rad/s]	$\dot{v}_M$ [mm/s]	$D_0$ [mm]	$D_F$ [mm]			$D_F$ [mm]			$D_F$ [mm]		
3	2.92	944.7	2000	2000	2000	-	-	-	-	-	-
	3.27	944.7	-	-	-	2000	2000	2000	2000	2000	2000
	3.37	897.7	-	1700	1700	1700	1700	1700	1700	1700	1700
	3.70	1049.3	-	-	2000	-	-	-	-	-	-
	3.75	549.3	650	650	650	650	650	650	650	650	650
	3.82	909.3	1400	1400	1400	1400	1400	1400	1400	1400	1400
	3.83	876.2	1400	1400	1400	1400	1400	1400	1400	1400	1400
	3.85	944.5	-	-	2000	-	-	-	-	-	-
	4.10	875.7	-	-	2000	-	-	-	-	-	-
	4.50	549.3	650	650	650	650	650	650	650	650	650
	4.60	621.6	1100	1100	1100	-	-	1100	1100	1100	1100
	5.15	668.7	1100	1100	1100	1100	1100	1100	1100	1100	1100
	5.25	549.3	650	650	650	650	650	650	650	650	650
	5.39	550.9	800	800	800	800	800	800	800	800	800
	5.50	549.3	650	650	650	650	650	650	650	650	650
	5.60	621.6	1100	1100	1100	1100	1100	1100	1100	1100	1100
	5.75	549.3	650	650	650	650	650	650	650	650	650
	6.00	490.5	650	650	650	650	650	650	650	650	650
	6.10	575.3	1100	1100	1100	1100	1100	1100	1100	1100	1100
	6.85	518.9	800	800	800	800	800	800	800	800	800
7.50	510.9	650	650	650	650	650	650	650	650	650	
7.60	490.5	650	650	650	650	650	650	650	650	650	
8.50	490.5	650	650	650	650	650	650	650	650	650	
5	4.09	575.3	1100	-	-	-	-	-	-	-	-
	4.85	944.7	2000	2000	2000	-	-	-	-	-	-
	5.43	944.7	-	-	-	2000	2000	2000	2000	2000	2000
	5.67	897.7	-	1700	1700	1700	1700	1700	-	1700	1700
	6.35	909.3	1400	1400	1400	1400	1400	1400	1400	1400	1400
	6.38	876.2	1400	1400	1400	1400	1400	1400	-	1400	1400
	7.30	549.3	650	650	650	650	650	650	650	650	650
	7.69	621.6	1100	1100	1100	-	-	-	1100	1100	1100
	8.97	550.9	800	800	800	800	800	800	800	800	800
	10.04	575.3	-	1100	1100	1100	1100	1100	1100	1100	1100
	12.12	518.9	800	800	800	800	800	800	800	800	800
	13.7	490.5	650	650	650	650	650	650	650	650	650
	14	490.5	650	650	650	650	650	650	650	650	650
	14.15	490.5	650	650	650	650	650	650	650	650	650



Table 2- Validity range and Hansel-Spittel flow stress model constants for the i) 42CrMo4 steel, ii) Inconel 718 super alloy and iii) AA6082 (AlMgSi) aluminum alloy.

<b>Parameters</b>	<b>42CrMo4</b>	<b>IN 718</b>	<b>AA6082</b>
Temperature range for the model [°C]	800–1250	950-1100	200-530
Strain range for the model [-]	0.05–2	0.05-2	0.05-0.9
Strain rate range for the model [1/s]	0.01–150	0.01-150	0.01-63
$C_1$	5290.5	10501.1	378.5
$C_2$	-0.00370	-0.00307	-0.00492
$n_1$	-0.00033	-0.00018	-0.00011
$n_2$	0.20612	0.54398	-0.02573
$L_1$	-8.26584e-5	-2.17606e-5	6.03612e-5
$L_2$	0.02891	0.02376	-0.02548
$m_1$	0.000301	-2.67316e-6	0.000345
$m_2$	-0.15618	0.09746	-0.031501

Table 3 - Ring rolling mill characteristics and general process settings.

	<b>42CrMo4</b>			<b>Inconel 718</b>			<b>AA6082</b>		
Initial temperature [°C]	900	1050	1200	980	1025	1070	300	375	450
Density [kg/m <sup>3</sup> ]	7847			8190			2695		
Young modulus [GPa]	129	108	84	126	120	100	58	54	51
Yield strength [MPa]	126	50	40	216	187	161	101	82	67
Thermal conductivity [W/(m·K)]	28	29	30	29	30	31	200	208	214
Specific heat capacity [J/(kg·K)]	645	635	642	647	687	704	1032	1069	1120

The tools involved and set in the FEM model have been described and represented in Fig. 1 in section 1.1: for this analysis, the dimensions have been considered as constant, in order to avoid the introduction of additional parameters in the analysis. The setting of the tools in terms of dimensions, temperature, and friction are reported in Table 4 and have been considered as rigid with heat transfer. The tools have been meshed with the 3D 8-node, first-order iso-parametric heat transfer element (MARC® element type 43) and considered rigid with heat transfer with both the ring and the surrounding simulated environment.

Friction has been calculated considering the constant shear friction described in Eq. (9) and the utilized friction factor reported in Table 4.

$$\tau = m \cdot k \quad (9)$$

Table 4 - Ring rolling tools characteristic and general process condition.

Parameters	Value
Radius of the main roll [mm]	325
Radius of the mandrel [mm]	125
Length of the axial rolls [mm]	595.9
Half of cone vertex angle [°]	17.5
Temperature of the environment [°C]	50
Tool initial temperature [°C]	150
Friction factor mandrel and main roll [-]	0.85
Friction factor axial and guide rolls [-]	0.6

Considering the combination of initial and final ring geometries, process parameters, material properties, and boundary conditions as summarized in this chapter, the whole 380 FEM simulations relevant for the flat RARR process analysis have been calculated and set on FE models: a summary of the obtained results from numerical simulations will be presented in the following section.

### 3.4 Thermo-mechanical FEM models results

In order to show a meaningful case of the 380 performed simulations, a ring evolution in terms of equivalent plastic strain and mandrel force of one simulation has been summarized in section 3.4.1. In addition to that, the accuracy of the FEM model has been demonstrated by comparing the experiments made in Sogang University [11] with a ring rolling laboratory machine with an equivalent numerical simulation: this validation will be described in 3.4.2 along with the obtained results.

#### 3.4.1 Numerical model simulation results

According to the implemented numerical simulation model, as presented in section 3.3, and to the considered input parameters, the results of the implemented 380 FEM simulations have been exported and utilized in further analysis, presented from section 3.5. To provide an insight into the results of the implemented FEM simulations, and to prove their reliability, a concise summary of some of the results is presented in this section. Figure 5a-c represents the equivalent plastic strain distribution on the ring at the end of the rolling phase, whereas in Fig. 5d-f the evolution of the outer diameter of the ring over time is shown. The results in Fig. 5a-c and 5d-f are relevant for the same simulation cases and representative of final outer diameter 800 mm, 1100 mm, and 2000 mm, for the case of 42CrMo4 steel at the initial temperature of 1200 °C.

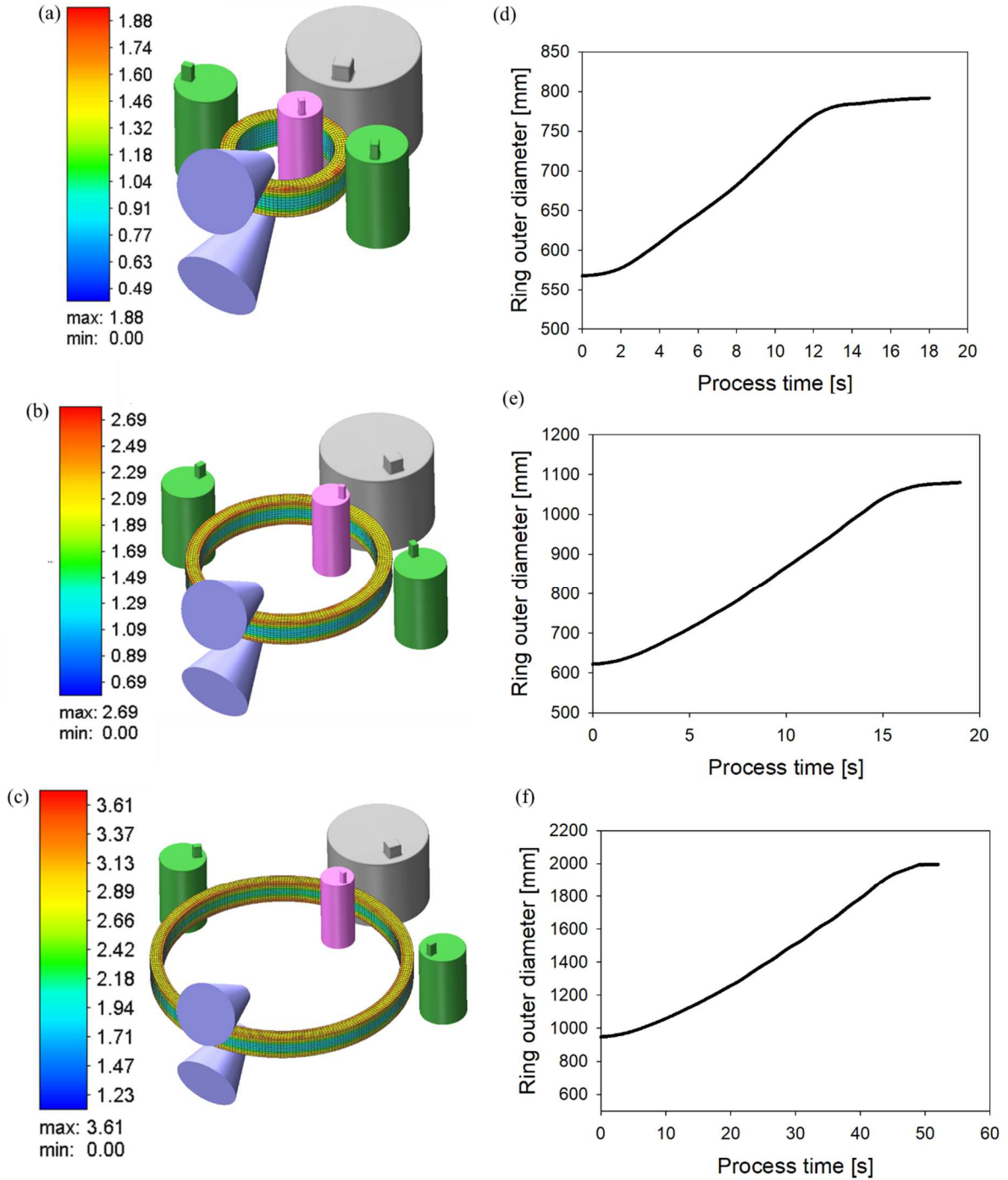


Figure 5 – (a)-(c) Effective plastic strain and (d)-(f) outer diameter expansion for three case studies relevant for 800 mm, 1100 mm, and 2000 mm.

Furthermore, considering the 380 simulations, the force applied by the mandrel during the RARR process as well as the mandrel feeding time, have been exported from FEM simulations and used for the creation of the training and test database for the machine learning algorithms. As a representative example, the radial forming forces for the three cases reported in Fig. 5 are shown in Fig. 6. Due to the large amount of data composing the database, they are summarized in Appendix 2.

As remarked in the previous paragraphs, the starting point of the research for the estimation of energy consumption is to utilize the amount of energy as a sort of measure of the force impulse. For the automatic calculation of the time integral of the force, allowing to calculate the force impulse, a script has been implemented in MS-Excel. The mandrel time has been used for the calculation of the impulse: in fact, the mandrel force gradually increases until it reaches the maximum value and, when the mandrel time is over and the calibration time starts, it gradually decreases until the end of the process, as shown in Fig.6. The mandrel time has been set by the user in the numerical simulations according to [16], whereas the calibration time could be adjusted to obtain a better final ring geometry accuracy. For this reason, the computational time has not been considered during the analysis since most of the process energy is employed during the translation towards the main roll of the mandrel.

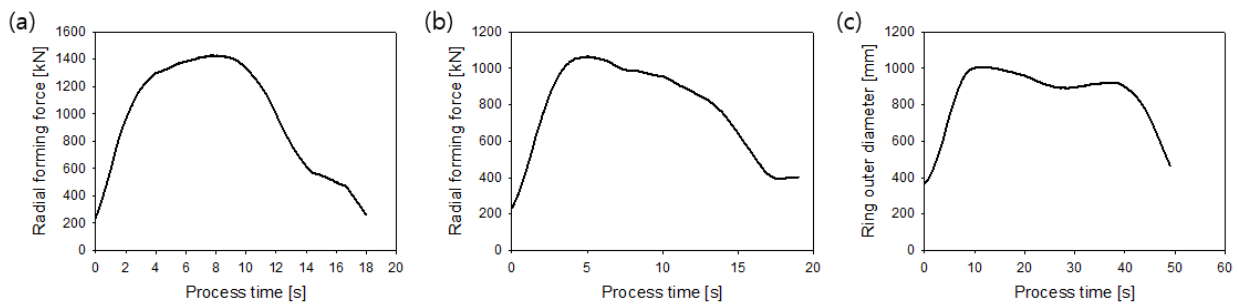


Figure 6 – Radial forming force relevant for the cases of Fig. 5.

### 3.4.2 FEM validation

Since the starting point for all the analysis relevant for the flat RARR process has been based on the results of the above-mentioned 380 FEM simulations, an assessment of the accuracy of the implemented solutions is necessary. To this aim, the experimental results summarized in Quagliato and Berti [11] have been considered, as hereafter reported. The experiment has been carried out on a lab-scale ring rolling machine in Sogang University, Fig. 7, and thanks to a metering roll and to the load cells installed on the main roll and the upper axial roll, the data have been recorded and exported to be used for a comparison with the FEM simulation.

The considered ring has been manufactured with a soft alloy made of 75% lead and 25% tin (Pb75-Sn25 alloy) under cold forming condition. The Pb75-Sn25 soft alloy has been chosen as its plastic behavior under severe plastic deformations at room temperature resembles that of steel at high temperature. The ring dimensions are summarized in Table 5 and the images of the ring before and after the ring rolling process are shown in Fig. 7. The same process setting has been considered in both the experiment as well as in the FEM numerical simulation. The model has been implemented by means of the same procedure presented in section 3.3, as reported in Table 5, considering in this specific case a cold deformation process.

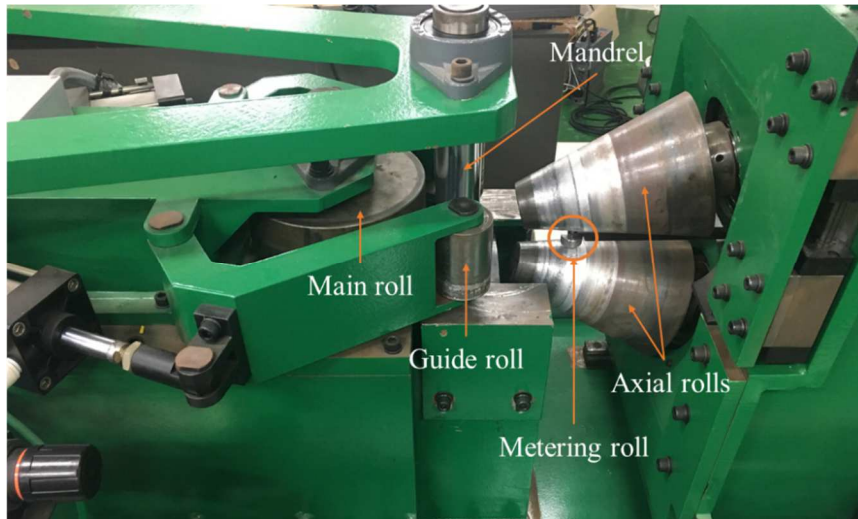


Figure 7– Ring rolling machine for the lab-scale experiments utilized for the developed FEM model validation.

The comparison between FEM prediction and experimental results is shown in Fig. 9. The accuracy of the implemented numerical model has been demonstrated by replicating real process conditions and is represented in Fig. 9, where the maximum deviation between experimental and finite element model results is equal to 0.95% for the outer diameter, and 2.15% for the radial forming force.

Table 5 - Initial and final dimensions of the Pb75-Sn25 ring experiment.

Ring geometry	Value [mm]
Outer initial diameter - $D_0$	155
Inner initial diameter - $d_0$	105
Initial thickness - $s_0$	25
Initial height - $h_0$	42
Outer final diameter - $D_F$	195
Inner final diameter - $d_F$	155
Final thickness - $s_F$	20
Final height - $h_F$	36



(a) Ring blank



(b) Final ring

Figure 8 – (a) Initial and (b) final Pb75-Sn25 rings.

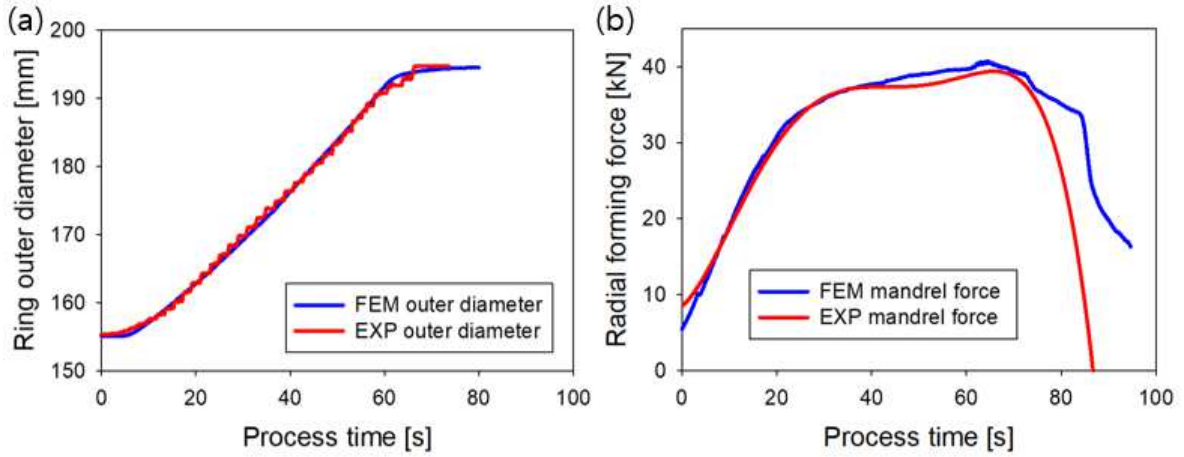


Figure 9 – Comparison between experimental and finite element (a) outer diameter and (b) radial forming force for the Pb75-Sn25 validation ring.

### 3.5 Multi-variable regression model evolution

The first approach considered during the study is the multivariable regression method. This approach is suitable for determining the correlation between variables. In this thesis, the theory of the regression model is described in 3.5.1 and the results of this approach are explained and shown in 3.5.2.

#### 3.5.1 Regression model definition

The multi-variable regression is a technique that permits to predict a dependent variable  $Y$  starting by independent variables  $x_i$ : or rather, considering two or more different variables as input of the model, it is possible to obtain the desired output. The model involves  $i$  dependent variables  $x_i$ , shown in the following three-order generic Eq. (10):

$$Y = b_0 + b_1x_1 + b_2x_2 + b_{11}x_1^2 + b_{22}x_2^2 + b_{12}x_1x_2 + \dots + e_i \quad (10)$$

where  $b_0$  is the intercept,  $b_1$ ,  $b_2$  are the linear effect parameters,  $b_{11}$ ,  $b_{22}$  are the quadratic effect parameters,  $b_{12}$  is defined as interaction effect parameters and  $e_i$  is the error in correspondence with the  $i$ -th observation. The single coefficients  $b_1$ ,  $b_2$ , ...,  $b_n$  are called regression coefficients, the  $x_{1i}$ ,  $x_{2i}$ , ...,  $x_{pi}$  are the values assumed by the explanatory variables named predictors, and  $Y$  is the response of the model.

In this research, the regression model has been built using the Minitab commercial software, and a stepwise approach has been performed to build the fit regression model: this method has been used for describing the connection between the variables of the ring rolling process and energy consumption. Model regression coefficients have been calculated by the least-squares method with the purpose of reducing the sum of the deviation from the regression line.

A fit regression model is a method that permits to identify the optimal correlation between the dependent variables  $x_i$  and the independent variable  $Y$ : this kind of regression has been chosen and applied through Minitab to check the effective correlation between the pre-formulated input variables and the required output, that in our study is the energy consumption.

The stepwise regression is an additional method applied to the multi-variable fit regression, allowing to obtain a simplification of the predictive formula. This kind of optimization allows selecting the best independent variables by identifying the fittest relationships between the set of predictors and the dependent variable: this iterative construction method identifies relationships hidden by all relevant variables of the model, permitting to build a final regression model with the most useful terms and to make the final equation less complex. To optimize the stepwise approach, several tests have been conducted, varying alpha-to-enter and alpha-to-remove values: the first value establishes if a term can be included in the final equation, while the second one defines if a term must be removed. More specifically, the stepwise approach begins from an empty model or a user-defined model and starts to add or remove terms: the user can eventually force terms to be included in the final model. The iteration stops when the variables included in the model have a p-value greater than Alpha-to-enter and less than Alpha-to-remove. The probability value, or also called p-value, is a probability measurement that shows if an observed difference has been found just by random chance: a lower number of p-value means a greater statistical influence of the observed difference. P-value is calculated by software using the deviation between the reference value, the energy in this case, and the observed value. A p-value less than 0.05 is considered statistically significant: it means that there is a 5% probability that the results are random.

Another two important values considered during the development of the multi-variable fit regression model are the R-squared and the Adjusted R-squared value. The first one is also known as the coefficient of multiple determination, and it is a statistical measure that indicates how much variation there is between data and the fitted regression line: R-square value range is between 0% and 100%, and usually a higher R-square value means that the model fits the data well. The adjusted R-squared value is a modified version of the R-squared measure that considers the number of independent variables: it is a useful tool to understand if a new predictor has enhanced or not the regression model by comparing it with the R-square value.

### 3.5.2 Model development and results

The process variables chosen for the linear multi-variable fit regression on Minitab software are 7 and are defined in the following Table 6.

The Y value as above stated is the energy consumption estimated with the FEM simulations: the  $x_i$  values have been derived from the first database composed by a final outer diameter range from 800 mm to 1700 mm for a total of 65 cases. After several attempts, the optimal regression model with the constructed set of data is a two-order equation with 22 terms, as reported in Eq. (11) and Table 7.

Table 6 – Process variables considered for the regression model.

Variables	Description
$x_1$	$C = (D_F \cdot s_F)/(d_F \cdot h_F)$ parameter for identifying the final geometry
$x_2$	$\omega_R$ = main roll rotational speed
$x_3$	$v_{mM}$ = Mandrel feeding speed chosen in the middle of the reasonable range
$x_4$	$T$ = temperature
$x_5$	$E$ = Young modulus
$x_6$	$Y_S$ = yield strength
$x_7$	$F = (D_0 \cdot s_0)/(d_0 \cdot h_0)$ parameter for identifying the initial geometry

$$\begin{aligned}
 Y = & \alpha_1 x_2 + \alpha_2 x_5 + \alpha_3 x_1^2 + \alpha_4 x_4^2 + \alpha_5 x_6^2 + \alpha_6 x_7^2 + \alpha_7 x_1x_2 + \alpha_8 x_1x_3 + \alpha_9 x_1x_4 \\
 & + \alpha_{10} x_1x_5 + \alpha_{11} x_1x_6 + \alpha_{12} x_1x_7 + \alpha_{13} x_2x_5 + \alpha_{14} x_2x_6 + \alpha_{15} x_3x_4 \\
 & + \alpha_{16} x_3x_6 + \alpha_{17} x_3x_7 + \alpha_{18} x_4x_5 + \alpha_{19} x_4x_6 + \alpha_{20} x_4x_7 + \alpha_{21} x_5x_7 \\
 & + \alpha_{22} x_6x_7
 \end{aligned} \tag{11}$$

Table 7 – Coefficients of the regression equation.

$\alpha_1$	120439	$\alpha_{12}$	95476
$\alpha_2$	2702	$\alpha_{13}$	-67.7
$\alpha_3$	4311163	$\alpha_{14}$	-2037
$\alpha_4$	0.00785	$\alpha_{15}$	1.974
$\alpha_5$	138.1	$\alpha_{16}$	1039
$\alpha_6$	-43455	$\alpha_{17}$	-7606
$\alpha_7$	129980	$\alpha_{18}$	-0.546
$\alpha_8$	-150028	$\alpha_{19}$	-0.617
$\alpha_9$	148	$\alpha_{20}$	-10.58
$\alpha_{10}$	-3460	$\alpha_{21}$	177.7
$\alpha_{11}$	-50676	$\alpha_{22}$	668

Considering the stepwise optimization method, the value chosen is 0.5 for both alpha-to-enter and alpha-to-remove: this value permits obtaining the best residuals result, simplifying the final model. The R-square value obtained is 99.77% and the Adjusted R-square value is 99.65%: the maximum variable p-value is 0.047. The graph in Fig. 10 compares the energy consumption of FEM simulations with the energy predicted by the regression Eq. 11. The maximum error is 21.8% while the average error is 5.09%.

A new database has been built with an additional set of data in order to amplify the case studies range and as an attempt to improve the maximum error obtained in the first regression model: a total of 240 simulations



has been run with a final outer diameter range from 650mm to 2000mm. The  $x_i$  variables remain the same as previously used, as the multi-variable fit regression approach. After several tests, the optimal resulting predictive formula is a 4th-order equation composed of 89 terms: a value of 0.6 has been chosen in the stepwise optimization. The maximum p-value is equal to 0.47, the R-square value is 99.69%, and the Adjusted R-square value is 99.5%: regardless of the high value of R-square and AR-square, comparing the energy obtained through FE simulation and the predicted energy, the regression equation gives an average error of 15% and a maximum error of 137%, which is unacceptable.

In the following Fig. 11, the comparison between the FE simulation energy and the predicted energy with the amplified database is shown. The high number of terms in the equation and the high maximum error make this regression method industrially unusable: for this reason, other predictive methods have been investigated.

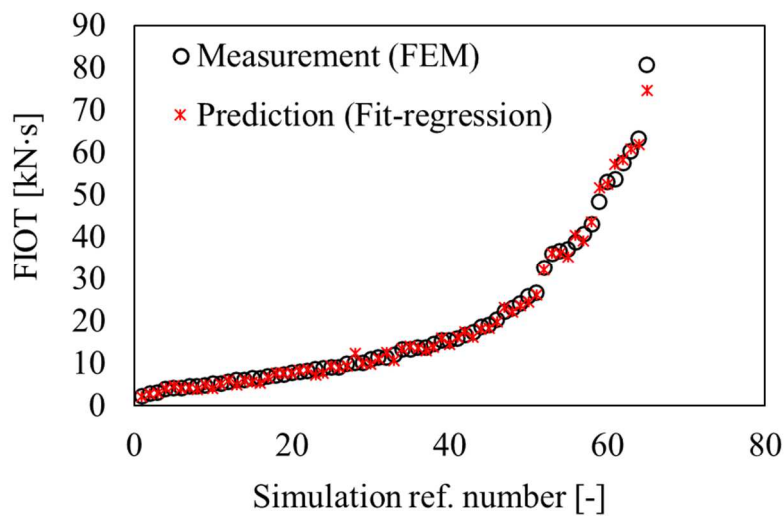


Figure 10 – Comparison between FEM and Fit regression prediction.

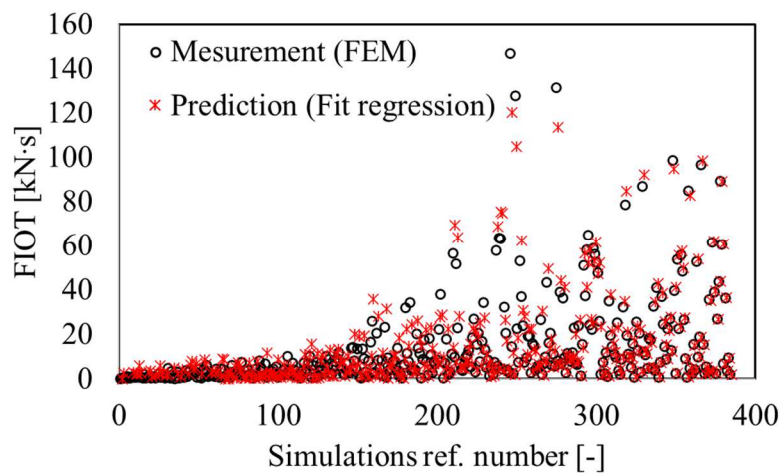


Figure 11 – Comparison between FEM and Fit regression prediction.

## 3.6 Machine learning models definition

Due to the complexity of the RARR process and the difficulty of finding a correlation between the process parameters and the energy consumption through the linear regression method, several Machine Learning methods have been considered and tested to achieve the aim of this research. Machine Learning, abbreviated as ML, is a sub-field of Artificial Intelligence and it is an algorithm that can automatically learn from input data in order to give the desired output: Artificial Intelligence, or AI, includes every program or device that perceives the environment inputs and takes correlated action to achieve the desired target successfully. Reported below are four of the several machine learning methods that have been considered: eight ML algorithms have been developed, and after the explanation of each methodology, a resume of models' results will be reported, as well as a comparison of all the developed methods and final considerations.

The same seven process parameters values (Table 6) used the for the multi-variable linear regression have been utilized: the energy consumption is the output result, and it is still considered as the force impulse. The database that has been used is composed of 380 FE simulations with a final outer diameter range from 650mm to 2000mm: a randomly selected 80% of the simulation dataset has been used for models training and the remaining 20% has been considered for accuracy assessment of the trained algorithms.

### 3.6.1 Multiple Linear Regression method

Multiple Linear Regression is a Neural Network methodology used to find a correlation between multiple  $x$  variables and the dependent variable  $y$ : the predicted value  $\hat{y}$  is calculated with the minimization of the Residual Sum of Squares (RSS), which is also called Cost Function. The generic Eq. (12) to calculate  $\hat{y}$  and the RSS definition (13) are below reported.

$$\hat{y} = w_0 + w_1x_1 + \dots + w_Dx_D = w_0 + w^T X \quad (12)$$

$$RSS(w) = \sum_{i=1}^N (y_i - w^T X_{i,D})^2 \quad (13)$$

where  $D$  is the input variables number,  $w_D$  are coefficients or weights, and  $N$  is the dataset size. Several Multiple Linear Regression algorithms exist and for this study, 3 different approaches have been considered.

The first one is the Ridge Model: this model aims to minimize the objective function  $Y$  composed by the cost function RSS with the addition of a penalty, as defined in the following Eq. (14).

$$Y(w) = RSS(w) + \lambda \sum_{j=1}^D \|w_j\|^2 \quad (14)$$

Where  $\lambda$  is called penalty hyperparameter, and it is a tuning parameter of the penalty that is adjusted during the model training to maximize the correlation factor between independent and dependent variables, and to enhance the accuracy [79]. Usually,  $\lambda$  has a small value: if the value is 0, the objective function is equal to the original multi variable regression model.

The second model considered is the Least Absolute Shrinkage and Selection Operator algorithm, also called LASSO. This approach is similar to the Ridge model with a different definition of the penalty: while in the Ridge algorithm the penalty is defined as the sum of squared value of weights, in the LASSO model the penalty consists of the sum of the absolute value of weights as stated in Eq. (15)

$$\gamma(w) = \frac{1}{2N} \text{RSS}(w) + \lambda \sum_{j=1}^D \|w_j\| \quad (15)$$

The third model concerning multiple linear regression is the Elastic Net Model resumed by the following Eq. (16). This algorithm is a hybrid version of the Ridge model and LASSO model: in fact, it contains both penalties, the sum of squared weight and the sum of absolute value weight. Moreover, for this algorithm, there are the penalty hyperparameter  $\lambda$ , calculated during the training, and the parameter  $\alpha$ , usually set by the user, and for this study calculated through random search method [79]. The value of  $\alpha$  is between 0 and 1: with  $\alpha$  equal to 0 the Elastic Net Model turns into the Ridge Model, while for  $\alpha$  equal to 1 it becomes the LASSO algorithm.

$$\gamma(w) = \frac{1}{2N} \text{RSS}(w) + \lambda \left\{ \frac{(1-\alpha)}{2} \sum_{j=1}^D \|w_j\|^2 + \lambda \sum_{j=1}^D \|w_j\| \right\} \quad (16)$$

### 3.6.2 Kernel method

By replacing a non-linear equation in the multiple linear regression mentioned above, a non-linear relationship between independent variables  $x$  and dependent variable  $y$  can be obtained. Instead of representing the  $x$  variables with a linear function (12), they can be explicated with the Kernel function  $\kappa(x_i, x_j)$  obtained by the following Eq. (17):

$$k(x_i, x_j) = \phi(x_i)\phi(x_j) \quad (17)$$

where  $\phi(x)$  is the feature function. One of the advantages of the Kernel approach is the so-called Kernel trick: instead of computing the coordinates of each data in a determined space, it calculates the inner products between images of all data pairs in the function space. The kernel function is contained in the Gram matrix, a positive semi-definite symmetric matrix (18) used for linear independence analysis of function:

$$\mathbf{K} = \phi\phi^T = \begin{bmatrix} \kappa(x_1, x_1) & \cdots & \kappa(x_1, x_n) \\ \vdots & \ddots & \vdots \\ \kappa(x_n, x_1) & \cdots & \kappa(x_n, x_n) \end{bmatrix} \quad (18)$$

Two neural network regression approaches have been considered, both derived from the Kernel approach. The first one is the Kernel Ridge (KR) method derived from the combination of the Kernel theory (17) and Ridge model (14): a polynomial version of the Kernel function has been used as reported below in Eq. (19).

$$\kappa(x_i, x_j) = (\gamma x_i^T x_j + c)^d \quad (19)$$

where  $\gamma, c$ , and  $d$  are constants set during the training phase of the development through the random search method. The second method developed is the Support Vector Machine (SVM), [80], based on the Kernel approach and built with the same polynomial kernel Eq. (17). Below the main formulation is represented (20), with the epsilon intensive loss function used, where  $C$  is the regularization parameter,  $L_\epsilon$  the epsilon intensive loss function (21), and  $\epsilon$  a constant value that defines the tolerance of error:  $C$  and  $\epsilon$  are defined during the training phase.

$$Y(w) = C \sum_{i=1}^N L_\epsilon(y_i, \hat{y}_i) + \frac{1}{2} \sum_{j=1}^D \|w_j\|^2 \quad (20)$$

$$L_\epsilon(y, \hat{y}) = \begin{cases} 0 & \text{if } |y - \hat{y}| < \epsilon \\ |y - \hat{y}| - \epsilon & \text{otherwise} \end{cases} \quad (21)$$

### 3.6.3 Ensemble method

The Ensemble method [81-83] is an automatic learning where different learning algorithms are applied, and which randomly selects sub-sets of data to improve the prediction performances: the consideration of multiple methods also allows to obtain better performance and flexibility than the chosen models considered individually. Two different ensemble methods have been considered: the Random Forest (RF) and the Gradient Boosting (GB), as explained below. For each model, the database has been divided into a training part, and into a small validation part: moreover, each model permits solving non-linear case studies.

Random Forest RF is an ensemble learning method considered for the prediction of energy consumption: this algorithm builds and trains decision trees and gives an output for each one of them. Each decision tree is independent and not correlated: in fact, each decisional tree considers a different random subset of data from the main database for the training part. Moreover, each node of each tree gives a response based on a random interval of the dataset: so, the problem is subdivided into sub-classes, and each node response is classified by the accuracy compared with the true value. The final prediction of the RF model is the average of all the trees predictions, as resumed in equation (22):

$$\hat{y} = \sum_{m=1}^M \frac{1}{M} \hat{y}_m \quad (22)$$

where  $M$  is the number of trees. The overall functioning of the RF algorithm could be resumed by the following Fig. 12. The subdivisions of the whole data set permit the reduction of the strict correlation between the algorithm and the training data, to obtain a more flexible model, to reduce the variance, and to perform a better regression.

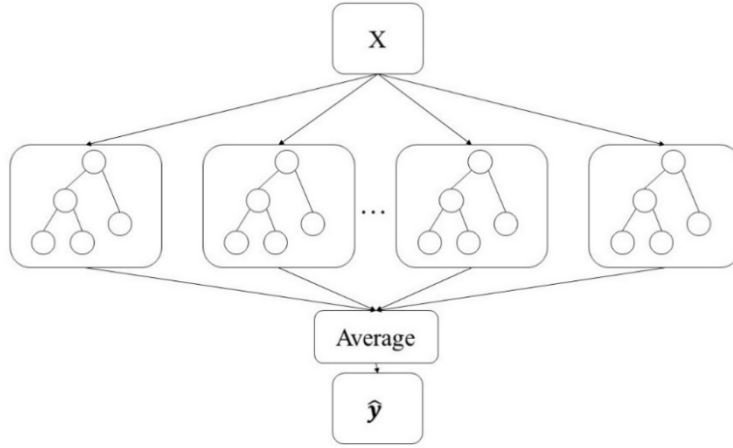


Figure 12 – Random Forest schematic functioning.

The second ensemble model is the Gradient Boosting: this algorithm starts from a weak learner and converts it into a strong learner. In this study, the initial weak learner is a single decision tree ( $f$ ): this first tree is trained and optimized to minimize the objective function  $Y(w)$ . The following decision tree is developed with the results of the previous tree, considering the gradient residual of the previous tree adjusted by the learning rate coefficient. The two equations (23, 24) resume the iterative passage of the GB model

$$Y(w) = L_{\delta}(y, f) = \begin{cases} \frac{1}{2}(y - f)^2 & \text{if } |y - f| < \delta \\ \delta|y - f| - \frac{1}{2}\delta^2 & \text{otherwise} \end{cases} \quad (23)$$

$$f_{m+1} = f_m + \eta \cdot r_{m+1}$$

$$\text{where } r_{i,m+1} = - \left| \frac{\partial L_{\delta}(y_i, f_i)}{\partial f_i} \right|_{f_m} \quad (24)$$

where  $f$  is the generic  $M$ -th tree,  $L$  is the loss function and  $\eta$  is the learning rate, which indicates the speed by which the algorithm minimizes the loss function. The value of the learning rate is set during the training phase of the model: if a non-linear regression is required, the learning rate is not used since the optimized value is the minimum of the loss function. The schematic functioning of the Gradient Boosting method is resumed in the following Fig. 13.

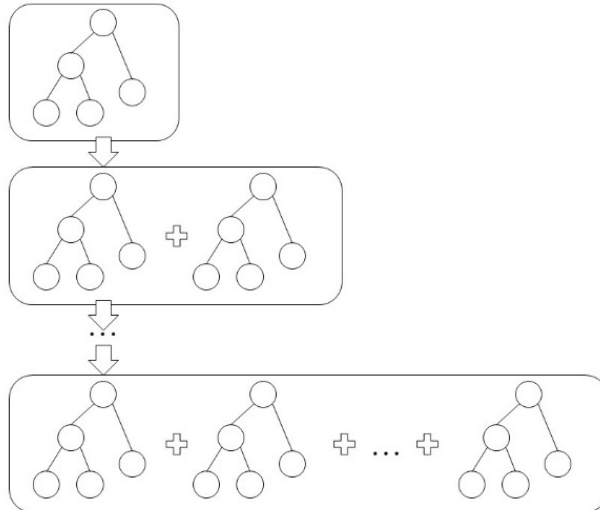


Figure 13 – Gradient Boosting schematic functioning.

### 3.6.4 Neural Network method

Artificial Neural Network models [84-86] belong to the deep learning algorithms, a sub-field of machine learning, and permit to lead a non-linear regression: it is an approach inspired by the human brain, that simulates the brain neurons network in order to learn from a dataset of input and return a related response as output. A Neural network model is composed of the first input layers, multiple hidden layers, and a final output layer, as resumed in Fig. 14.

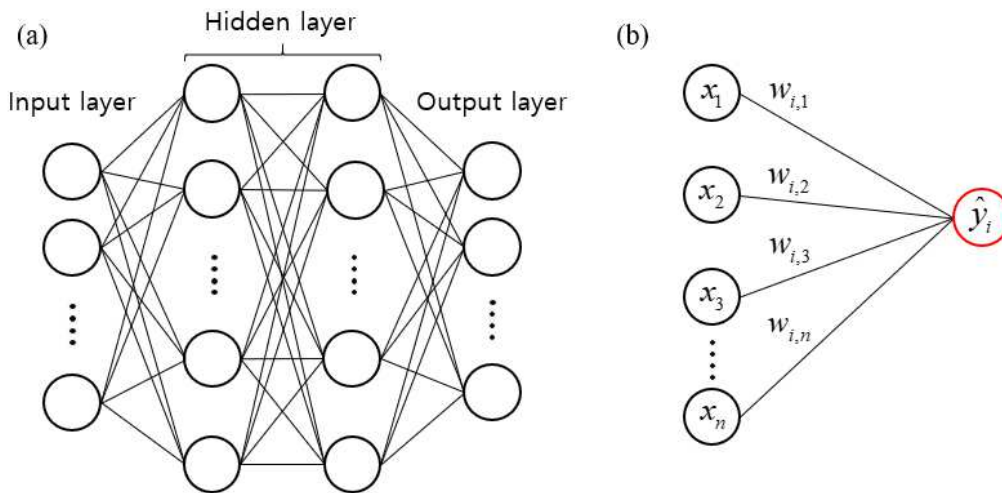


Figure 14 – (a) Artificial Neural Network model and (b) connection between nodes.

Hidden layers contain the weight function  $w_{ij}$  calculated during the training phase of the NN model: starting from the training dataset composed of variables  $x_i$  multiplied by weights  $w_{ij}$ , the output layer composed by  $y_i$  variables are calculated via the activation function shown in Eq. (25) and schematized in Fig. 14b.

$$\hat{y}_i = \Psi \left( \sum_{j=1}^D w_{ij} \cdot x_j + w_{i0} \right) \quad (25)$$

where  $\Psi$  is the activation function. The weight matrix has been updated at each adjustment of the Neural Network model considering the RMSprop algorithm [87] as reported in Eq. (26)

$$w_{i+1} = w_i - \eta \frac{1}{\sqrt{h}} \cdot \frac{\partial L_{\delta}(\mathbf{y}_i, \hat{\mathbf{y}}_i)}{\partial w_i} \quad (26)$$

$$\text{where } h_i = \rho \cdot h_{i-1} + (1 - \rho) \left( \frac{\partial L_{\delta}(\mathbf{y}_i, \hat{\mathbf{y}}_i)}{\partial w_i} \right)^2$$

Where  $\eta$  is the learning rate coefficient and  $\rho$  is a model hyperparameter: each one of these two values has been set and optimized with the random search method, already used for the other machine learning method. The activation function  $\Psi$  is defined as follows Eq. (27):

$$\Psi(x) = \begin{cases} 0 & \text{for } x \leq 0 \\ x & \text{for } x > 0 \end{cases} \quad (27)$$

$\Psi$  value it's a threshold indicator that establishes whether a node of a certain hidden layer must be activated: if the activation function value exceeds a certain level then the node of the i-layer is connected to the node of the i+1 layer. The developed Neural Network model for RARR regression has been composed of 4 hidden layers with respectively 200, 100, 50, and 25 nodes.

### 3.7 Energy prediction model result and validation

The machine learning and neural network models presented in the previous section have been all implemented in Python scripts. Considering the length of each script, only the one that provides the best prediction performances in terms of maximum and average errors have been included in Appendix 3.

Among the 380 simulations, 80% is randomly selected for the training, whereas the remaining 20% for the validation. For the test of the developed model has been used literature data instead of using part of the implemented database. In 3.7.2 the resulting models have been compared and analyzed in terms of performance and error. Finally, considering the model with the lesser residual result, the accuracy in the prediction of the force integral over time (FIOT) has been evaluated using three previously published experimental papers.

#### 3.7.1 Data pre-processing and machine learning algorithm training

The 8 algorithms described in the previous 3.6 paragraphs are developed in a Windows OS environment utilizing the scikit-learn 0.22.2 and Keras 2.3.1 modules implemented in Anaconda Spyder environment with Python 3.7.4. As previously mentioned, 80% of the whole 380 simulations, corresponding to 304 data, are randomly selected for the training and 20%, corresponding to 76 data, for the validation.

In the training phase, the model learns the relationship between input and output (target value). The validation phase is responsible for validating the results obtained in the training set. Being an iterative method,

if the residual is less than expected, the hyperparameters are changed and the process restarts with the training until the result is satisfying. In the present research, the dataset of both training and validation has been defined as a row of the table composed of the following data:

1. Main roll rotational speed,
2. Average mandrel feeding speed,
3. Initial ring geometry,
4. Final ring geometry,
5. Initial ring temperature,
6. Material yield strength,
7. Material Young's modulus,
8. Force integral over the mandrel time (FIOT).

where the first 7 are the model inputs, and the FIOT is the output. Since the input variables considered have different intervals and measurement units, normalization has been applied to convert them to a 0 to 1 range.

As concerns the FIOT, due to the skewness of the data distribution, the data has been converted into  $\log(1 + \text{FIOT})$  before the normalization process. Similarly, the remaining parameters have also been converted by a box-cox transformation defined as  $(x^{0.15} - 1)/0.15$  where  $x$  is the considered parameter.

This procedure allows to reduce the computational burden during the training, as well as increase the accuracy. As previously defined, hyperparameters are the parameters not directly learned within estimators and that guide the learning process for a specific database. They have been obtained by applying the random search method aiming to maximize the correlation factor on both the training and the test data sets. The optimization of hyperparameter is required for obtaining the best out of the machine learning models and the result is a single set of high-performing hyperparameters to use for configuring the models.

Three steps have been considered for validation and accuracy evaluation of 8 implemented models and will be described in the following paragraph. In the first step, the hyperparameters have been optimized, and the training dataset is fed once again to the model. Then, the validation data set is used by the model for validating the results obtained by the training set: at this point, the accuracy, in the case of untrained data, has been evaluated. Finally, the obtained model has been run with data coming from experimental papers and self-developed experiments, and the accuracy has been calculated and evaluated.

### 3.7.2 Model results and validation

In the first part of the chapter, the model target has been defined and the dataset has been prepared for implementing the machine learning selected models and a deep learning model. Before developing the models, the hyperparameters have to be optimized for driving the models' training process.

As already explained in 3.7.1, the hyperparameter optimization has been done with the random search method which turns out to be the best strategy for highly complex problems with noisy or discontinuous areas of the search space. The Random Search method has identified values of hyperparameters for each studied



model for reducing the risk of overfitting, and it has allowed applying the model correctly and efficiently also to process parameters not contained in the training and validation dataset.

The main model results concerning the optimized hyperparameters as well as the determination factors ( $R^2$ ), relevant for the training and validation dataset, are reported in Table 8. In fact, the determination of the R-square score is important for obtaining a measure of the model quality and permits to evaluate the performances of the studied models.

Table 8 - Machine learning models optimized hyperparameters and accuracy.

Model		Hyperparameters	$R^2$	
			Train set	Validation set
<i>Linear method</i>	Ridge	$\lambda = 0.6$	0.920	0.855
	Lasso	$\lambda = 0.0005$	0.921	0.852
	Elastic Net	$\lambda_1 = 0.0005, \lambda_2 = 0.9$	0.921	0.953
<i>Kernel method</i>	Kernel Ridge	$\lambda = 0.02, \gamma = 1.0$ $d = 3.0, c = 15.0$	0.985	0.970
	Support Vector Machine	$C = 0.89, \varepsilon = 0.03$ $\gamma = 1.0, d = 3.0, c = 15.0$	0.983	0.952
<i>Ensemble method</i>	Random Forest	$M = 5000$	0.995	0.971
	Gradient Boosting	$M = 6900, \delta = 0.9$ $\eta = 0.091$	0.998	0.996
<i>Neural Network method</i>	Artificial Neural Network	$\delta = 0.9, \delta = 1.0$ $\eta = 0.001$	0.993	0.992

As shown in Table 8, the relatively low determination factor by the linear methods indicates the fact that the relationship between the considered input and output parameters is not linear. Concerning the Kernel methods, both present a high determination factor during the training phase, but the kernel ridge has been found to be approximately seven times faster than fitting support vector machine. In addition to that, considering a medium-sized database on the validation set, the kernel ridge returns a higher determination factor compared to SVM. The ensemble methods consist of more than one model and achieve better performance than any single contributing model, reducing the dispersion of the predictions and increasing the robustness of the response. The best results, for both training and validation datasets, have been obtained by the Gradient Boosting approach, and the code implemented is reported in Appendix 3: below, in Table 9, the model hyperparameter ranges on which the random search approach has found the optimized values are summarized. The number of trees  $M$ , also called  $N$  Estimators value, chosen from a set range of values, determines the measure of the complexity of the model, which affects its own accuracy and its stopping criteria. Max Depth value, Min sample value, and Min samples split value define the pruning of the model trees and have been all chosen from a range of values by mean of the random search approach: pruning methodology reduces the complexity of the model, eliminating useless leaves of developed trees and avoiding trees overfitting.

Table 9 – Hyperparameters range and result of random search optimization in Gradient Boosting.

Model Parameters	RANGE VALUES	OPTIMIZED VALUES
N_ESTIMATORS (M)	1000 / 3000 / 5000 / 7000	6900
LEARNING RATE ( $\eta$ )	0.01 / 0.05 / 0.1 / 0.15 / 0.2	0.091
MAX DEPTH	2 / 4 / 6 / 8	2
MIN SAMPLES LEAF	11 / 13 / 15 / 17 / 19	15
MIN SAMPLES SPLIT	6 / 8 / 10 / 12 / 14	11

For a more comprehensive evaluation of the performances, the four best arising models (Kernel Ridge, Random Forest, Gradient Boosting, and Artificial Neural Network) are compared in Fig. 15 in terms of determination factors as well as the percentage residuals for the 76 cases of the validation set.

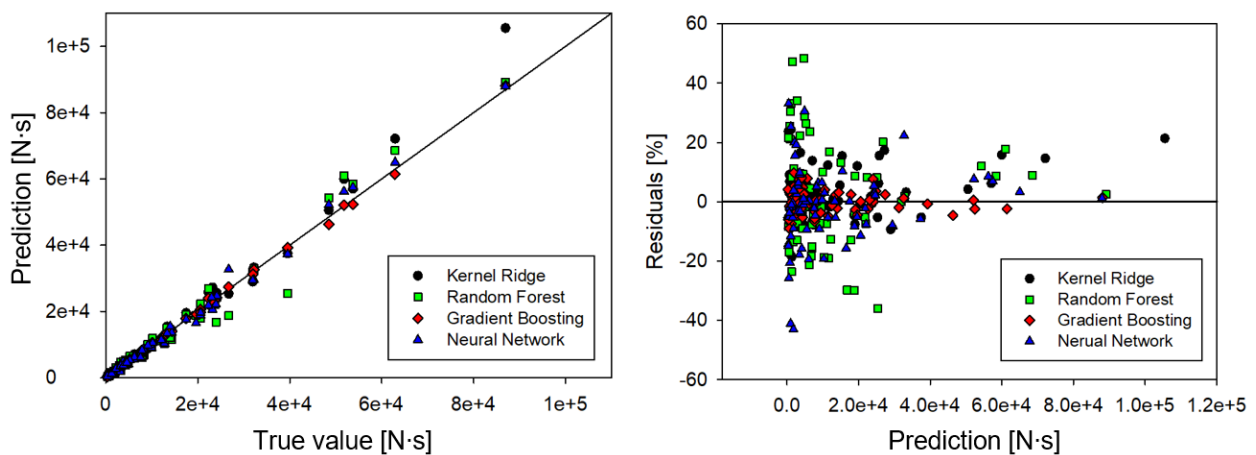


Figure 15 – (a) True value vs prediction and (b) percentage.

The analysis of the residuals, Fig. 15a, shows that, although the Kernel, Random Forest and Artificial Neural Network methods have a very high determination factor, their residuals are considerably high, especially for small prediction values. On the other hand, the Gradient Boosting method allows having low residuals for all FIOT levels. The maximum and average residuals, for the 4 methods summarized in Fig. 15, are reported in Table 10.

Table 10 – Artificial intelligence accuracy for the validation data set.

Model	Maximum residual	Average residual
Kernel Ridge	24.28%	6.93%
Random Forest	48.44%	13.08%
Gradient Boosting	9.03%	3.18%
Artificial Neural Network	43.00%	9.17%

In addition to that, the evaluation of the accuracy has been assessed by considering the three experimental ring rolling cases from the literature [14, 11, 46] and using the data for applying the three machine learning models and the deep learning model identified with the highest determination factor (Table 8). These experimental results are all relevant for experiments carried out on GH4169 nickel-based superalloy [14], the Pb-Sn alloy ring, also utilized for the finite element model validation [11], and AISI-304 steel alloy [46]. The geometrical values, the materials, and the process parameters considered are completely different from those used for implementing the models, and they have provided additional validation on the proposed models. True prediction percentage residuals for these 3 cases are summarized in Table 11.

Table 11 – Artificial intelligence accuracy for the literature experimental cases

<b>Model</b>	<b>[14] % Error</b>	<b>[11] % Error</b>	<b>[46] % Error</b>
Kernel Ridge	16.73	15.11	28.97
Random Forest	8.48	13.44	24.10
Gradient Boosting	7.01	2.09	8.00
Artificial Neural Network	7.23	6.27	9.11

The relevant process conditions for the [14, 11, 46] are different from those imputed to the FEM simulations utilized for the training of the developed models, where the same friction conditions have been considered in all the cases and reported in 3.4. Considering the accuracy results obtained with the data of the literature papers, the residuals are still remarkably good, and the computational time is almost real-time. So, by comparing the model results with the computational time of the thermo-mechanical numerical simulations, there is a considerable improvement from a range of 9 h to 3 days for the simulations to a few seconds with the machine learning model.

Considering both the residuals presented in Table 10 and the validation results in Table 11, the Gradient Boosting approach returns the best result by efficiently managing the interactions and connections between geometry, material, and process parameters in the radial-axial ring rolling process. Models that have been built in order to iteratively learn from the last prediction, as the Gradient Boosting approach and the Artificial Neural Network model, turn out to be the most efficient: in fact, taking into account the GB model, the adjusting of tree response from previous tree mistake allows to optimize the output from an unbalanced database and to avoid random chance prediction, as reported in the results of Table 10 and 11. Even if it is faster than the GB model, the RF model is more influenced by the unbalanced database problem since this kind of approach initially provides n-trees that consider different sub-datasets. Moreover, in this research, the overfitting issue that generally affects Gradient boosting approaches has been minimized by using the random search approach for hyperparameters setting.

### 3.8 Chapter 3 summary and highlights

Considering all the models presented in the previous sub-sections, some important remarks must be pointed out, as hereafter summarized.

- The material, the geometrical attributes, and the process parameters have importance on the estimation of the forming force during the RARR process;
- The use of the multivariable analysis and, in particular, of the Fit Regression approach, have permitted to find the relationship between a set of predictors and a continuous response using the ordinary least squares method. Moreover, the interaction of polynomial terms has been included, and the stepwise regression has been performed, with advantages on the statistical examination of significance for each independent variable;
- All the inputs used for implementing the stepwise regression model have been considered on the final equation: this is an affirmation of the correlation between the chosen input and the desired FIOT output;
- The multi-variable regression is limited when the aim is to find a useful, generalized model with different combinations and ranges of work. For this reason, 8 intelligence approaches have been studied and implemented;
- The ensemble method grants the best accuracy in the prediction of the FIOT, the maximum residual being equal to 9.03% with the Gradient Boosting approach;
- The validation of the GB model has been carried out on experimental results previously found in literature, where the ring geometries, materials, and process conditions were different from those used for the training of the model: the approach is efficient also outside of the training data set range;
- The application of a machine learning model has allowed a significant reduction of the time required for the estimation of the energy consumption: the calculation is almost real-time, in comparison with FEM simulations where the computational time is between 9 h (for the 650 mm final outer diameter rings) and 3 days (for 2000 mm final outer diameter rings);
- Considering a new metal forming or forging process, the presented procedure can be used for the implementation of an energy consumption model, with a creation of a new initial training dataset, specific for the analyzed process.

## **Chapter 4**

### **Process control, geometry, and energy prediction models for profiled rings**

In this chapter, the analytical model developed for the estimation of the geometrical expansion of the ring, along with the relevant validation regarding both the model and the implemented FEM simulation, are presented. In addition to that, the energy prediction model, previously developed and applied to the flat ring rolling process, has also been modified and applied to the case of an L-shape profiled ring. The relevant results are also reported in this chapter.

The analytical model starts from the study already presented in chapter 2 concerning the interactions between the process parameters of the flat ring rolling process and adapting that approach to this more complex production system. The analytical model for the prediction of the material plastic flow between the wall and the flange of rings obtained through profiled RARR process has been developed with the aim of being easy, fast, and precise to use in industrial applications. The energy predictive model, on the other hand, starts from chapter 3 assumptions and results concerning artificial intelligence approaches and generates a new specific predictive model. To this aim, a dataset of values has been used for the training and validation phase of the chosen Gradient Boosting approach.

As stated in the introduction, the purpose is to find a model that predicts the energy consumption that is valid for profiled rings. To achieve this aim, it is fundamental to start by the study of the evolution of the ring geometries in order to understand the process and the influence of process parameters. After developing the analytical model, a FE model has been set to conduct simulations for the profiled ring rolling process. The development of the numerical model starts from the assumptions and considerations reported in section 3.3 with the necessary adaptations. Different sets of process conditions and geometries have been considered as input of the analytical model and each set of data has been used as input for FEM analysis, in order to build a

dataset of parameters. Moreover, validations of the analytical model and FE model are carried out by considering previous literature experimental analysis and relative process values [13, 52, 53, 60].

This chapter is organized as follows: In the first section 4.1, the investigation conducted on profiled RARR to select the main process parameters is reported. Then in section 4.2 the process set-up and the profiled ring evolution are explained in order to introduce the developed analytical model for ring expansion. Section 4.3 is dedicated to show the FE numerical model setting on Simufact Forming software and in the following sections, 4.4 and 4.5 the literature experimental cases considered for the analytical model validation and the FE model results are reported. Then, after having implemented a database of process parameters and energy consumption resulted from FE simulations, a process energy prediction model is developed with a Gradient Boosting approach as reported in section 4.6. Finally, a summary of the main step and contents of this chapter are listed to emphasize the key points and underline the final considerations.

## 4.1 Process parameters identification

The ring rolling process is an efficient industrial solution to achieve seamless and high-performance, relatively large-scale ring-shaped components, thanks to the possibility to obtain a near-net shape with a single step and without welding or machining requirements. The required tools for this specific process remain the same used on flat RARR processes as shown in Fig.1, but differently from the flat rolling rings process, on profiled production, the deformation of the tools is applied only to a portion of the circumferential surface of the ring. A different range of cross-section shapes can be obtained from profiled RARR process, varying tools geometries, and positions: for developing the analytical model, only 3 shapes, namely external L-shape, internal L-shape, and external C-shape, have been considered as shown in Fig 16.

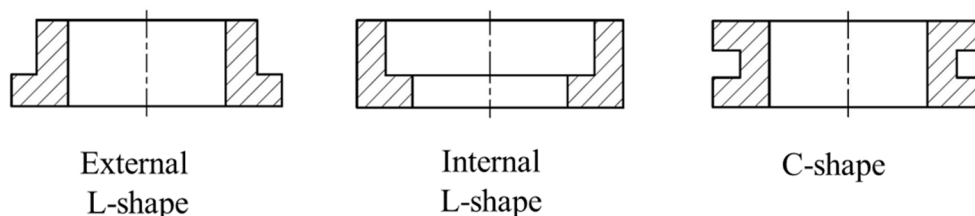


Figure 16 – Profiled shape sections considered.

As shown in Fig. 17b, on a flat ring rolling process both mandrel and main roll applies a uniform deformation on the internal and external circumferential surface of the ring: on the other hand, on an external L-shape ring rolling production the main roll works only on the upper part of the ring height (Fig. 17c), permitting the flange expansion on the lower part. Taking as further example internal L-shape ring production, the main roll acts on the whole height of the ring while the mandrel deforms the ring on the upper part of the internal surface permitting the internal expansion of the flange, as represented in Fig. 17d. Finally, the external C-shape ring section can be obtained from the ring rolling process by varying the geometry of the main roll and adding a central flange, while the mandrel and the guide rolls remain the same as per the flat ring rolling process.

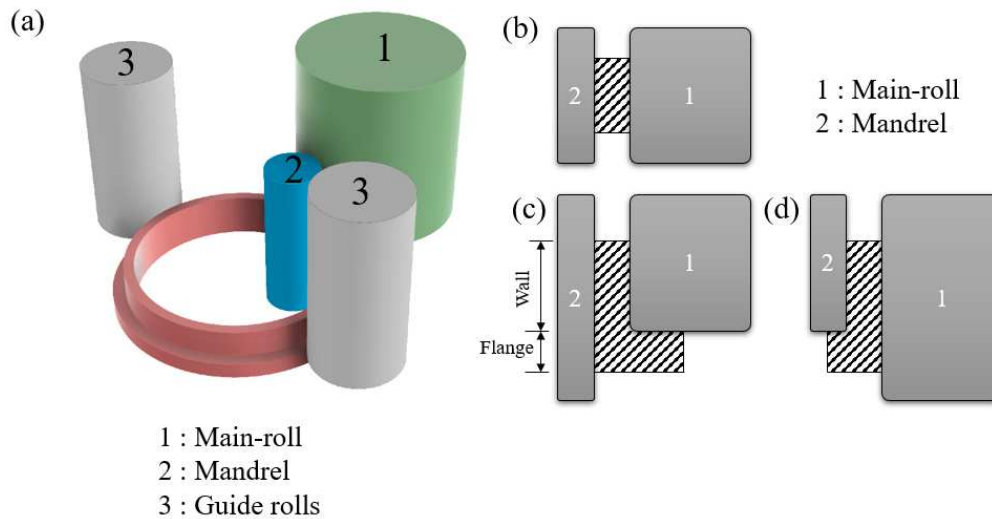


Figure 17 – (a) Schematic representation of the profiled ring rolling process and contact conditions between mandrel, main roll, and ring for (b) flat ring, (c) external flange profiled ring, and (d) internal flange in profiled rings.

The external L-shape is the main geometry considered in this research and the energy prediction model will be developed only for this profiled ring: the other two shapes, internal L-shape and C-shape have been considered for the validation of analytical and FE model through comparison with previous literature data. For this reason, only process parameters for external L-shape geometry have been deeply investigated in order to build a database of values: the other ring sections can be easily applied to the analytical model, FE simulation, and energy predictive model through the appropriate adaptations.

As in the case of the flat RARR process (chapter 3), the process parameters have been subdivided into the same macro-groups, namely speed parameters SP, initial and final ring geometries (RG), material properties (MP), and process conditions (PC) as resumed in Fig. 18. This underlines the similarity of flat (section 3.1) and profiled process parameters analysis, with the difference that, for profiled version, the number of process parameters is higher.

## Ext. L-shape Ring Model input

<p>i) <b>Initial/final Speed parameters (SP)</b></p> <ul style="list-style-type: none"> <li>- Main roll wall rotational speed;</li> <li>- Main roll flange rotational speed;</li> <li>- Mandrel feeding speed;</li> <li>- Upper axial roll feeding speed;</li> </ul>	<p>iii) <b>Initial/final ring geometries (RG)</b></p> <ul style="list-style-type: none"> <li>- Inner diameter;</li> <li>- Outer wall diameter;</li> <li>- Wall height;</li> <li>- Outer flange diameter;</li> <li>- Flange height.</li> </ul>
<p>ii) <b>Material properties (MP)</b></p> <ul style="list-style-type: none"> <li>- Flow stress (<math>\epsilon, \dot{\epsilon}, T</math>) dependence;</li> <li>- Yield strength (YS) and Young's Modulus (E) influence.</li> </ul>	<p>iv) <b>Processing conditions (PC)</b></p> <ul style="list-style-type: none"> <li>- Ring initial temperature (uniform);</li> <li>- Friction (constant);</li> <li>- Tools temperature (constant).</li> </ul>

Figure 18 – Process variable analyzed for implementing the profiled external L-shape ring model.

Concerning the speed parameters (SP), the composition is similar to the flat ring version, with the difference that main roll initial and final speeds have two different values for the wall section and for the flange section and thus a total of 8-speed parameters have been considered. For calculating main roll, mandrel and axial roll speeds, the same considerations of section 3.1 are valid with the necessary adaptations, and the main formulation adopted will be reported in the following section.

Regarding ring geometries parameters (RG), for the external L-shape ring, the initial and final inner diameters have been considered the same as in the flat ring case. On the other side, for the outer diameter and ring height, specific values for the flange section and the wall section have been considered, for a total of 10 parameters. By considering and applying the volume conservation principle, the initial and final geometries are correlated, therefore one of the geometrical values is redundant. Moreover, it should be noted that the analysis conducted for developing a profiled ring analytical model permits to consider as initial ring geometries both flat and profiled version. The last two macro-group, namely Material properties MP and Process condition PC are identical to the flat ring analysis conducted in section 3.1, with the same consideration: so, 3 parameters have been considered both for MP and PC macro-group. Concerning ring material, differently from flat analysis, only 2 materials have been considered, namely the 42CrMo4 steel alloy and Inconel 718 super alloy.

Overall, a total of 24 process parameters have been identified for defining the external L-shape profiled RARR process: in the following section, the main passages and formulations used for calculating the values of each process parameter and develop the analytical model for the profiled ring will be explained.

## 4.2 Profiled ring rolling process set-up and analytical model

The annular portion of the ring where both mandrel and main roll operate can be considered as a sub-part of the ring, called ring wall, where the contact and process conditions are the same as a flat ring rolling process [4, 7, 16]: so, the same considerations and limit conditions considered for flat ring rolling must be applied, in order to achieve the full plastic deformation along the ring wall thickness. In other words, the contact condition, the main roll speed law, and the speeds of the tools are the same considered for flat ring rolling explicated in section 3.2. Considering a linearly decreasing mandrel speed as in the flat ring rolling process, the range limits of the mandrel feeding speeds have been calculated with Eqs. (6)-(8), while the main roll wall rotational speed has been calculated with Eq. (5): this means that the expansion of the wall section is controlled and has the same expansion behavior of a flat ring.

The flange section expansion on the other hand is free since it is not controlled by any tools: in fact, the translation of the mandrel towards the main roll during the process cause a circumferential expansion of the ring as in flat RARR, and a radial expansion of the flange, since there is lower plastic flow resistance. In Fig. 19 the deformation directions of external and internal L-shape and profiled ring rolling processes are shown, to clarify the above-mentioned consideration.

As in flat ring analysis, the volume conservation principle permits defining the amount of material that is displaced from the wall to the flange section during the mandrel progress, after deducting the circumferential



volume expansion on the wall section. In order to do that, the time required for a complete rotation of a ring section must be calculated first. Eq. (28-1) defines the time for a complete rotation, and Eq. (28-2) defines the total time of the subsequent complete rotation.

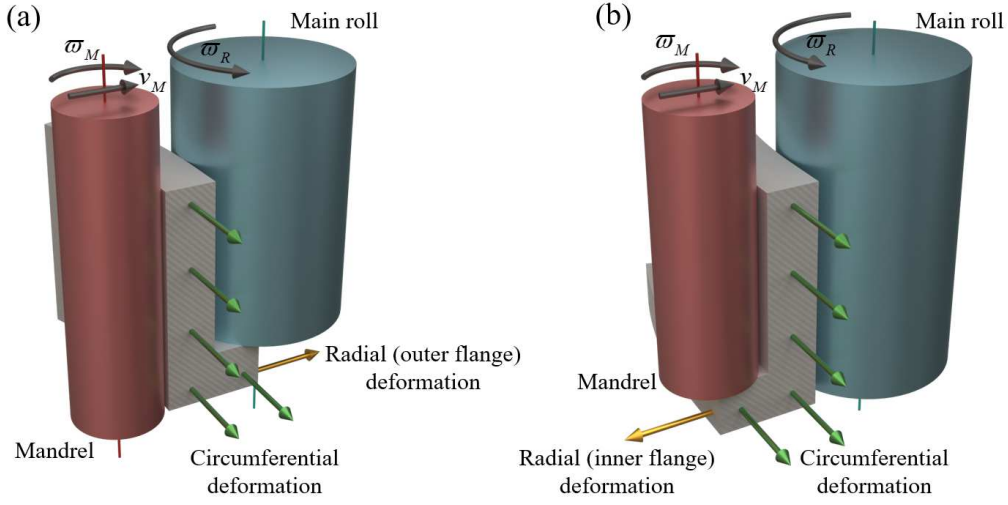


Figure 19 – Plastic deformation along the circumferential and radial (flange) directions, caused by the motions of the mandrel and the main roll, for (a) outer flange and (b) inner flange.

$$t_1 = \frac{2\pi R_{w,0}}{(\omega_R R_R)} \quad (28-1)$$

$$t_{i+1} = \frac{2\pi R_{w,i+1}}{(\omega_R R_R)} + t_i \quad (28-2)$$

where  $R_{w,0}$  and  $R_{w,i+1}$  are the initial wall radius and the new wall radius after the passage through the deformation gap, and  $R_R$  and  $\omega_R$  are respectively radius and rotational speed of the main roll. In the developed analytical model, the new process time  $t_{i+1}$  is continuously updated in order to calculate the required time for each step and the total mandrel time: this permits also to calculate the evolution of the wall thickness  $S_w$  as shown in Eq. (29): obviously, at the initial time the thickness is coincident with the initial wall thickness  $S_{w,0}$  and it is equal to the final desired wall thickness at the final mandrel time.

$$s_w(t) = s_{w,0} - \int_0^{t_j} v_M(t) dt = s_{w,0} - \left[ \frac{v_{M,0} - v_{M,F}}{t_M} \frac{(t_j)^2}{2} + v_{M,0} \cdot t_j \right] \quad (29)$$

where  $v_M$  is the mandrel feeding speed,  $t_M$  is the mandrel time and  $t_j$  is the considered revolution time. Considering two consecutive periods of a complete revolution, namely the  $i$ -revolution and the  $i+1$  revolution, and assuming a uniform evolution of the wall thickness between different complete rotation, the average thickness of ring wall at the  $i+1$  revolution have been calculated via double integration of Eq. (29) as reported in Eq. (30)

$$\bar{s}_{w,i+1} = s_{w,0} - \frac{v_{M,0}}{2} (t_{i+1} - t_i) + \frac{v_{M,0} - v_{M,F}}{6t_M} \frac{t_{i+1}^3 - t_i^3}{t_{i+1} - t_i} \quad (30)$$

where  $\bar{s}_{w,i+1}$  is the average thickness of the ring wall, representative of the incremental evolution of each ring slice. Then, the preform ring wall volume  $V_{w,0}$  has been calculated as reported in Eq. (31-1), and the updated ring wall volume  $V_{w,i}$  at the next  $i$ -revolution as in Eq. (31-2).

$$V_{w,0} = \pi(R_{w,0}^2 - R_{in,0}^2)(h_w + h_f) \quad (31-1)$$

$$V_{w,i} = \pi(R_{w,i}^2 - R_{in,i}^2)(h_w + h_f) \quad (31-2)$$

where  $R_{w,0}$  and  $R_{in,0}$  are the wall outer and inner radius of the blank ring and  $R_{w,i}$  and  $R_{in,i}$  are the updated wall outer and inner radius and finally  $h_w$  and  $h_f$  are the wall and flange height respectively. In the event of a flat blank ring, the  $R_{w,0}$  value is equal to the outer ring diameter and the volume calculated at Eq. (31-1) is the total blank volume. Moreover, in this research the height of the wall and the flange  $h_w$  and  $h_f$  have been considered as constant during the whole process: this means that the axial rolls control only the height deformations [17] and that the total height of the profiled ring does not change. Considering that deformation is only applied on the wall section of the ring, the ring wall volume variation can be calculated as in Eq. (32).

$$\Delta V_{w,i} = 2\pi\lambda h_f (\bar{s}_{w,i} - \bar{s}_{w,i+1}) \left( \bar{R}_{w,i} - \left[ \frac{(\bar{s}_{w,i} - \bar{s}_{w,i+1})}{2} \right] \right) \quad (32)$$

$$\text{where } \lambda = (\pi/2)h_f/(h_w + h_f)$$

where  $\lambda$  is a geometrical factor that considers the relationship between the flange height and the wall height values. In fact, higher flange height to wall height ratios leads to a lower material flow resistance in the circumferential direction, instead of the radial direction. Combining equations (29), (31-2), and (32) it is possible to calculate the average radius of the ring wall  $\bar{R}_{wc,i+1}$  at the  $i+1$  revolution, as reported in Eq. (33)

$$\bar{R}_{wc,i+1} = \frac{[V_{w,i} - \Delta V_{w,i}]}{2\pi\bar{s}_{w,i+1}(h_w + h_f)} \quad (33)$$

The average radius of the ring wall  $\bar{R}_{wc}$  represent the spatial averaging across the circumference of the ring, of the wall cross-section radius: it has been represented in the middle cross-section of the ring wall in Fig. 20.

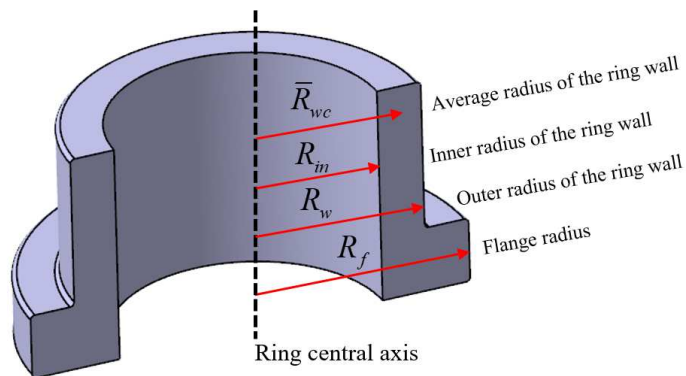


Figure 20 – Flanged ring diameters identification on a generic ring cross-section.

From the average radius of the ring wall  $\bar{R}_{w,i+1}$  at the i-th+1 revolution, it has been calculated the inner and outer wall radii of the ring, as shown in Eq. (34-1) and Eq. (34-2):

$$R_{in,i+1} = \bar{R}_{w,i+1} - \frac{\bar{s}_{w,i+1}}{2} \quad (34-1)$$

$$R_{w,i+1} = \bar{R}_{w,i+1} + \frac{\bar{s}_{w,i+1}}{2} \quad (34-2)$$

With these two geometrical parameters, the wall volume at the i-th+1 revolution has been calculated according to Eqs. (31). This permits also to estimate the volume variation from the i-th period to the i-th+1 period: considering the already mentioned volume conservation assumption, the ring wall volume variation has been considered as the material portion that has moved to the flange section and can be calculated as shown in the following Eq. (35):

$$R_{f,i+1} = \sqrt{\frac{V_{w,0} - V_{w,i+1}}{\pi h_f} + R_{w,i+1}^2} \quad (35)$$

By means of this set of equations, the profiled ring geometrical evolution can be predicted from the ring preform at the instant  $t_0$ , through consecutive instant  $t_i$  and  $t_{i+1}$ , to the final mandrel time  $t_m$ . The algorithm has been implemented on an Excel spreadsheet to provide a fast and easy instrument to check the ring evolution during the process and to calculate all the necessary data to implement and control a numerical simulation model.

### 4.3 Finite element model implementation

For the verification of the developed algorithm, numerical simulations have been carried out and literature experiments have been used, since the experimental verification was not possible with a laboratory test. The numerical simulations have been run by utilizing the commercial software Simufact Forming 16. The explanation of the model set is presented in 4.3.1, whereas the validation of the FEM model is described in 4.3.2, by comparing experimental papers and FEM literature results with the analytical and FEM results. The accuracy verification of the flanged ring expansion prediction algorithm has been carried out by two different separate instigations that reinforce the validity of the proposed model and are described in 4.3.3.

#### 4.3.1 Model setting

In order to further investigate the effect of the profiled ring rolling parameters on the geometrical evolution of the ring and also on the energy consumption, FEM simulations have been implemented in Simufact Forming. In addition to that, the FEM solutions have been also utilized to determine the accuracy in the prediction of the geometrical expansions of profiled rings, and, for this reason, it has been validated against literature FEM and experimental results. The general simulation settings defined in this section have been considered in all the implemented FEM simulations relevant for the profiled ring rolling process, with the exception of the process parameters, which vary from case to case.

In order to analyze the influence of the mesh size on the simulations results, four different mesh studies have been conducted for identifying the best compromise between accuracy and computational time. The result of this analysis has been detected in i) 1 element every  $1^\circ$  for the circumferential direction, ii) 1 element every 2.5mm for the radial direction and iii) 1 element every 2.5 mm for the vertical direction. In the same way, as flat ring rolling process, the tools have been considered as rigid with heat transfer and meshed with 3D arbitrarily distorted 8-nodes first order isoparametric, heat transfer element (MARC® element type 43). A representation of the implemented FEM model is shown in Fig. 21.

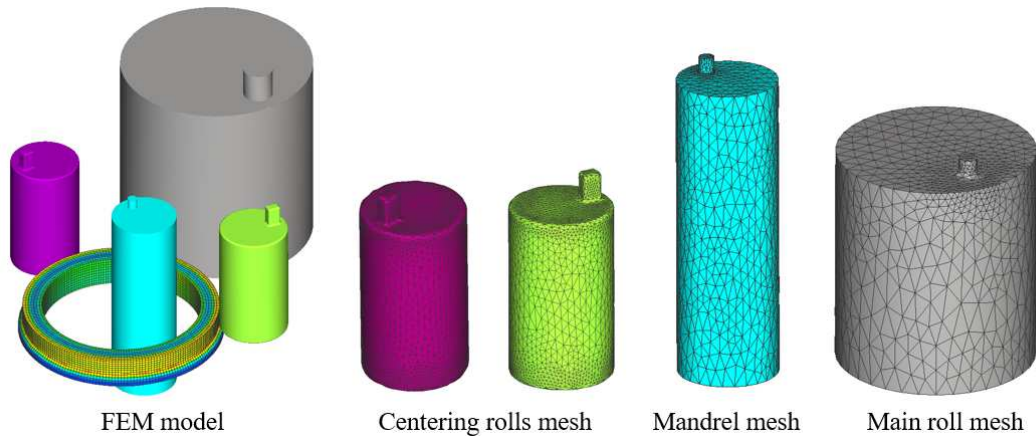


Figure 21 – Thermo-mechanical finite element simulation model implementation.

Considering both the FEM simulations and the literature cases that have been used for the validation, the friction has been modeled considering the shear friction law, described in section 3.3. During the contact process between the tools and the ring, friction is involved, and in order to overcome the discontinuity of friction when relative velocity is zero, a nonlinear arctangent smoothing function, based on the relative sliding velocity between contact bodies, has been defined adopting a threshold of 0.001 mm/s for the relative velocity below which sticking is simulated.

The employed solver for the simulations is the Multifrontal Massively Parallel sparse direct Solver (MUMPS), which implements a direct method based on a multifrontal approach, which performs a Gaussian factorization. The kinematics of deformation is formulated according to the updated Lagrangian approach for the estimation of the node displacement calculation. The updated Lagrangian approach is particularly indicated in case of large deformation such as the case of both circumferential and flange growths in the profiled ring rolling.

The setting of the materials and the boundary conditions are the same employed on the experimental papers considered for validating the FEM model: in this manner, the simulation is as close as possible to experimental conditions and thus the validity of the model can be effectively verified. On the other hand, for the validation of the implemented algorithm have been considered two materials already used for the flat ring rolling FEM simulations, namely the steel (42CrMo4) and Inconel 718 super alloy, as it will be presented in 4.3.3.

### 4.3.2 Validation of the FEM model

In order to enhance the reliability of the model validation, the developed numerical model has been priority validated by comparing its results with literature experiments, and the detailed results comparison is presented here below. For obtaining a validation as complete as possible, the FEM results have been validated by considering different initial shapes of the ring, such as rectangular section and profiled preform [13], and different final shapes such as inner L-flange [52], outer L-flange [53], and C-grooved rings [60]. The first experiment considered has been conducted starting from a profiled preform, as shown in Fig. 22a with the aim to obtain an external L-shape, shown in Fig. 22b.

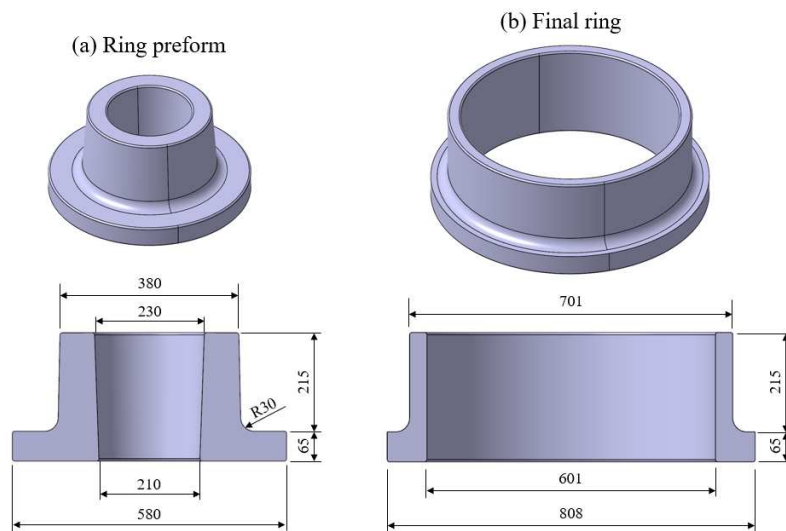


Figure 22 – (a) Initial and (b) final geometry of the authors’ validation case (Monti and Berti [13]).

The ring rolling machine dimensions, and the process settings relevant for both the real production as well as for the implemented FEM model are reported in Table 12.

Table 12 - Ring rolling mill dimensions, initial and final ring geometries, and process settings for the authors’ validation cases [13].

Parameters	Value
Main-roll radius [mm]	100
Mandrel radius [mm]	50
Guide rolls radius [mm]	75
Initial ring temperature [°C]	1240
Initial tools temperature [°C]	400
Friction coefficient	0.15
Main-roll rotational speed [rad/s]	6.28
Initial ~ Final mandrel feeding speed [mm/s]	1 ~ 0.58

This first experiment allows an accurate and detailed validation of the developed FEM simulation model, since the material and the process conditions are similar to those used for investigating the accuracy of the

implemented algorithm and that will be described in 4.3.3. In fact, the material used for the experiment is the 42CrMo4 steel and the friction, as well as the process setting, are the same considered in [13]. Moreover, considering as an initial blank a profiled preform, as shown in Fig. 22a, the model allows showing the reliability of the proposed algorithm in predicting the geometrical expansion of flanged rings also for a different type of initial preform shape.

Concerning the validation of the FEM model with inner L-shape geometry, since both radial force and initial/final geometries of the ring are available, the FEM results concerning the radial forming force and the experimental results relevant for the geometry of the ring, in terms of inner and outer wall radii and flange radius, have been compared with the relevant analytical and FEM results obtained.

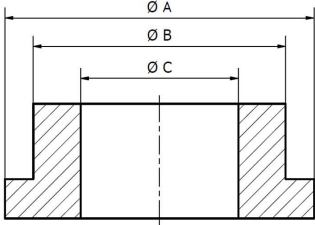
The material considered in this validation is the BS EN 12588 lead, where the stress-strain has been evaluated by the authors of the paper [52] with a tensile test and the response results have been found to be similar to hot forming aluminum or steel. In Fig. 23 is represented the true stress-strain curves at 0.2/s and 0.02/s and flow stress interpolation curves for the lead alloy and used for predicting the force with the Hollomon Eq. (36).

$$\sigma = K \varepsilon^n \quad (36)$$

where  $\sigma$  represents the applied true stress on the material,  $\varepsilon$  is the true strain, and  $K$  is the strength coefficient.

The simulation has been set with the same mesh and solver described in 4.3.1. In the Table 13 are summarized the ring rolling mill dimensions, the initial and final ring geometries and the process conditions relevant for the validation.

Table 13 - Ring rolling mill dimensions, initial and final ring geometries, process settings for the validation case, and external L-shape ring representation [52].

Parameters	Literature case [52]
Main-roll radius [mm]	100
Mandrel radius [mm]	45
Initial ring outer diameter [mm]	196
Initial ring wall thickness [mm]	41.5
Initial ring flange thickness [mm]	41.5
Initial ring height [mm]	46.5
Final ring wall thickness [mm]	15.1
Final ring flange thickness [mm]	30.2
Final ring wall height [mm]	17.55
Final ring flange height [mm]	23.25
Diameter A [mm]	270
Diameter B [mm]	239.8
Diameter C [mm]	209.6
Thickness reduction per rev. [%]	4
Final shape schematic reference	

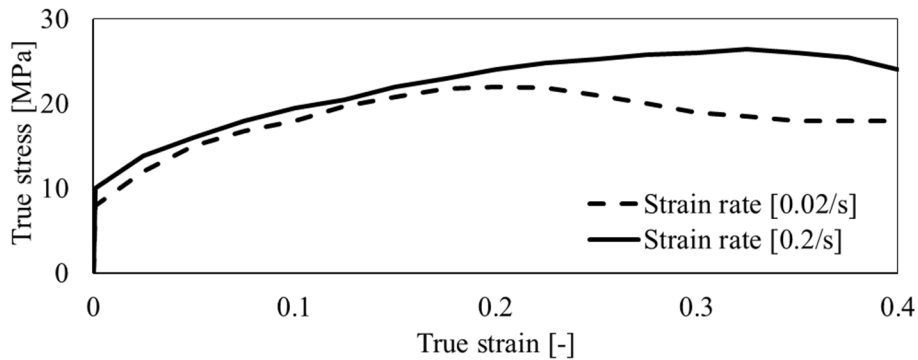
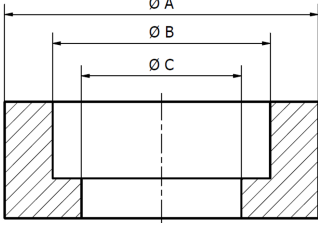


Figure 23 – True stress-strain curves at 0.2/s and 0.02/s and flow stress interpolation curves for the BS EN 12588 lead alloy [52].

Concerning the validation of the FEM model with outer L-shape geometry, the only result reported in the considered paper [53] is the geometrical expansion of the ring. Due to this, the comparison has been carried out between the final diameters of the cited paper [53] on one side, and the modeled analytical and FEM results on the other. Same way as reported in [52], the mesh and solver has been chosen as described in 4.3.1 and the material involved is the BS EN 12588 lead. Table 14 includes the main ring rolling mill dimensions, the initial and final ring geometries, the process settings for the validation and a representation of the final internal L-shape of the ring.

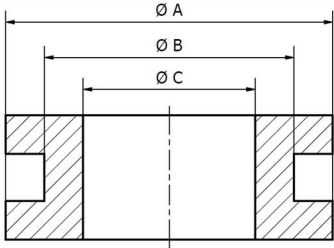
Table 14 - Ring rolling mill dimensions, initial and final ring geometries, process settings for the validation case, and internal L-shape ring representation [53].

Parameters	Literature case [53]
Main-roll radius [mm]	100
Mandrel radius [mm]	45
Initial ring outer diameter [mm]	222.6
Initial ring wall thickness [mm]	40.1
Initial ring flange thickness [mm]	40.1
Initial ring height [mm]	44.4
Final ring wall thickness [mm]	15
Final ring flange thickness [mm]	18
Final ring wall height [mm]	26.4
Final ring flange height [mm]	18
Diameter A [mm]	396
Diameter B [mm]	376
Diameter C [mm]	346
Thickness reduction per rev. [%]	1
Final shape schematic reference	 <p>The diagram shows a cross-section of a ring with a central hole. Three diameters are indicated: Ø A is the outer diameter, Ø B is the diameter of the inner hole, and Ø C is the diameter of the inner groove. The ring is shown as a double-symmetric L-shape with hatched areas on the left and right sides.</p>

Concerning the validation of the FEM model with double L-shape (C-shape) geometry, the experimental research used as reference is by Liang et al. [60]. The ring is defined as a double-symmetric L-shape grooved ring, as shown in Table 15, and is manufactured with the Inconel 718 superalloy, also utilized in this thesis for the flat ring analysis and in the finite element investigation cases presented in the following section (4.3.3). Also for this validation, the principal values concerning the ring rolling mill dimensions, the initial and final geometries, and the process settings are summarized in Table 15.



Table 15 - Ring rolling mill dimensions, initial and final ring geometries, process settings for the validation cases, and C-shape ring representation [60].

Parameters	Value
Main-roll radius [mm]	570
Mandrel radius [mm]	150
Guide rolls radius [mm]	150
Initial ring temperature [°C]	1000
Tools temperature [°C]	150
Friction coefficient	0.3
Initial ring outer diameter [mm]	756.4
Initial ring inner diameter [mm]	456.4
Initial ring height [mm]	223.1
Final ring wall thickness [mm]	60.8
Final ring flange thickness [mm]	101.5
Final ring wall height [mm]	82.5
Final ring total height [mm]	223.1
Diameter A [mm]	1164.3
Diameter B [mm]	1082.9
Diameter C [mm]	961.3
Main-roll rotational speed [rad/s]	1.1
Mandrel feeding speed [mm/s]	0.3
Final shape schematic reference	

### 4.3.3 FEM investigation cases set up

The proposed flanged ring expansion prediction algorithm has been investigated in detail with two different analyses that are named, for simplicity and convenience, investigation A and B. In this paragraph, the two investigations' settings, objectives, and reasons will be presented.

The main aim of investigation A is to analyze and to understand the influence of the speeds of the tools on the setting choice of the model and in the definition of the geometry. For doing this investigation, three different initial and final ring configurations have been coupled with three different main roll rotational speeds. For each main roll rotational speed, three initial and final mandrel feeding speed sets have been considered.

The final ring outer flange covers a range from ~500 mm to ~1100 mm and the three main roll rotational speeds that were chosen are 2 rad/s, 3 rad/s, and 4 rad/s. The mandrel feeding speeds have been calculated by the Eqs. (3)-(5) described in 3.2, and for each combination of geometry and main roll rotational speed, the lower range, the middle, and the upper on the range values were considered. In total, 27 simulations have been run and all the initial and final ring geometries, the main roll rotational speeds, the mandrel feeding speeds,

and the process parameters are summarized in Table 16. All the simulations have been defined to maintain the same gear ratio between the ring and the tools, thus the outer diameters of the mandrel and main roll have been changed according to the initial geometry of the considered ring.

Table 16 - Initial and final ring geometries, the main roll rotational speeds, the mandrel feeding speeds, and the process parameters settings for investigation A.

<b>Parameters</b>	<b>Ring#1A</b>								
Main-roll radius [mm]	270								
Mandrel radius [mm]	90								
Initial ring outer diam. [mm]	235								
Initial ring wall thickness [mm]	90								
Initial ring height [mm]	145								
Final ring wall thickness [mm]	54								
Final ring flange thickness [mm]	72								
Final ring outer flange diam. [mm]	564								
Final ring outer wall diam. [mm]	528								
Final ring internal diam. [mm]	420								
<b>Sub-case numbering</b>	<b>A1-1</b>	<b>A1-2</b>	<b>A1-3</b>	<b>A1-4</b>	<b>A1-5</b>	<b>A1-6</b>	<b>A1-7</b>	<b>A1-8</b>	<b>A1-9</b>
Main-roll rotational speed [rad/s]	2			3			4		
Initial mandrel feeding speed [mm/s]	0.26	1.88	3.33	0.4	2.86	5.08	0.54	3.85	6.84
Final mandrel feeding speed [mm/s]	0.16	1.75	3.19	0.24	2.68	4.86	0.33	3.6	6.54
Mandrel active time [s]	139	19.2	10.8	90	12.6	7.08	66.7	9.34	5.26
Total process time [s]	160	25.2	15.2	105	16.8	12.3	74.5	13.9	9.8

<b>Parameters</b>	<b>Ring#2A</b>								
Main-roll radius [mm]	375								
Mandrel radius [mm]	125								
Initial ring outer diam. [mm]	325								
Initial ring wall thickness [mm]	120								
Initial ring height [mm]	145								
Final ring wall thickness [mm]	72								
Final ring flange thickness [mm]	96								
Final ring outer flange diam. [mm]	802								
Final ring outer wall diam. [mm]	754								
Final ring internal diam. [mm]	610								
<b>Sub-case numbering</b>	<b>A2-1</b>	<b>A2-2</b>	<b>A2-3</b>	<b>A2-4</b>	<b>A2-5</b>	<b>A2-6</b>	<b>A2-7</b>	<b>A2-8</b>	<b>A2-9</b>
Main-roll rotational speed [rad/s]	2			3			4		
Initial mandrel feeding speed [mm/s]	0.35	2.7	4.8	0.5	4	7.2	0.7	5.5	9.7
Final mandrel feeding speed [mm/s]	0.2	2.4	4.37	0.3	3.6	6.65	0.4	4.9	8.9
Mandrel active time [s]	140	18.15	10.21	98	12.25	6.79	70	8.91	5.05
Total process time [s]	158	22.9	15.2	108	16.5	11.2	76.3	13.6	9.7

Parameters	Ring#3A								
Main-roll radius [mm]	490								
Mandrel radius [mm]	165								
Initial ring outer diam. [mm]	425								
Initial ring wall thickness [mm]	160								
Initial ring height [mm]	145								
Final ring wall thickness [mm]	96								
Final ring flange thickness [mm]	128								
Final ring outer flange diam. [mm]	1011								
Final ring outer wall diam. [mm]	947								
Final ring internal diam. [mm]	755								
<b>Sub-case numbering</b>	<b>A3-1</b>	<b>A3-2</b>	<b>A3-3</b>	<b>A3-4</b>	<b>A3-5</b>	<b>A3-6</b>	<b>A3-7</b>	<b>A3-8</b>	<b>A3-9</b>
Main-roll rotational speed [rad/s]	2			3			4		
Initial mandrel feeding speed [mm/s]	0.46	3.45	6.14	0.7	5.26	9.37	0.94	7.08	12.59
Final mandrel feeding speed [mm/s]	0.28	3.22	5.87	0.43	4.92	8.96	0.58	6.62	12.05
Mandrel active time [s]	139.5	18.55	10.42	91.34	12.16	6.83	67.92	9.04	5.08
Total process time [s]	159.5	24.5	15.2	97.8	16.5	11.7	76.2	14.5	9.7

The second analysis, called investigation B, aims to understand the performances of the proposed developed algorithm on the prediction of different flange expansion, considering the same initial preform shape. For doing this analysis, 3 different initial geometries have been considered, and for each geometry, 3 different percentages of flange reduction, for a total of 9 rings. The initial and final geometries for the considered rings, the geometry of the ring rolling mill, and additional process settings relevant for each case are shown in Table 17.

In Table 17, the wall thickness reduction is defined as the percentage reduction of the initial wall of the ring because of the deformation carried out by the mandrel. Besides, the flange protrusion from the initial wall thickness represents the percentage increase in the flange thickness from the initial wall thickness.

Investigation A has been carried out considering the Inconel 718 super alloy whereas, for investigation B, the 42CrMo4 steel alloy has been additionally considered. For the latter case, the kinematic process settings, obtained by applying the proposed algorithm, have been kept constant and only the initial temperature of the ring has been changed according to the higher processing temperature for the 42CrMo4 steel alloy under hot forming conditions. In the FEM simulations, the ring has been set with an initial temperature equal to 1030 °C for the Inconel 718 rings and 1200 °C for the 42CrMo4 rings, respectively.

The material properties have been acquired from the material library available in Simufact Forming 16, directly originated from the MATILDA® (Material Information Link and Database Service) archive. Concerning the plastic behavior, the Hasel-Spittel flow stress model [88], Eq. (37) has been utilized and the model constants for the two above-mentioned materials are reported in Table 18.

$$\sigma = C_1 e^{(C_2 \cdot T)} \varepsilon^{(n_1 \cdot T + n_2)} e^{\left(\frac{L_1 \cdot T + L_2}{\varepsilon}\right)} \dot{\varepsilon}^{(m_1 \cdot T + m_2)} \quad (37)$$

Table 17 - Ring rolling mill dimensions, initial and final ring geometries, and process settings for the investigation B.

Parameters	Ring #1B	Ring #2B	Ring #3B	Ring #4B	Ring #5B	Ring #6B	Ring #7B	Ring #8B	Ring #9B
Main-roll radius [mm]	270			375			490		
Mandrel radius [mm]	90			125			165		
Wall thickness reduction [%]	70%	60%	50%	70%	60%	50%	70%	60%	50%
Flange protrusion from initial wall thickness [%]	10%	20%	30%	10%	20%	30%	10%	20%	30%
Initial ring outer diam. [mm]	235			325			425		
Initial ring wall thickness [mm]	90			120			160		
Initial ring height [mm]	145			145			145		
Final ring flange thickness [mm]	72			96			128		
Final ring wall thickness [mm]	63	54	45	84	72	60	112	96	80
Final ring outer flange diam. [mm]	519	564	619	712	802	852	926	1011	1106
Final ring outer wall diam. [mm]	501	528	565	688	754	780	894	947	1010
Final ring internal diam. [mm]	375	420	475	520	610	660	670	755	850
Final ring flange height [mm]	50								
Final ring wall height [mm]	95								
Main-roll rotational speed [rad/s]	4	4	4	4	4	4	4	4	4
Initial mandrel feeding speed [mm/s]	6.88	6.84	6.79	9.8	9.7	9.72	12.67	12.6	12.52
Final mandrel feeding speed [mm/s]	6.82	6.54	6.16	9.6	8.9	8.67	12.6	12.05	11.38
Mandrel active time [s]	3.92	5.26	6.63	3.67	5.05	6.17	3.79	5.08	6.39
Total process time [s]	5	6.5	8	5	6.5	7.5	4.5	6.5	8

Table 18 - Material constants and validity range for the Inconel 718 and 42CrMo4.

<b>Parameter</b>	<b>Inconel 718</b>	<b>42CrMo4</b>
Temperature range for the model [°C]	950 ~ 1100	800 ~ 1250
Strain range for the model [-]	0.05 ~ 2	0.05 ~ 2
Strain rate range for the model [1/s]	0.01 ~ 150	0.01 ~ 150
$C_1$	10501.100	5290.5
$C_2$	-0.0030755	-0.0036967
$n_1$	-0.0001815	-0.0003340
$n_2$	0.543976	0.206120
$L_1$	-2.17606e-5	-8.26584e-5
$L_2$	0.0237644	0.0289085
$m_1$	-2.67316e-6	0.0003007
$m_2$	0.0974653	-0.1561810

Finally, for both investigations A and B, the friction has been set according to the shear friction law already described in 3.3, with the  $m=0.85$  for the contact between the main roll and mandrel with the ring whereas  $m=0.6$  for the contact between axial rolls and guide rolls with the ring.

#### 4.4 FEM and model validation results

The numerical simulation study cases carried out for validating the FEM model and of the developed analytical model have been presented in 4.3 and their results will be described in the following paragraph. The first part will cover the results of the 4-analysis made for validating the FEM and analytical model, and then all the results of the two investigations on the behavior of the implemented model will be presented.

The first validation has been carried out by comparing a FEM result with a FEM and an experiment made by Monti et al. [13] in a ring rolling company. Thanks to this comparison the FEM model has been verified in terms of accuracy on the prediction of geometrical expansion of the ring throughout the process. Moreover, this analysis allows to verify the validity of the proposed analytical model in the case of a non-annular initial preform.

In Fig. 24a, the mandrel force obtained during the experiment has been compared with the FEM model implemented in Simufact Forming 16, where the variation of the radial force can be explained by the presence of an initial flange on the process. As concerns the experimental results, the presence of sudden variation of the radial forming force is caused by several factors, among them the presence of oxidation scale forming and detaching from the ring surface during the production, the variation of the lubrication conditions during the process as well as variation of the hydraulic pressure keeping the contact between the mandrel and the ring. Although some deviations between experimental and FEM results can be seen from the results presented in Fig. 24a, the overall trend is well followed, and the average deviation is calculated in 14.8%. The average deviation has been calculated considering 20 points between 0s and 48s (which is the final process time) and comparing the experimental results with the FEM results.

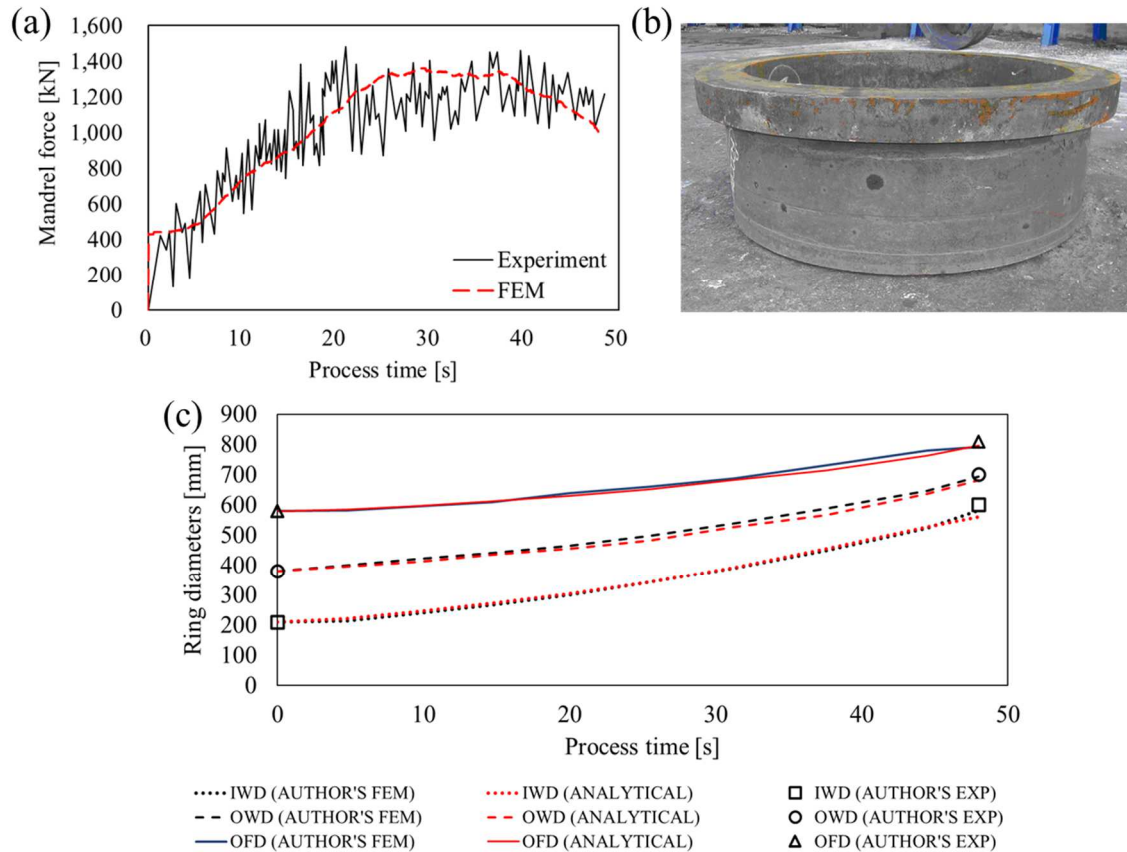


Figure 24 – (a) Comparison between authors' FEM and experimental results for the main roll forming force and (b) final ring at the end of the ring rolling process. (c) Cross-comparison of FEM, analytical and experimental results comparisons.

The L-shape final ring obtained with the experiment is represented in Fig. 24b and the final measure achieved is summarized in Table 19, showing a good agreement among experimental, FEM, and analytical results. As concerns the material redistribution in profiled rings, even when starting from a non-annular preform, the maximum deviation obtained comparing the analytical model with the experiment is 4.9 % for final inner wall diameter. Moreover, the proposed algorithm can be utilized for an initial screening phase to investigate the influence of process and geometrical parameters on the geometrical expansion of the ring. The results accuracy of analytical and FEM solutions compared to experiment, as reported in Table 19, permits to rely on FEM analysis only in a further step, thus gaining time since the estimation carried out by the proposed algorithm is almost real-time.

The second analysis that has been done to validate the FEM simulation model, considers a ring with an outer L-flange final shape [52]. For the FEM model implementation, the material properties, geometries, and process conditions reported in section 4.3.2 have been utilized. The comparison between the experimental and FEM mandrel forming force results shown a maximum deviation of 3.3 % (Fig. 25). The peak in the mandrel forming force noticeable around 39 mm of the evolution axis is due to the collision between the mandrel and one of the centering rolls, an issue that might happen in the first stages of the process.

Table 19 – Comparison among analytical, finite element, and experimental results for the literature case [13].

Models and experiment comparison	Final ring dimensions		
	Inner wall diameter [mm]	Outer wall diameter [mm]	Final outer diameter [mm]
EXPERIMENT [13]	601	701	808
FEM	581.8	693.4	792.4
ANALYTICAL MODEL	571.7	681.7	796.1
EXP vs FEM deviation [%]	3.2	1.1	1.9
EXP vs ANALYTICAL deviation [%]	4.9	2.8	1.5

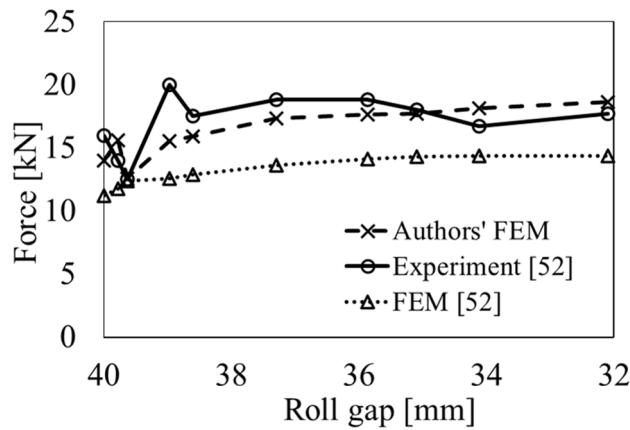


Figure 25 – Comparison between authors' FEM simulation result and literature [52] experiment and FEM results for the mandrel forming force.

The inner and outer ring wall diameters and flange diameter of the experiment [52] have been analyzed and the FEM model and analytical calculations results have been compared, as shown in Fig. 26. This comparison allowed estimating the deviations in 1.05% for the ring outer wall diameter (OWD), 1.2% for the ring inner wall diameter (IWD), and 2.5% for the inner flange diameter (IFD). Additionally, FEM and analytical model results are very close during the evolution process. The good agreement between the FEM and literature experiments implies that the implemented FEM simulation is reliable in replicating the deformation behavior throughout the process.

The third analysis that has been done for obtaining a further validation of the FEM simulation model, considers an inner L-shape ring [53]. The comparison between the FEM simulation model, the analytical model, and the literature experimental result, shown that the deviations that are minimal as reported in Fig. 27. In Fig. 27, the roll gap represents the distance between the mandrel and the main roll in the wall portion of the ring height. This comparison allowed estimating the deviations in 1.1% for the ring outer flange diameter (OFD), 1.4% for the ring inner wall diameter (IWD), and 0.75% for the outer wall diameter (OWD). Also in this third validation case, the FEM model and analytical solutions well agree both for the final values at the end of the process time (minimum value of the roll gap) as well as during the ring expansion process.

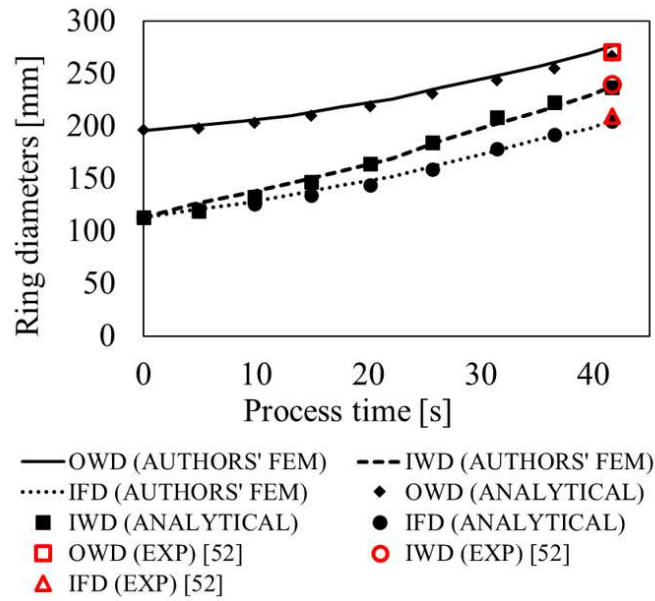


Figure 26 – Comparison between authors’ analytical and FEM solutions with the literature [52] experimental results for the expansion of inner flange diameter (IFD), inner wall diameter (IWD), and outer wall diameter (OWD), for decreasing roll gap.

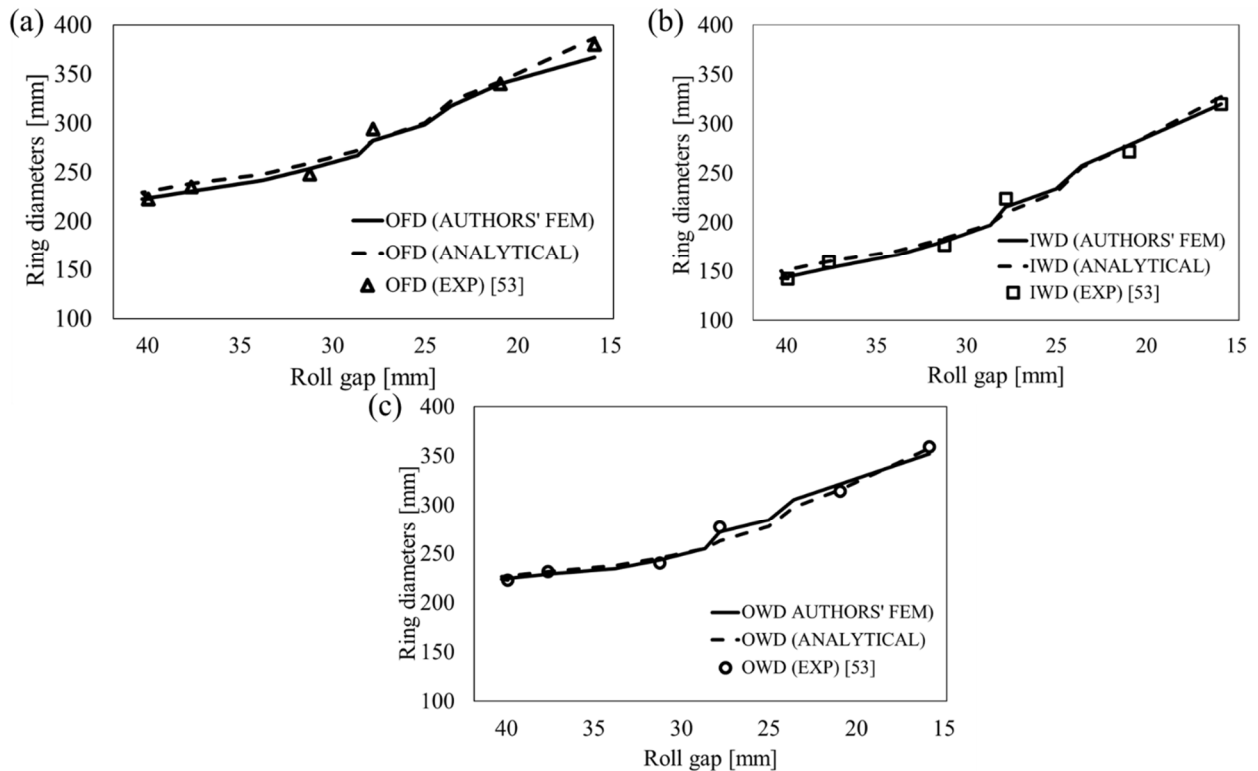


Figure 27 – Comparison between authors’ analytical and FEM solutions with the literature [53] experimental results for (a) the expansion of outer flange diameter (OFD), (b) inner wall diameter (IWD) and (c) outer wall diameter (OWD) for decreasing roll gap.

The last validation is related to the experimental case presented in Liang et al. [60] for a ring with a final C-shape symmetric along the horizontal direction. The results have been compared and plotted in Fig. 28, and



the average deviations between the analytical predictions and the literature experimental results are 0.5% for flange diameter (OFD), 3.6 % for inner wall diameter (IWD), and 2.9% for the outer wall diameter (OWD). Also, in this case, the accuracy in the prediction of the ring expansion of profiled rings has been validated.

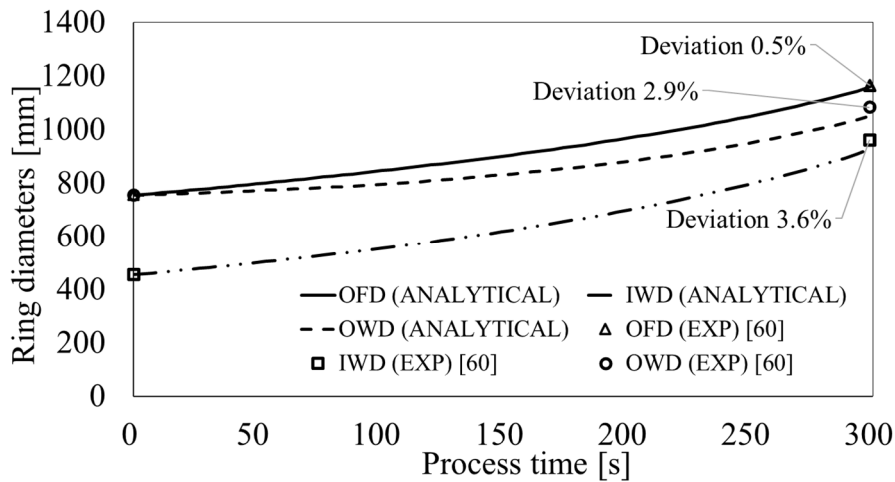


Figure 28 – (a) Comparison between authors' analytical solution and literature [60] experimental results for the expansion of outer flange diameter (OFD), inner wall diameter (IWD), and outer wall diameter (OWD) vs the process time.

Finally, considering the results of the analysis described above, it is possible to conclude that the implemented FEM solution is capable of properly replicating the profiled ring rolling process. Therefore, with the aim of analyzing in detail the accuracy of the developed algorithm as well as showing some of the main correlations present between process settings and ring geometrical expansion, the results of the two investigations A and B, already introduced in 4.3.3, are presented here below and validated with FEM model.

Regarding the results of investigation A, the 27 simulation results have been analyzed and compared with the analytical prediction, and a representation of the influence of the tools speeds on the accuracy of the ring geometry prediction algorithm and on the force integral of mandrel active time are shown in Fig. 19.

In Fig. 19a, the dimensionless parameter on the x-axis is represented by the ratio between the average mandrel feeding speed and the main roll rotational speed. The maximum and average deviations between analytical predictions and FEM results are equal to 11.6% and 6.73%, evidence that the implemented algorithm is accurate for a wide range of main roll rotational speeds and relevant initial and final mandrel feeding speeds. The analysis of the error behavior shows that it tends to drop with increasing x-axis values (ratio between the average mandrel feeding speed over the main roll rotational speed).

Considering the hot forging conditions of the process, the incremental variation during the ring evolution of the ring rolling process, and the above reported Eqs. (3)-(5) to define the mandrel initial and final feeding speed, it has been assumed that with higher main roll rotational speed, the process time necessary to reach the final ring geometry decreases. For this reason, the decreasing temperature has not been considered on the analytical model, differently as in the FEM simulations, since it has a smaller influence on the material flow stress. In the case of a low rotational speed of the main roll, on the other hand, the process time increases

causing a significant temperature drop on the ring, resulting in a variation of the material properties during the whole process.

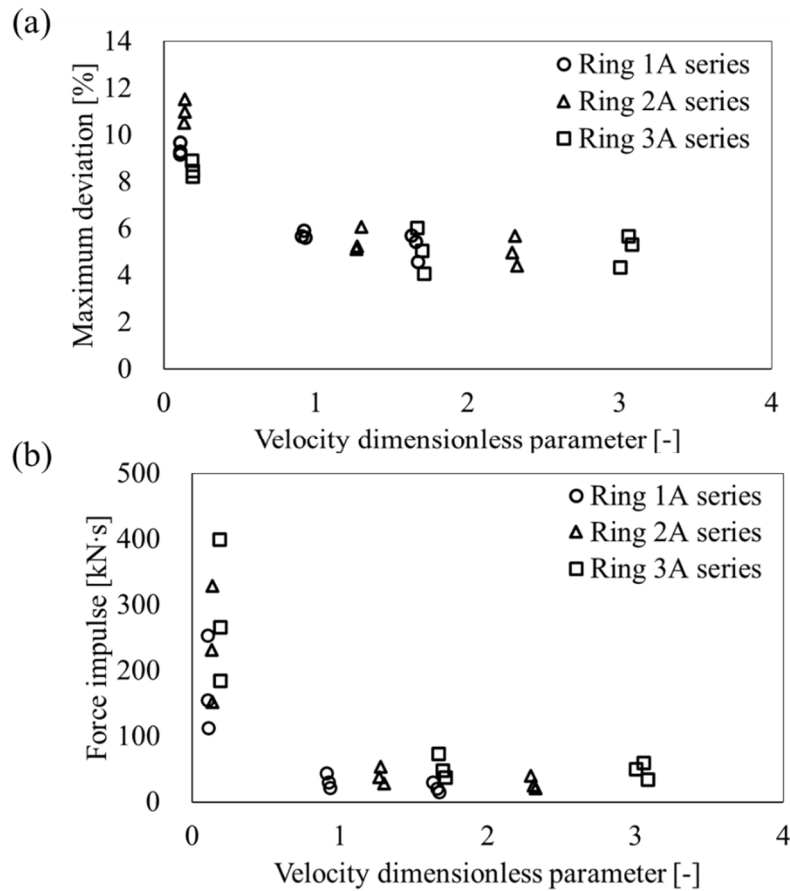


Figure 29 – Influence of the main roll rotational speed and initial and final mandrel feeding speeds on the accuracy of the ring geometry prediction algorithm and on the force integral of mandrel active time (results for investigation A).

The values of the force impulse, defined as the integral of mandrel force over the mandrel feeding time, have been considered as an indicator of the algorithm performance, as represented in Fig. 29b. In the last graph of Fig. 29, it is important to notice that with a high main roll rotational speed and high initial and final mandrel feeding speeds, a minimization of the energy consumption of the whole production process occurs. This can be explained by the previous consideration concerning the temperature drop: in fact, with high tool speeds, the temperature fall is minimum and so the force required for deforming the ring is lower. Moreover, considering the results reported in Fig. 29, it can be noted that, for a shorter process time (higher main roll rotational speed), the deviation between FEM and analytical model results is smaller. Finally, it has to be mentioned that the analytical model estimation returns the required results in real-time, while the FEM simulations have required an average of 18 hours: this allows to consider the relatively small deviation of the analytical model acceptable, considering the huge computation time saved.

Concerning investigation B, as already explained in 4.3.3, the 9 selected cases have been studied for understanding the accuracy of the application of the analytical model with different materials and considering

the different percentages of flange reduction. The deviation between analytical and FEM results have been compared and calculated at 20%, 40%, 60%, 80%, and 100% of the mandrel time, as reported in Table 20.

Table 20 - Analytical vs FEM deviations for investigation B for Inconel 718 and 42CrMo4.

		Analytical vs FEM solutions deviations [%]									
		Percentage of the total process time [%]									
Geometrical parameters		Inconel 718					42CrMo4				
		20%	40%	60%	80%	100%	20%	40%	60%	80%	100%
Ring #1B	Inner wall Diam. [mm]	2.73	1.19	3.45	2.95	1.26	2.17	0.77	2.91	0.79	0.08
	Outer wall Diam. [mm]	1.85	0.61	2.74	2.00	1.70	2.03	0.82	0.25	0.34	1.36
	Flange Diam. [mm]	1.67	1.04	3.96	3.87	1.06	2.47	2.53	1.76	3.71	0.96
Ring #2B	Inner wall Diam. [mm]	2.17	1.28	2.29	1.29	1.02	0.25	3.06	0.57	1.42	2.71
	Outer wall Diam. [mm]	0.78	1.16	3.54	2.83	0.56	1.49	0.86	2.55	3.44	4.31
	Flange Diam. [mm]	0.61	2.02	2.50	0.93	3.26	1.33	0.54	2.04	1.32	0.21
Ring #3B	Inner wall Diam. [mm]	2.63	1.15	3.27	2.26	1.71	1.67	0.91	2.69	1.70	1.38
	Outer wall Diam. [mm]	0.24	1.28	1.63	2.31	3.46	1.14	1.24	4.03	1.74	0.89
	Flange Diam. [mm]	0.95	1.67	1.94	1.60	4.34	2.06	0.66	0.82	0.96	4.29
Ring #4B	Inner wall Diam. [mm]	2.82	2.32	1.68	0.93	0.51	2.97	1.84	0.64	1.13	1.63
	Outer wall Diam. [mm]	1.72	0.83	1.51	1.26	2.04	0.05	0.17	0.62	1.14	0.63
	Flange Diam. [mm]	2.03	4.06	3.08	2.59	0.37	2.57	2.11	3.05	3.39	0.28
Ring #5B	Inner wall Diam. [mm]	1.50	2.06	1.06	0.45	2.34	1.05	2.07	0.10	0.28	1.62
	Outer wall Diam. [mm]	0.13	0.13	0.82	1.16	0.65	0.80	1.59	0.60	1.40	0.65
	Flange Diam. [mm]	1.80	2.19	2.11	2.20	3.70	1.07	2.65	3.05	2.74	3.69
Ring #6B	Inner wall Diam. [mm]	0.07	1.54	4.39	6.05	3.23	1.02	0.86	3.01	5.41	3.45
	Outer wall Diam. [mm]	0.49	0.10	2.75	4.28	0.97	0.09	0.39	0.17	1.91	2.20
	Flange Diam. [mm]	1.54	0.68	0.28	1.09	5.34	1.08	1.26	0.16	1.18	4.73
Ring #7B	Inner wall Diam. [mm]	1.93	3.19	4.98	3.09	3.05	1.90	3.52	5.42	3.33	3.42
	Outer wall Diam. [mm]	0.57	1.69	3.00	0.91	0.19	1.95	2.35	2.29	0.40	0.74
	Flange Diam. [mm]	1.73	4.63	5.40	4.15	4.66	2.40	3.34	4.81	4.28	4.00
Ring #8B	Inner wall Diam. [mm]	3.73	4.06	2.77	0.28	3.85	0.98	1.62	0.98	1.94	1.03
	Outer wall Diam. [mm]	0.01	2.62	4.60	3.54	3.99	1.63	0.12	0.33	0.61	0.70
	Flange Diam. [mm]	0.23	3.31	3.15	4.01	2.61	0.85	0.82	0.68	1.20	3.04
Ring #9B	Inner wall Diam. [mm]	2.89	3.33	1.14	0.75	1.71	2.40	3.93	0.09	0.00	0.12
	Outer wall Diam. [mm]	2.86	1.70	0.54	1.24	0.54	0.73	1.85	0.54	0.97	0.92
	Flange Diam. [mm]	3.19	4.49	3.09	2.02	1.07	2.64	4.91	2.84	2.64	1.40

As shown in Table 20, the maximum and average deviations between analytical and FEM solutions are calculated in 6.05% and 1.94%, respectively, showing the accuracy in the estimation of the ring geometry also for the case of the same initial ring blank shape deformed to different final rings dimensions.

In order to understand the influence of the material on the geometrical expansion, in Fig. 30 is reported the analytical prediction and the FEM solutions for Ring #9B, derived considering Inconel 718 and 42CrMo4 materials. As can be noted, the geometrical expansion of the ring is independent of the chosen material, confirmation of the fact that the proposed analytical model can be used also to different materials and process conditions different from those utilized in this analysis.

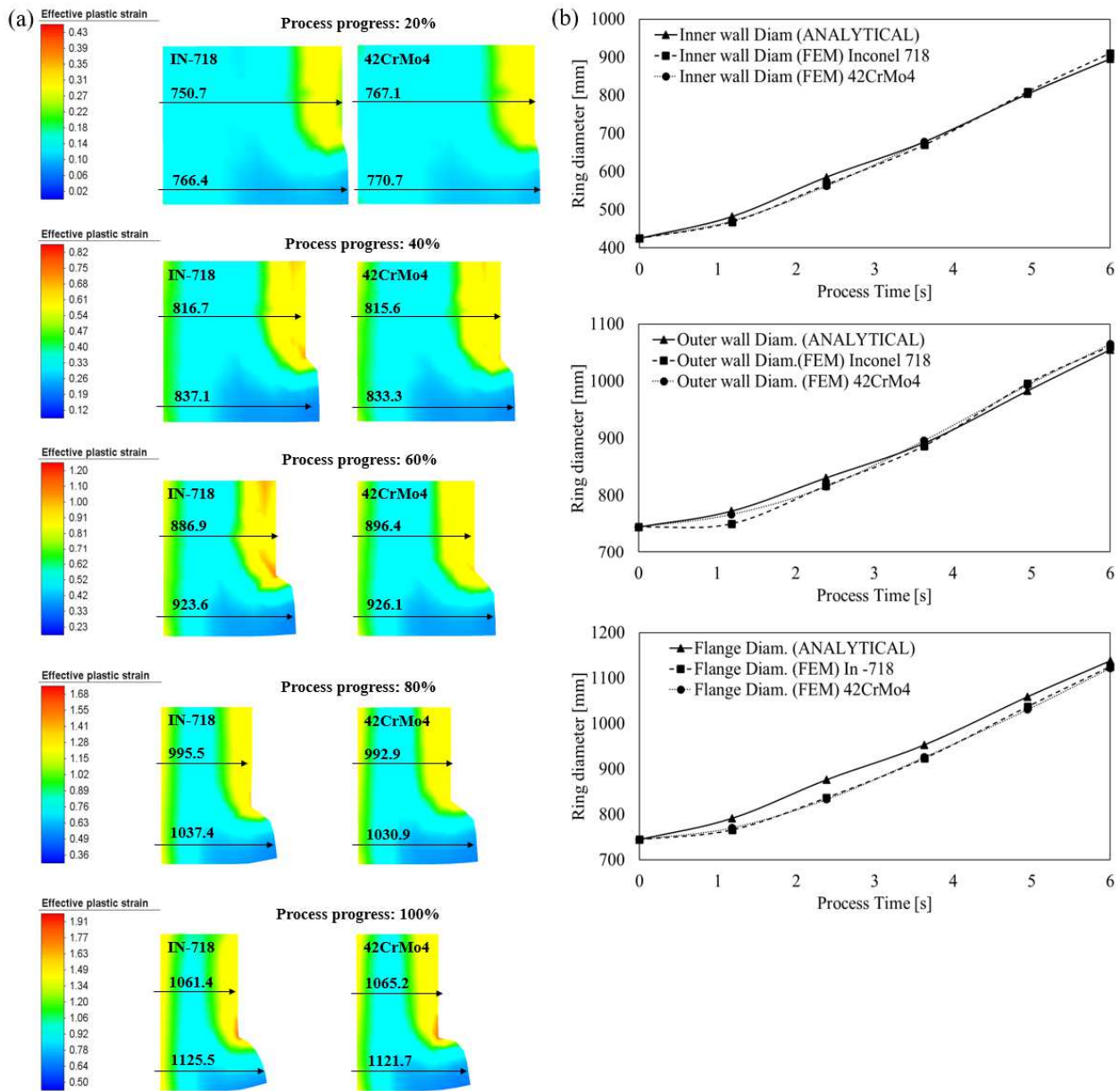


Figure 30 – (a) Comparison between analytical and FEM solutions for Ring #9B considering Inconel 718 and 42CrMo4 materials (in the FEM). (b) Equivalent plastic strain and geometrical expansion comparison between Inconel 718 and 42CrMo4 materials for the Ring #9B.

## 4.5 Process energy prediction for the profiled ring rolling process

The best performing model for energy consumption prediction, identified in the investigations relevant for the flat ring rolling and described in 3.7, has been used for describing and predicting the energy consumption in terms of force integral over time (FIOT) also in the profiled rings case. The Gradient Boosting algorithm, once again, has been developed in a Windows OS environment utilizing the scikit-learn 0.22.2 and Keras 2.3.1 modules implemented in Anaconda Spyder environment with Python 3.7.4.

A total of 50 simulations have been set and run with Simufact Forming 16. The setting of the FEM model has been described in the previous paragraphs 4.3.1. The flanged ring prediction algorithm has been used for choosing the geometry range to consider for the analysis. In Table 21 the geometry parameters, speed variables, material properties and chose ranges are reported.

Table 21 – Ranges of variables in the dataset.

<b>Parameters</b>	<b>Range of validity</b>
Final outer diameter wall [mm]	501 ÷ 1010
Final height wall [mm]	95
Final outer diameter flange [mm]	519 ÷ 1106
Final thickness wall [mm]	45 ÷ 112
Final height flange [mm]	50
Final inner diameter [mm]	375 ÷ 850
Initial outer diameter [mm]	415 ÷ 745
Initial inner diameter [mm]	235 ÷ 425
Initial height [mm]	145
Initial thickness	90 ÷ 160
Main roll speed [rad/s]	2 / 3 / 4
Materials	In-718 / 42CrMo4

The resulting data set has been divided and 80% was used for the training of the model while 20% for the validation. The parameters that compose the input data set of the model are:

1. main roll rotational speed,
2. average mandrel feeding speed,
3. parameters that describes the variation in the shape of the ring,
4. material yield strength,
5. material Young's modulus,
6. force integral over the mandrel time (FIOT).

As concerns the optimization of the prediction model described in 3.7, the random search method has been used for obtaining the parameters of the model and the results are reported in Table 22.

Table 22 - Hyperparameters result of random search optimization in Gradient Boosting.

Model Parameters	OPTIMAZED VALUES
N_ESTIMATORS (M)	672
LEARNING RATE ( $\eta$ )	0.0726
MAX DEPTH	2
MIN SAMPLES LEAF	2
MIN SAMPLES SPLIT	4

Comparing the FEM results of force integral over time with the FIOT obtained by the Gradient Boosting model (Fig. 31) the maximum error is 9.86 % while the average is 5.51%. The determination factor (R-square), also called the “goodness of fit” factor, is equal to 0.9815 and it expresses the variability in the process parameters explained by FIOT. The high value of the R-square shows that the considered sets of parameters all have a high influence on the FIOT value. As mentioned for the case of the flat ring rolling process, the indication of those governing parameters that have the highest influence on the considered target function is of key importance in order to achieve accurate prediction. At the same time, it allows avoiding considering low-influence parameters in the analysis, which would inevitably increase the time required for the definition of the training and validation data sets. Keeping that in mind, the Gradient Boosting algorithm provides the weights during the training phase, but if the database used as input is poor, the weights may only fit the training dataset. Since the development of an extended database requires a huge computational time, the model has been validated only in the range considered as input.

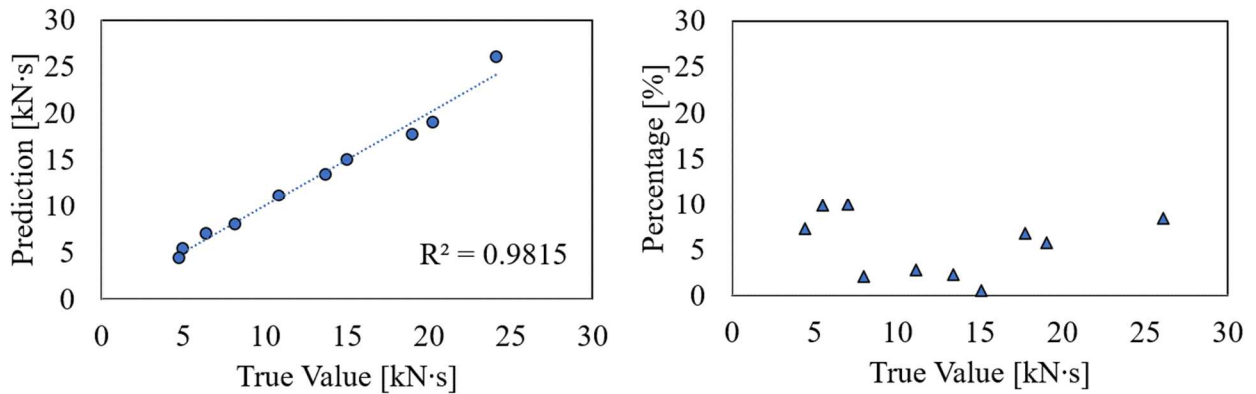


Figure 31 – (a) True value vs prediction and (b) percentage.

For the validation, an arbitrary ring geometry has been considered and its geometric characteristic, material properties, and working speeds are summarized in Table 23. The FIOT calculated by the machine learning model is 8748 [kN·s], while the result of the FEM simulation is 8551.69 [kN·s]. The maximum error is 2%.

Table 23 – Ring dimensions, material properties, and speeds of validation case.

<b>Parameters</b>	<b>Value</b>
Final outer diameter wall [mm]	850
Final wall height [mm]	95
Final outer flange diameter [mm]	950
Final flange height [mm]	50
Final inner diameter [mm]	700
Initial outer diameter [mm]	701.5
Initial inner diameter [mm]	444.56
Initial height [mm]	145
Main roll speed [rad/s]	3.75
Mandrel feeding speed [mm/s]	13.58
Young's modulus [GPa]	111
Yield strength [MPa]	187

## 4.6 Chapter 4 summary and highlights

Concerning the analytical model, the FE implementation, and the energy prediction model presented in the previous sub-sections about profiled ring rolling process, a summary of the key points of this chapter, along with the main achievements, is reported.

- Although the differences in the plastic flow of the material in the cross-section and in the circumferential direction, the energy prediction model developed for the flat ring rolling process showed a good accuracy also for the case of the profiled ring rolling. This fact is of key importance because it shows that the implemented solution can be extended also to different manufacturing processes if a proper pre-analysis is carried out to identify the governing influence the considered output the most (target function);
- The absence of an analytical model for describing the geometrical expansion of the profiled rings has driven the current research to study and develop the first analytical model for predicting the ring evolution of external L-shape section ring starting from both flat or profiled blank geometry. The model can also be adapted to different ring sections, such as internal L-shape and external C-shape, and also to a generic initial ring preform shape. The proposed algorithm can be used in the pre-production phase to analyze the various process parameters and conditions to obtain the desired final shape, allowing to spare precious time during the design stage and to focus on FEM simulations only on few pre-screened cases;
- Moreover, the proposed algorithm can be utilized in the early design stages of the process in order to investigate the influence of geometry, process conditions, and parameters on the geometrical expansion of the ring, helping process engineers in reducing the number of FEM simulations required for an efficient design of the profiled ring rolling process;

- Besides, a FEM model has been built specifically for profiled RARR process, considering internal and external L-shape as well as external C-shape. Several numerical simulations have been conducted in order to build a dataset of process parameters values. The process settings, utilized for the implementation of the FEM simulations, have been determined by the implemented algorithm, extended from the previously developed solution for flat rings by Berti and Quagliato [16];
- Both analytical and numerical models for profiled ring rolling process have been validated through comparison with previous literature data and experiments. The validation has been conducted considering different initial and final ring cross-sections. Concerning the geometry estimation, the analytical model and FEM model have a maximum error respectively of 4.9% and 3.2%. Regarding the force estimation, the numerical model returns a maximum deviation of 14.8% with the first literature comparison and 3.3% with the second literature comparison;
- Two cross-validations between analytical and FEM models' solutions have been conducted. The first one investigated the influence of different tool speeds on the accuracy of the analytical model against the numerical model. The maximum resulting error is 11.6%: the analytical model works well in a wide range of tool speeds, and it has been noticed that the accuracy decreases when the tools' speed decreases or, equivalently, when the process time increase. Moreover, it has been found that the energy consumption of the whole process decreases when the tool speeds (main roll rotational speed and mandrel feeding speed) are higher under the other process parameters. The second investigation has analyzed the influence of different materials and ring flange reduction on the accuracy of the analytical model, obtaining a maximum error of 6.05%.
- A total of 50 FEM simulation of external L-shape profiled ring rolling process has been conducted in order to develop a database to build an energy prediction model for the profiled ring. The same Gradient Boosting algorithm and the same developing methodology (training and validation) of flat RARR analysis has been used and adapted for the flanged ring rolling process. Checking the error on force impulse estimation of the predictive model against the 50 FE simulations, a maximum error of 9.86% has been obtained. Moreover, the new machine-learning algorithm has been validated through comparison with a new FEM simulation, obtaining a maximum error of 2%.



## **Chapter 5**

# **Energy minimization model development and validation**

To conclude this research, the developed energy minimization model is presented here. The model has been applied and validated on the flat ring rolling process, and it has also been implemented for the deep drawing process and validated as well. The developed optimization model not only has a scientific interest but also industrial importance, given the ever-growing attention to process optimization and energy saving. Due to the complex nature of this production process and the non-linear relationship between the numerous process variables, a different approach from the classic direct optimization models has to be applied. To this aim, the Differential Evolution (DE) model has been considered, given its properties of finding the optimized solution on a “black box” environment and without the need for function derivatives [89, 90]. The algorithm has been developed with Python script programming language and it is designed to work with multi-dimensional real-valued candidate solutions. The DE-based developed model has been built in order to be easy to use for possible industrial applications and to give the optimized response in real-time, permitting to save time compared to numerical analysis. Moreover, since the DE model requires more input data than a classic gradient descent optimization method, a wider database of process case studies has been provided, using the developed energy prediction model to increase the number of combinations contained in the data set.

In the following section 5.1, the algorithm theory will be explained, along with the advantages of the chosen approach. Then, in section 5.2, all the passages and considerations used to build the algorithm will be reported. Finally, in chapter 5.3, the obtained results and the validation of the model will be shown for both flat ring rolling and deep drawing processes, along with final considerations. Chapter 5.4 contains a summary of the key points of this last part of the research.

## 5.1 Definition of energy minimization model

In chapter 3, the non-linear regression approaches have been used in order to develop a predictive model for energy consumption, and they were found to be much more accurate than linear regression approaches for this specific process. This might mean that a non-linear correlation exists between the chosen process parameters and the energy consumption described as force impulse over time. For this reason, it has been decided to proceed with an optimization approach that doesn't require a defined analytical form or a minimization of the function derivatives. The Differential Evolution model has been chosen to develop the energy optimization algorithm: it belongs to the evolutionary computing algorithm field, which in turn is a sub-field of the artificial intelligence techniques.

Evolutionary computing is a series of algorithms designed for global optimization models, that emulate biological processes of evolution [91], with a population of solutions that are selected through several iterations until the best individual solution is found. This kind of model started to be implemented in the last century, with the rapidly growing computation power, and the application to industrial cases are several. Among the various evolutionary computing approaches, the Differential Evolution (DE) model has been chosen and implemented in this research. The advantage of this model over other approaches is that it allows for optimization of non-linear and non-differentiable objective functions requiring fewer control parameters. Moreover, Differential Evolution is a heuristic and stochastic model that is easy to use and implement, making it a valid solution for engineering and industrial applications.

As with other evolutionary computing approaches, Differential Evolution starts with creating randomly an initial population of candidate solutions of the optimization problem, also called individuals, as shown in Eq. (38).

$$X_{N,p} = [x_{1,N}, x_{2,N}, \dots, x_{m,N}] \quad (38)$$

where  $X_{N,p}$  is the population,  $N$  is the dimension of the problem,  $p$  is the number of populations,  $x_{m,N}$  is the  $m$ -th individual and  $m$  is the population size. Many strategies can be applied to mutate the population and generate new individuals. In this research, a classic mutation strategy has been introduced in the population considering for each solution  $x_{m,N}$  a mutant vector  $v_{i,N}$  as reported in Eq. (39):

$$v_{i,N} = x_{best,1,N} + F \cdot (x_{random2,N} - x_{random3,N}) \quad (39)$$

where  $x_{best,1,N}$  is the target vector, defined as the best individual that optimizes the problem.  $F$  is the mutation factor defined by the user, and  $x_{random2,N}$  and  $x_{random3,N}$  are random individuals of the population  $X_N$ . Obviously,  $x_{best,1,N}$ ,  $x_{random2,N}$  and  $x_{random3,N}$  must be different individuals and the obtained mutant vector must be within the problem value ranges to be considered valid. After completing the mutation process, a crossover step is applied, mixing the mutant vector components  $v_{i,j}$  with the target vector components  $x_{best1,j}$ , and generating a trial vector  $u_{i,N}$  with a binomial approach as defined in Eq. (40):

$$u_{ji} = \begin{cases} v_{ji}, & \text{if } r_{random} \leq CR \text{ or } j = i_{random} \\ x_{ji}, & \text{if } r_{random} > CR \text{ or } j \neq i_{random} \end{cases} \quad (40)$$

where  $j$  is the  $j$ -th vector components ( $j \in [0, N]$ ),  $CR$  is the crossover rate defined by the user,  $i_{random}$  is a random integer number chosen from the interval  $[1; N]$  and  $r_{random}$  is a number randomly chosen from interval  $[0; 1]$ .

After conducting the crossover of the individual components, a final selection phase is initialized, for determining if the target vector or the trial vector will be included in the next population  $p+1$ . The following Eq. (41) summarizes the selection step procedure.

$$x_{i,N,p+1} = \begin{cases} u_{i,N} & \text{iff } (u_{i,N}) \leq f(x_{i,N}) \\ x_{i,N} & \text{otherwise} \end{cases} \quad (41)$$

Where  $f(x)$  is the objective function that must be optimized, and that in this research coincides with the developed GB energy predictive model. It is clear that, after this final selection phase, the new population will have the best fitting individuals. The process described above is then repeated iteratively until the maximum number of iterations is reached, or in other words, the maximum number of populations has been generated. Hereafter in Fig. 32 it is resumed the iterative process of the developed model.

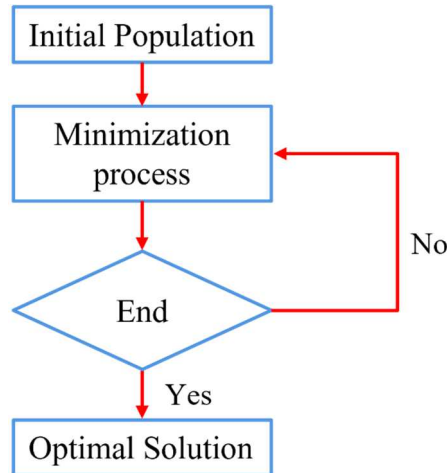


Figure 32 – Flowchart of the main step of the DE iterative process.

In the following section, it will be reported the implementation of the DE evolution, outlining the process parameters considered and the algorithm constants adopted.

## 5.2 Differential Evolution implemented method

The differential evolution algorithm above described has been developed in a Windows OS environment utilizing the Scikit-learn 0.24.1 and Scipy 1.6.2 modules implemented with Python 3.8.8. Concerning the specific application of this research on the flat ring rolling process, the input parameters are the final ring geometry, defined as inner and outer diameter and ring height, the ring material and temperature, and the geometry of the tools.

On the other hand, the expected output parameters that minimize the energy consumption are the initial ring geometry, which means inner and outer diameter and ring height, the main roll rotational speed, and the mandrel feeding speed. In the following Fig. 33, the process parameters involved in the DE minimization model are resumed.

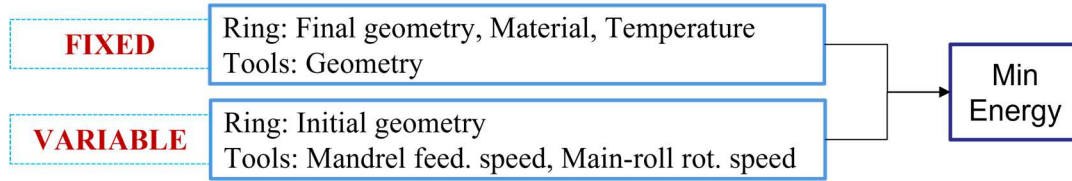


Figure 33 – Input and Output parameters for DE energy minimization model.

Moreover, the objective function used in the DE algorithm is the Gradient Boosting energy predictive model developed and validated in chapter 3. Finally, since this evolutionary computing model required a high number of values to be implemented, with the aid of the GB model 320 new case studies have been added to the already developed database, reaching a total of 760 cases.

The DE method requires the user to first define three algorithm parameters, namely the population size  $m$ , the mutation factor  $F$ , and the crossover parameter  $CR$ . These three variables have been set equal to 15, 0.5, and 0.7 respectively, along with the maximum number of iterations equal to 1000. These are initial settings, which will be changed and/or optimized during the training process.

Specifically, the first population has been generated by the Latin Hypercubic statistical method, which allows to randomly generate the individuals inside an optimized population number that maximizes the parameter space. Furthermore, the mutation strategy used in this research is called “best/1/bin” meaning the best-fitting individual is considered as the target vector during the mutation phase, that only 1 vector is perturbed at each iteration and that a binomial crossover is applied after the mutation.

As it will be explained in the following section 5.3, a validation of the developed minimization algorithm has been conducted and reported along with final consideration on the model.

### 5.3 Differential evolution model validation

In order to demonstrate the robustness and the effective calculation of the minimum energy consumption with the Differential Evolution algorithm, a random ring case study (Ring#1) has been considered and analyzed. The input and output process parameters of the minimization model concerning this specific Ring#1 production are summarized in Table 24.

Table 24 – Input and output parameters used in DE algorithm for Ring#1.

Case Study	Fix Input					Variable Output				
	$D_F$ [mm]	$d_F$ [mm]	$h_F$ [mm]	$T$ [°C]	Material	$D_0$ [mm]	$d_0$ [mm]	$h_0$ [mm]	$\omega_M$ [rad/s]	$v_{mM}$ [mm/s]
Ring#1	750	570	90	1050	42CrMo4	546.52	325	110.76	4.95	5.64

Afterward, for validating and checking the reliability of the DE algorithm, a FEM simulation has been conducted with the same process conditions applied to the numerical model developed in section 3.3. The energy consumption resulted from the Differential Evolution is equal to 1184.91 [N·s], while, with the FEM simulation, a value of 1187.58 [N·s] has been obtained. Comparing the two results, and considering the FE simulation as a reference, the error of the DE minimization model is equal to 8.95%. Since in the Differential Evolution algorithm, the value of the energy is calculated by the Gradient Boosting model, the obtained error matches with the predictive error underlined in section 3.7 (9.03%).

Further validation of the DE minimization model has then been conducted analyzing the boundary of the solution, checking if the output is the real minimum of the FIOT function for that specific case study. In order to do that, a first subdivision of the process parameters has been done, creating the geometrical parameter group GP and the control parameter group CP. The first group includes the output geometrical variables, namely the final outer and inner diameter and the final height.

On the other hand, the average mandrel feeding speed and main roll rotational speed belong to the second group. Then 5 additional ring case studies have been set varying and combining the GP and CP group by plus and minus 15% of their values. The following Table 25 resumes the process parameters considered for all 5 additional cases. Some of the combinations have not been considered since the initial geometries turned out to be too close to the final geometry.

Table 25 – Initial geometrical values and tools speeds of the case studies.

Case Study	Do [mm]	d0 [mm]	h0 [mm]	$\omega_M$ [rad/s]	$v_{mM}$ [mm/s]	GP	CP
Ring#1	546.52	325	110.76	4.95	5.64	1	1
Ring#2	508.62	275	116.8	4.95	5.64	-15%	1
Ring#3	546.52	325	110.76	4.21	4.8	1	-15%
Ring#4	508.62	275	116.8	4.21	4.8	-15%	-15%
Ring#5	546.52	325	110.76	5.7	6.49	1	15%
Ring#6	508.62	275	116.8	5.7	6.49	-15%	15%

Then, as conducted for Ring#1, each new case study has been processed through the same FEM model, to obtain the energy consumption. In the following Fig. 34 the results are plotted, with the different ring settings on the x-axis and the energy consumption (defined as FIOT) obtained by numerical simulation in the y-axis. As it can be seen, the process energy of Ring#1 case turns out to be the minimum, therefore the minimization model has been considered valid.

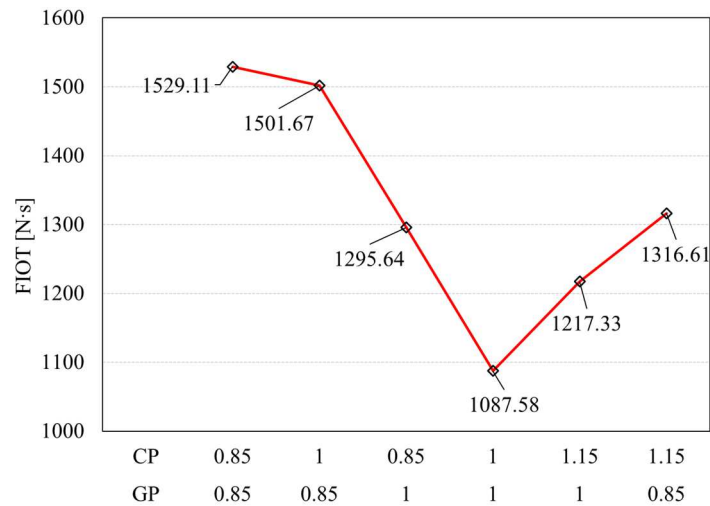


Figure 34 – Verification of the prediction of the “real minimum” for the FIOT parameter.

The same approach used in this research to develop a minimization model for the flat ring rolling process has been used for a different production system, namely the deep drawing production process.

This sheet metal forging process starts from a blank metal sheet that is deformed in a forming die by the pushing force generated by the translation of a punch, as summarized in Fig. 35. The process is defined as “deep” drawing since the height of the final part is greater than its diameter.

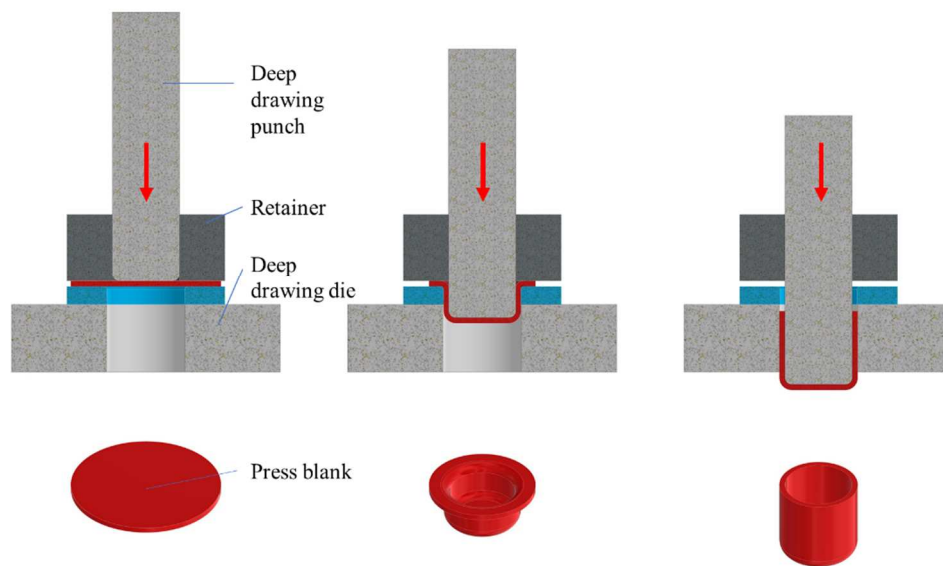


Figure 35 – Schematic representation of the main phases of the deep drawing process.

Different shapes and heights can be obtained by changing the forming die and punch geometries, and the industrial application of this process are several, such as automotive and medical components, packaging, and electronic cases and accessories. Moreover, different metal alloys can be used such as aluminum alloy and stainless steel. In order to keep the sheet in the right position during the plastic deformation process, a blank holder is usually applied before the translation of the punch, and the force of this latter generates a radial stress on the locked flanged part of the final pieces. The initial shape of the sheet (blank), the punch velocity, the

friction between the metal sheet and forming die, and the blank-holder force are all influencing parameters on the final quality of the component, as well as on the possible forging defects, such as the earing defect.

Considering this brief introduction of the deep drawing process, this last research part focused on extending and validating the developed optimization model to the deep drawing process and has been conducted in collaboration with Sogang University. In this specific case, the aim is to minimize the defects occurrences, optimizing both process and the geometrical parameters to either minimize or eliminate the earing at the edges of the formed part. This defect is caused by a combination of material anisotropy and non-uniform stress distribution in the corner or edges of formed parts and, if not controlled during the production, it leads to an expensive post-operation reworking of the part.

The Differential Evolution algorithm, presented in the previous section of the thesis, has been trained by means of a dataset specifically designed for the deep drawing process but, since the target of this section is the validation of the algorithm, the details relevant for the database construction are not included. For the case of the deep drawing process, the target is defined as the minimization or elimination of the post-forming earing defect arising in the area close to the edges of the part and, especially, where corner radii are present. The considered process conditions, as well as the calculation procedure for the earing defect, are shown in Fig. 36.

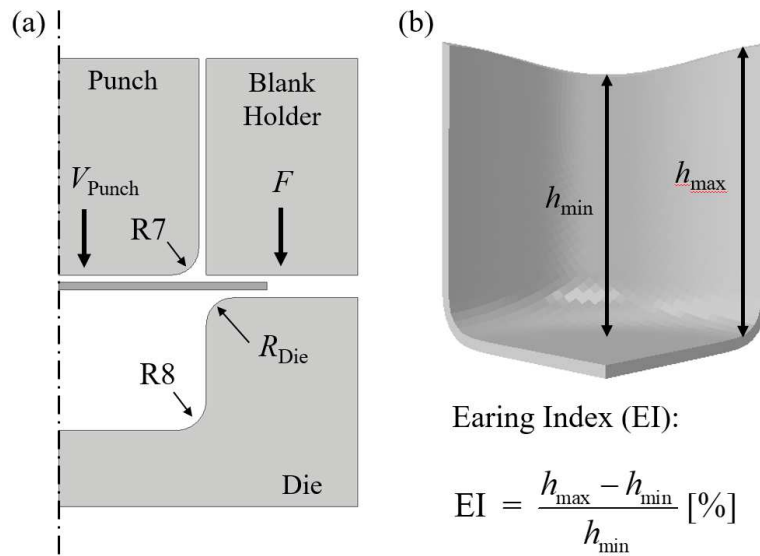


Figure 36 – (a) Schematic representation of the implemented deep drawing process showing the characteristic dimensions of the dies and (b) Earing Index definition.

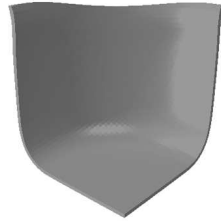
The considered final shape is summarized in Fig. 37a whereas the fixed input values and the predicted process and geometrical parameters, predicted by the Differential Evolution model, are reported in Table 26. As for the flat ring rolling case, in order to verify that the predicted solution is, in fact, the minimum point of the target function (local minimum), additional study cases have been considered by changing the blank shear outer diameter in a  $\pm 15\%$  range, as shown in Table 27. For the assessment of the results, both EI index (Fig. 36) as well as the geometrical accuracy of the part, especially in terms of final height, have been considered.

Table 26 - Input and output parameters used in DE algorithm for the deep drawing validation case.

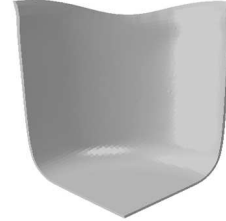
Case Study	Fix Input			Variable Output				
	Final cup $\phi$ [mm]	Height [mm]	Strength coef. [MPa]	Initial blank diam. [mm]	Die radius [mm]	Force [N]	Velocity [mm/s]	Friction
Case#1	140	36~37	1200	119.35	6.155	11511.7	119.6	0.0737



(a) Final cup geometry with minimum target height



(b) Formed cup geometry with optimized variables



(c) Formed cup geometry with not optimized variables

Figure 37 – (a) Final cup-shape considered in the validation case. Result of the deep drawing considering (b) the predicted (optimization) process conditions and (c) non-optimized process conditions.

Table 27 – Study cases implemented to verify the “real minimum” predicted by the DE algorithm.

Case Study	Initial blank diam. [mm]	Die radius [mm]	Force [N]	Velocity [mm/s]	Friction	Height [mm]	Earing [%]	Defect
Case#1	119.35	6.155	11511.7	119.6	0.0737	36.4	7.944	0
Case#2	119.35	6.155	9785	101.7	0.0737	36.7	7.945	0
Case#3	119.35	6.155	13238	137.6	0.0737	36.2	7.932	0
Case#4	101.45	6.155	11511	101.7	0.0737	23.1	4.664	0
Case#5	101.45	6.155	9785	137.6	0.0737	23.3	4.663	0
Case#6	101.45	6.155	13238	119.6	0.0737	22.8	4.682	0
Case#7	137.26	6.155	11511	137.6	0.0737	-	-	1
Case#8	137.26	6.155	9785	119.6	0.0737	-	-	1
Case#9	137.26	6.155	13238	101.7	0.0737	-	-	1

First of all, considering the optimized process and geometrical settings, as reported in Table 26, the cup shape reported in Fig. 37b shows a minimum earring defect in comparison to an example of a non-optimized process and geometrical parameters configuration (Fig. 37c). Moreover, by considering the results of the additional 8 study cases reported in Table 7, it is clear that cases #1, #2, and #3, being close to each other in



terms of geometrical and process settings, allows to match the cup height and to limit the earring defect, estimated in 7.93% for all the three above-mentioned cases.

As concerns the cases from #4~#6, although the earring defect is less than that of the #1~#3 cases, the target height of the cup could not be reached. On the other hand, for the #7~#9 cases, the stress distribution at the edges of the blank holder leads to a too high deformation, which would lead to sheet metal fracture in the real production. For these reasons, #4~#6 cases have been identified as “0” in the “defect” columns, since the part can be produced without fracture, although the final geometry cannot be reached. On the other hand, for #7~#9 cases, the height and magnitude of the earring defect become negligible in comparison to the fracture arising on the metal sheet, thus the defect column has been indicated as “1”.

From a global perspective, the geometry and process predictions carried out by the implemented DE algorithm show that, for the case of the deep drawing process, the minimization of the target function, namely the reduction of the earring defect and the matching of the final height, is not represented by a single point but, instead, by a minimum locus. This fact implies that there are more than one possible set of parameters combinations that allow minimizing the considered target function, but they are all close to each other. From an analytical point of view, this fact can be interpreted as the slope at which the target function output changes according to the inputted parameters. For the case of the flat ring rolling process, the FIOT parameter, and the relevant target function, were highly influenced by the considered input parameters. On the other hand, for the case of the deep drawing process, the target function changes with a lower rate, generating solutions close to each other (such as #1~#3 cases) to provide similar results.

This ambiguity of the solution can be removed by reshaping the target function in order to consider additional parameters, such as the forming force, but, at this stage, this procedure is still being tested and could not be added in the current version of the thesis.

## 5.4 Chapter 5 summary and highlights

Considering the energy minimization model proposed in this chapter, and the results of the two validations carried out on the flat ring rolling and the deep drawing process, the important remarks relevant for this chapter are listed here after:

- Due to the complex nature of the flat ring rolling process and the non-linear objective function that predicts the energy consumption, a non-gradient based optimization approach is required in order to develop an energy minimization model;
- The Differential Evolution algorithm has been chosen, among the artificial intelligence optimization approaches, to build the desired minimization model;
- The database of flat ring values has been extended by means of the developed energy prediction model, based on the Gradient Boosting algorithm, presented in section 3.6;
- The combination of the energy prediction and the energy minimization algorithms reduces the time required for the training dataset definition in the energy minimization process. At the same time, it

should be noted that the energy prediction accuracy strongly influences the results of the energy minimization, thus much effort should be put in a proper training phase of the former in order to achieve a good accuracy for the latter;

- By means of the validation analysis carried out on boundary solution points surrounding the predicted solution it has been possible to verify that the predicted settings allow obtaining the minimum of the FIOT value, considered as the target function for the optimization;
- The same methodology applied to the flat ring rolling process for the minimization of the FIOT parameter has also been applied to the deep drawing process for the determination of the process and design parameters that allow minimizing the earing on the final product. This additional validation phase showed that the proposed algorithm performs well even for the case of different target functions and different manufacturing processes. This strengthens the generality of the proposed solution and, as highlighted in the following section, it serves as a starting point for future development.

## Chapter 6

### Conclusions and on-going work

Having summarized each chapter separately at their respective ends, the aim of this last section of the thesis is to provide a more general interpretation of the implemented algorithm from the point of view of their possible application into industrial environments, as well as to provide additional details on the on-going research work, which could not be included in this thesis.

Considering the various energy prediction and minimization models developed considering the flat ring rolling process it is interesting to highlight that, although counter-intuitive, the most important part is not the training of the former but, instead, of the latter one. This fact is particularly true when we consider that the energy prediction model, if well-trained, can be utilized for the expansion of the training database for the energy minimization algorithm. For this reason, the design of the initial database becomes an essential part of the algorithm development procedure and should be thoroughly investigated in order to provide both depth as well width of the dataset. The depth of the database is intended as a thorough analysis of the cross-influence between the various parameters involved in the considered process and their influence on the target function. For a generic manufacturing process, dozens of input parameters can be identified but if they are coupled with a specific target function, only a few of them will actually have a real and tangible influence. On the other hand, the width is intended in terms of the ranges of the considered parameters. This aspect is important if the database is aimed to be extended by means of prediction algorithms, as carried out in this research for the case of the flat ring rolling process. Although additional data can be predicted in the original database range, if some predictions are attempted outside this range, the accuracy may fall dramatically, inevitably affecting the energy minimization prediction.

Considering these two key points, for the case of the profiled ring rolling process, the developed analytical model for the estimation of the ring geometrical expansion as a consequence of the process parameters, ring geometry, and boundary conditions allows establishing the above-mentioned correlation required for the initial

design of the training dataset and has been considered as a necessary intermediate step for the extension of the energy prediction model from the flat to the profiled ring rolling process.

For the case of well-established manufacturing processes, such as the deep drawing process, these input-output correlations are available in the literature and can be directly utilized. On the other hand, for relatively newly developed or not-well-investigated processes, the pre-processing phase still remains the key point if either predictions or minimizations need to be carried out.

In fact, the fundamental nature of machine learning algorithms is to establish a correlation between a set of data where various input parameters are linked to one or more outputs. Obviously, the quality of the established correlation depends on the capability of the implemented machine learning model in recognizing the connection between these parameters. At the same time, the meaningfulness of the training dataset, as well as of the relevant validation cases, strongly influences the overall performances and, for this reason, the algorithm should be well designed and implemented.

Considering the research presented in this thesis, the developed target function minimization algorithm firstly developed and implemented for the case of the flat ring rolling process has shown its generality thanks to the validation carried out on the deep drawing process. In fact, the proposed algorithm can be extended also to manufacturing processes different from the metal forming, but the definition and construction of the training and validation datasets should be oriented towards providing data that can help the machine learning identifying the correlation between the parameters of interests, avoiding the consideration of low-influence variables.

Regarding this last statement, the proposed algorithm is now being tested on the plastic injection molding process in order to identify the process parameters that allow predicting and minimizing the warpage at the end of the process with the aim of showing that it can be generalized also to a manufacturing process where material, process, and boundary conditions are completely different from the initially considered flat ring rolling process. In addition to that, in the three considered manufacturing processes, finite element method (FEM) simulations have been utilized for the definition of the training and validation database whereas for the case of the injection molding process finite volume method (FVM) simulations are being utilized. This difference in the tool utilized for the definition of the training and validation datasets shall cast light on possible influences of the simulation approach on the database construction accuracy, thus on both the algorithm prediction and minimization capabilities.

Another important aspect that is being analyzed is the influence of the ratio between real and predicted values in the construction of the hybrid database utilized in the minimization algorithm. After the initial training phase of the prediction algorithm, based on FEM or experimental results, the trained prediction algorithm can be utilized for the augmentation of the initial database. This expanded database can then be inputted into the minimization algorithm, as also carried out for the case of the flat ring rolling process. However, the composition of this second database is crucial in order to minimize the computational time required for the definition of the initial (FEM only) training dataset. For this reason, additional tests are being

carried out in order to investigate the influence of the composition, both in terms of depths and width, of the training database in order to define rules for the minimization of the FEM (or FVM) simulations required for the definition of the initial database. This aspect is crucial especially for the application of the proposed procedures in industrial environments, where time is most likely the most important variable being considered in the evaluation of the performance of process investigation technique, such as the one proposed in this research.



# Appendix 1

The material properties of steel alloy 42CrMo4, super alloy Inconel 718 and aluminum alloy AA6082 after reported in terms of mechanical and thermal properties in Fig. 38 a, b, c, Fig. 39 d, e, f and Fig. 40 g, h, I respectively.

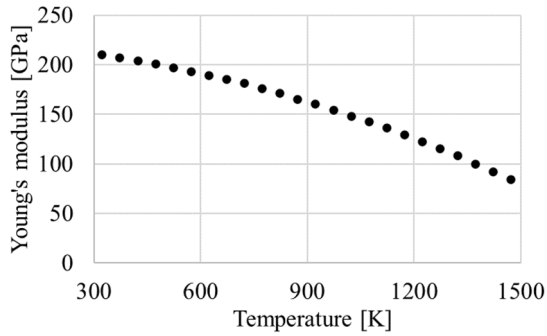


Figure 38a - Young's modulus of 42CrMo4.

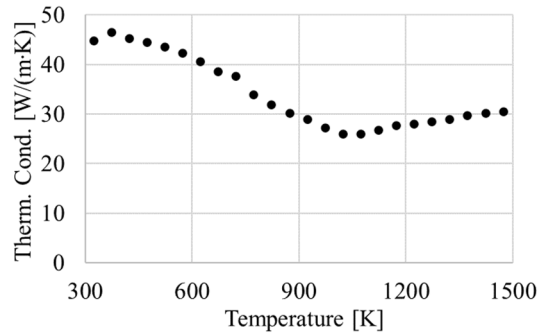


Figure 38b - Thermal conductivity of 42CrMo4.

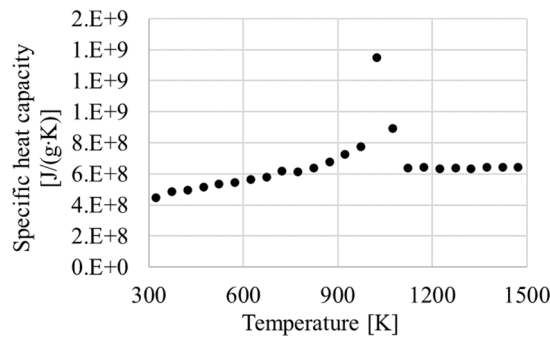


Figure 38c - Specific heat capacity of 42CrMo4.

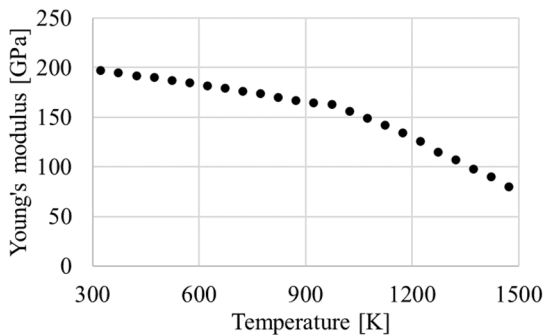


Figure 39a - Young's modulus of In-718.

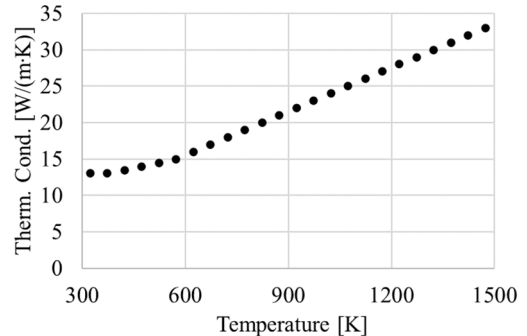


Figure 39b - Thermal conductivity of In-718.

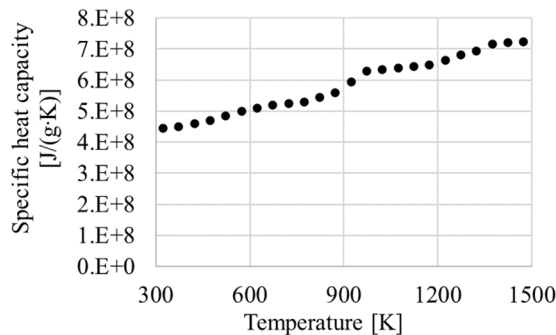


Figure 39c - Specific heat capacity of In-718.

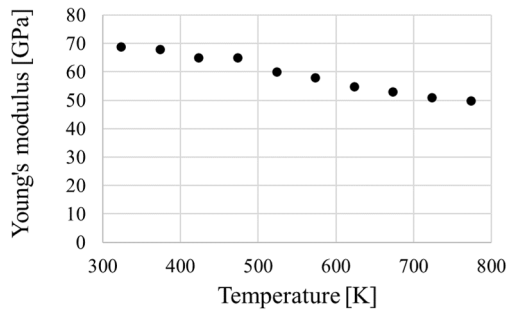


Figure 40a - Young's modulus of AA6082.

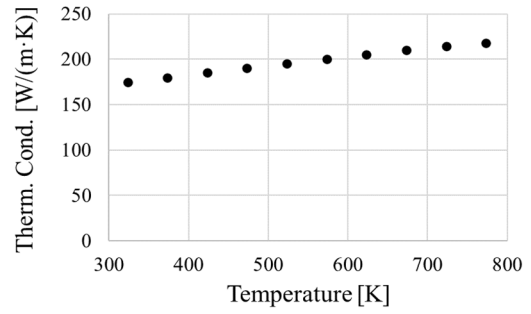


Figure 40b - Thermal conductivity of AA6082.

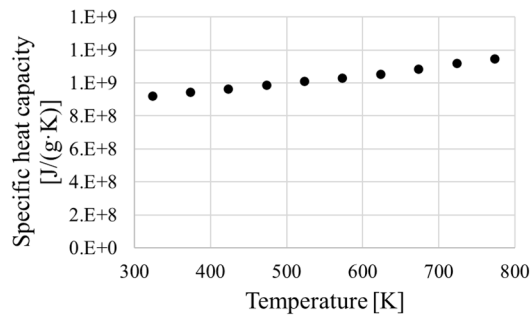


Figure 40c - Specific heat capacity of AA6082.



## Appendix 2

	Initial outer diam.	Final outer diam.	Ring initial temp.	Main roll rotational speed	Average mandrel feeding speed	Yield strength	Young's modulus	Force integral over time
# Num	D <sub>0</sub> [mm]	D <sub>F</sub> [mm]	T [°C]	$\omega_M$ [rad/s]	v <sub>mM</sub> [mm/s]	YS [MPa]	YM [GPa]	FIOT [Ns]
1	490.5	650	1200	2	5.7	40	84	2437
2	490.5	650	1200	3	8.5	40	84	1986
3	490.5	650	1200	5	14.15	40	84	1107
4	490.5	650	1200	2	5.65	40	84	2360
5	490.5	650	1200	3	6	40	84	2104
6	490.5	650	1200	5	13.7	40	84	1019
7	490.5	650	1200	2	5.73	40	84	2423
8	490.5	650	1200	3	7.6	40	84	2015
9	490.5	650	1200	5	14	40	84	1094
10	490.5	650	1050	2	5.7	50	108	3745
11	490.5	650	1050	3	8.5	50	108	2958
12	490.5	650	1050	5	14.15	50	108	1633
13	490.5	650	1050	2	5.65	50	108	3676
14	490.5	650	1050	3	6	50	108	3210
15	490.5	650	1050	5	13.7	50	108	1501
16	490.5	650	1050	2	5.73	50	108	3716
17	490.5	650	1050	3	7.6	50	108	2912
18	490.5	650	1050	5	14	50	108	1670
19	490.5	650	900	2	5.7	126	129	5696
20	490.5	650	900	3	8.5	126	129	4488
21	490.5	650	900	5	14.15	126	129	2476
22	490.5	650	900	2	5.65	126	129	5523
23	490.5	650	900	3	6	126	129	4722
24	490.5	650	900	5	13.7	126	129	2193
25	490.5	650	900	2	5.73	126	129	5696
26	490.5	650	900	3	7.6	126	129	4589
27	490.5	650	900	5	14	126	129	2475
28	510.9	650	1200	3	7.5	40	84	1318
29	510.9	650	1050	3	7.5	50	108	1991
30	510.9	650	900	3	7.5	126	129	3072
31	518.9	800	1200	3	6.85	40	84	3609
32	518.9	800	1200	2	4.88	40	84	4701
33	518.9	800	1200	5	12.12	40	84	2092
34	518.9	800	900	3	6.85	126	129	8261

# Num	D <sub>0</sub> [mm]	D <sub>F</sub> [mm]	T [°C]	ω <sub>M</sub> [rad/s]	v <sub>mM</sub> [mm/s]	YS [MPa]	YM [GPa]	FIOT
35	518.9	800	900	2	4.88	126	129	11700
36	518.9	800	900	5	12.12	126	129	4909
37	518.9	800	1050	3	6.85	50	108	5373
38	518.9	800	1050	2	4.88	50	108	7575
39	518.9	800	1050	5	12.12	50	108	3250
40	549.3	650	1200	2	2.75	40	84	820
41	549.3	650	1200	3	3.75	40	84	724
42	549.3	650	1200	5	7.3	40	84	380
43	549.3	650	1200	3	4.5	40	84	789
44	549.3	650	1200	3	5.25	40	84	585
45	549.3	650	1200	3	5.75	40	84	542
46	549.3	650	1200	3	5.5	40	84	582
47	549.3	650	1050	2	2.75	50	108	1400
48	549.3	650	1050	3	3.75	50	108	1112
49	549.3	650	1050	5	7.3	50	108	678
50	549.3	650	1050	3	4.5	50	108	1294
51	549.3	650	1050	3	5.25	50	108	910
52	490.5	650	1070	2	5.7	161	100	7686
53	490.5	650	1070	3	8.5	161	100	5880
54	490.5	650	1070	5	14.15	161	100	3266
55	490.5	650	1070	2	5.65	161	100	7630
56	490.5	650	1070	3	6	161	100	6889
57	490.5	650	1070	5	13.7	161	100	3050
58	490.5	650	1070	2	5.73	161	100	7693
59	490.5	650	1070	3	7.6	161	100	6623
60	490.5	650	1070	5	14	161	100	3244
61	510.9	650	1070	3	7.5	161	100	4073
62	549.3	650	1070	2	2.75	161	100	3514
63	549.3	650	1070	3	3.75	161	100	2760
64	549.3	650	1070	5	7.3	161	100	1383
65	549.3	650	1070	3	4.5	161	100	3364
66	549.3	650	1070	3	5.25	161	100	1935
67	549.3	650	1070	3	5.75	161	100	2300
68	549.3	650	1070	3	5.5	161	100	1874
69	490.5	650	1025	2	5.7	187	120	8626
70	490.5	650	1025	3	8.5	187	120	6788
71	490.5	650	1025	5	14.15	187	120	3657
72	490.5	650	1025	2	5.65	187	120	8604
73	490.5	650	1025	3	6	187	120	7778
74	490.5	650	1025	5	13.7	187	120	3461
75	490.5	650	1025	2	5.73	187	120	8648
76	490.5	650	1025	3	7.6	187	120	7424
77	490.5	650	1025	5	14	187	120	3662
78	510.9	650	1025	3	7.5	187	120	4595

# Num	D <sub>0</sub> [mm]	D <sub>F</sub> [mm]	T [°C]	ω <sub>M</sub> [rad/s]	v <sub>mM</sub> [mm/s]	YS [MPa]	YM [GPa]	FIOT
79	549.3	650	1025	2	2.75	187	120	3955
80	549.3	650	1025	3	3.75	187	120	3084
81	549.3	650	1025	5	7.3	187	120	1547
82	549.3	650	1025	3	4.5	187	120	3820
83	549.3	650	1025	3	5.25	187	120	2207
84	549.3	650	1025	3	5.75	187	120	2063
85	549.3	650	1025	3	5.5	187	120	2117
86	490.5	650	980	2	5.7	216	126	9763
87	490.5	650	980	3	8.5	216	126	7692
88	490.5	650	980	5	14.15	216	126	4134
89	490.5	650	980	2	5.65	216	126	9698
90	490.5	650	980	3	6	216	126	8729
91	490.5	650	980	5	13.7	216	126	3920
92	490.5	650	980	2	5.73	216	126	9695
93	490.5	650	980	3	7.6	216	126	8205
94	490.5	650	980	5	14	216	126	4132
95	510.9	650	980	3	7.5	216	126	5162
96	549.3	650	980	2	2.75	216	126	4486
97	549.3	650	980	3	3.75	216	126	3522
98	549.3	650	980	5	7.3	216	126	1799
99	549.3	650	980	3	4.5	216	126	4323
100	549.3	650	980	3	5.25	216	126	2496
101	549.3	650	980	3	5.75	216	126	1800
102	549.3	650	980	3	5.5	216	126	2410
103	490.5	650	300	2	5.7	101	58	2028
104	490.5	650	300	3	8.5	101	58	1508
105	490.5	650	300	5	14.15	101	58	811
106	490.5	650	300	2	5.65	101	58	1965
107	490.5	650	300	3	6	101	58	1690
108	490.5	650	300	5	13.7	101	58	774
109	490.5	650	300	2	5.73	101	58	1978
110	490.5	650	300	3	7.6	101	58	1630
111	490.5	650	300	5	14	101	58	816
112	510.9	650	300	3	7.5	101	58	1191
113	549.3	650	300	2	2.75	101	58	1098
114	549.3	650	300	3	3.75	101	58	852
115	549.3	650	300	5	7.3	101	58	437
116	549.3	650	300	3	4.5	101	58	926
117	549.3	650	300	3	5.25	101	58	646
118	549.3	650	300	3	5.75	101	58	729
119	549.3	650	300	3	5.5	101	58	631
120	490.5	650	375	2	5.7	82	54	1541
121	490.5	650	375	3	8.5	82	54	1157
122	490.5	650	375	5	14.15	82	54	617

# Num	D <sub>0</sub> [mm]	D <sub>F</sub> [mm]	T [°C]	ω <sub>M</sub> [rad/s]	v <sub>mM</sub> [mm/s]	YS [MPa]	YM [GPa]	FIOT
123	490.5	650	375	2	5.65	82	54	1487
124	490.5	650	375	3	6	82	54	1284
125	490.5	650	375	5	13.7	82	54	561
126	490.5	650	375	2	5.73	82	54	1515
127	490.5	650	375	3	7.6	82	54	1216
128	490.5	650	375	5	14	82	54	621
129	510.9	650	375	3	7.5	82	54	868
130	549.3	650	375	2	2.75	82	54	789
131	549.3	650	375	3	3.75	82	54	625
132	549.3	650	375	5	7.3	82	54	315
133	549.3	650	375	3	4.5	82	54	664
134	549.3	650	375	3	5.25	82	54	477
135	549.3	650	375	3	5.75	82	54	552
136	549.3	650	375	3	5.5	82	54	461
137	490.5	650	450	2	5.7	67	51	1156
138	490.5	650	450	3	8.5	67	51	878
139	490.5	650	450	5	14.15	67	51	460
140	490.5	650	450	2	5.65	67	51	1144
141	490.5	650	450	3	6	67	51	963
142	490.5	650	450	5	13.7	67	51	404
143	490.5	650	450	2	5.73	67	51	1150
144	490.5	650	450	3	7.6	67	51	889
145	490.5	650	450	5	14	67	51	471
146	510.9	650	450	3	7.5	67	51	644
147	549.3	650	450	2	2.75	67	51	561
148	549.3	650	450	3	3.75	67	51	434
149	549.3	650	450	5	7.3	67	51	224
150	549.3	650	450	3	4.5	67	51	469
151	549.3	650	450	3	5.25	67	51	337
152	549.3	650	450	3	5.75	67	51	411
153	549.3	650	450	3	5.5	67	51	330
154	549.3	650	1050	3	5.75	50	108	828
155	549.3	650	1050	3	5.5	50	108	883
156	549.3	650	900	2	2.75	126	129	2422
157	549.3	650	900	3	3.75	126	129	1876
158	549.3	650	900	5	7.3	126	129	999
159	549.3	650	900	3	4.5	126	129	2159
160	549.3	650	900	3	5.25	126	129	1468
161	549.3	650	900	3	5.75	126	129	1394
162	549.3	650	900	3	5.5	126	129	1450
163	550.9	800	980	2	3.60	216	126	25860
164	550.9	800	980	3	5.39	216	126	17480
165	550.9	800	980	5	8.97	216	126	10717
166	550.9	800	1025	2	3.60	187	120	23194

# Num	D <sub>0</sub> [mm]	D <sub>F</sub> [mm]	T [°C]	ω <sub>M</sub> [rad/s]	v <sub>mM</sub> [mm/s]	YS [MPa]	YM [GPa]	FIOT
167	550.9	800	1025	3	5.39	187	120	15563
168	550.9	800	1025	5	8.97	187	120	9569
169	550.9	800	1070	2	3.60	161	100	20470
170	550.9	800	1070	3	5.39	161	100	13837
171	550.9	800	1070	5	8.97	161	100	8607
172	550.9	800	300	2	3.60	101	58	5792
173	550.9	800	300	3	5.39	101	58	4065
174	550.9	800	300	5	8.97	101	58	2475
175	550.9	800	375	2	3.60	82	54	4242
176	550.9	800	375	3	5.39	82	54	3046
177	550.9	800	375	5	8.97	82	54	1872
178	550.9	800	450	2	3.60	67	51	3176
179	550.9	800	450	3	5.39	67	51	2267
180	550.9	800	450	5	8.97	67	51	1408
181	550.9	800	1200	2	3.60	40	84	4159
182	550.9	800	1200	3	5.39	40	84	2833
183	550.9	800	1200	5	8.97	40	84	1880
184	550.9	800	900	2	3.60	126	129	11471
185	550.9	800	900	3	5.39	126	129	7788
186	550.9	800	900	5	8.97	126	129	4882
187	550.9	800	1050	2	3.60	50	108	7036
188	550.9	800	1050	3	5.39	50	108	4711
189	550.9	800	1050	5	8.97	50	108	3064
190	518.9	800	980	3	6.85	216	126	16087
191	518.9	800	980	2	4.88	216	126	22851
192	518.9	800	980	5	12.12	216	126	9510
193	518.9	800	1025	3	6.85	187	120	14343
194	518.9	800	1025	2	4.88	187	120	20551
195	518.9	800	1025	5	12.12	187	120	8421
196	518.9	800	1070	3	6.85	161	100	12766
197	518.9	800	1070	2	4.88	161	100	18296
198	518.9	800	1070	5	12.12	161	100	7556
199	518.9	800	300	3	6.85	101	58	2943
200	518.9	800	300	2	4.88	101	58	4204
201	518.9	800	300	5	12.12	101	58	1732
202	518.9	800	375	3	6.85	82	54	2244
203	518.9	800	375	2	4.88	82	54	3187
204	518.9	800	375	5	12.12	82	54	1287
205	518.9	800	450	3	6.85	67	51	1673
206	518.9	800	450	2	4.88	67	51	2427
207	518.9	800	450	5	12.12	67	51	953
208	575.3	1100	1200	2	4.09	40	84	9721
209	575.3	1100	1200	3	6.10	40	84	7296
210	575.3	1100	1200	5	10.04	40	84	4435

# Num	D <sub>0</sub> [mm]	D <sub>F</sub> [mm]	T [°C]	ω <sub>M</sub> [rad/s]	v <sub>mM</sub> [mm/s]	YS [MPa]	YM [GPa]	FIOT
211	575.3	1100	900	2	4.09	126	129	24579
212	575.3	1100	900	3	6.10	126	129	17360
213	575.3	1100	900	5	4.09	126	129	7022
214	575.3	1100	1050	2	4.09	50	108	15572
215	575.3	1100	1050	3	6.10	50	108	11156
216	575.3	1100	1050	5	10.04	50	108	7017
217	621.6	1100	1200	2	3.11	40	84	9194
218	621.6	1100	1200	3	4.60	40	84	6611
219	621.6	1100	1200	5	7.69	40	84	4363
220	621.6	1100	900	2	3.11	126	129	26723
221	621.6	1100	900	3	4.60	126	129	18621
222	621.6	1100	900	5	7.69	126	129	11802
223	621.6	1100	1050	2	3.11	50	108	15852
224	621.6	1100	1050	3	4.60	50	108	11134
225	621.6	1100	1050	5	7.69	50	108	7179
226	621.6	1100	1200	3	5.50	40	84	6997
227	621.6	1100	900	3	5.50	126	129	18010
228	621.6	1100	1050	3	5.50	50	108	10973
229	668.7	1100	1200	3	5.15	40	84	4701
230	668.7	1100	900	3	5.15	126	129	12729
231	668.7	1100	1050	3	5.15	50	108	7690
232	575.3	1100	980	2	4.09	216	126	56074
233	575.3	1100	980	3	6.10	216	126	36914
234	575.3	1100	980	5	10.04	216	126	22585
235	621.6	1100	980	3	5.50	216	126	38001
236	668.7	1100	980	3	5.15	216	126	25513
237	575.3	1100	1025	2	4.09	187	120	51028
238	575.3	1100	1025	3	6.10	187	120	34401
239	575.3	1100	1025	5	10.04	187	120	19622
240	621.6	1100	1025	3	5.50	187	120	34255
241	668.7	1100	1025	3	5.15	187	120	22684
242	575.3	1100	1070	2	4.09	161	100	47602
243	575.3	1100	1070	3	6.10	161	100	32222
244	575.3	1100	1070	5	10.04	161	100	19622
245	621.6	1100	1070	3	5.50	161	100	31945
246	668.7	1100	1070	3	5.15	161	100	20603
247	621.6	1100	980	2	3.11	216	126	63391
248	621.6	1100	980	3	4.60	216	126	43159
249	621.6	1100	980	5	7.69	216	126	26510
250	621.6	1100	1025	2	3.11	187	120	57643
251	621.6	1100	1025	3	4.60	187	120	38980
252	621.6	1100	1025	5	7.69	187	120	23776
253	621.6	1100	1070	2	3.11	161	100	53141
254	621.6	1100	1070	3	4.60	161	100	36226

# Num	D <sub>0</sub> [mm]	D <sub>F</sub> [mm]	T [°C]	ω <sub>M</sub> [rad/s]	v <sub>mM</sub> [mm/s]	YS [MPa]	YM [GPa]	FIOT
255	621.6	1100	1070	5	7.69	161	100	22366
256	575.3	1100	300	2	4.09	101	58	9625
257	575.3	1100	300	3	6.10	101	58	6787
258	575.3	1100	300	5	10.04	101	58	4064
259	621.6	1100	300	3	5.50	101	58	7357
260	668.7	1100	300	3	5.15	101	58	5364
261	575.3	1100	375	2	4.09	82	54	7096
262	575.3	1100	375	3	6.10	82	54	5002
263	575.3	1100	375	5	10.04	82	54	2985
264	621.6	1100	375	3	5.50	82	54	5322
265	668.7	1100	375	3	5.15	82	54	3876
266	575.3	1100	450	2	4.09	67	51	5239
267	575.3	1100	450	3	6.10	67	51	3671
268	575.3	1100	450	5	10.04	67	51	2188
269	621.6	1100	450	3	5.50	67	51	3815
270	668.7	1100	450	3	5.15	67	51	2769
271	621.6	1100	300	2	3.11	101	58	13867
272	621.6	1100	375	2	3.11	82	54	10192
273	621.6	1100	450	2	3.11	67	51	7468
274	621.6	1100	450	3	4.60	67	51	5254
275	876.2	1400	1200	2	2.56	40	84	8648
276	876.2	1400	1200	3	3.83	40	84	6156
277	876.2	1400	1200	5	6.38	40	84	4056
278	876.2	1400	900	2	2.56	126	129	24123
279	876.2	1400	900	3	3.83	126	129	16818
280	876.2	1400	900	5	6.38	126	129	10666
281	876.2	1400	1050	2	2.56	50	108	14552
282	876.2	1400	1050	3	3.83	50	108	10045
283	876.2	1400	1050	5	6.38	50	108	6499
284	876.2	1400	980	2	2.56	216	126	60460
285	876.2	1400	980	3	3.83	216	126	40873
286	876.2	1400	1025	2	2.56	187	120	53743
287	876.2	1400	1025	3	3.83	187	120	36857
288	876.2	1400	1025	5	6.38	187	120	22444
289	876.2	1400	1070	2	2.56	161	100	48502
290	876.2	1400	1070	3	3.83	161	100	32643
291	876.2	1400	1070	5	6.38	161	100	20622
292	876.2	1400	300	2	2.56	101	58	12083
293	876.2	1400	300	3	3.83	101	58	8267
294	876.2	1400	300	5	6.38	101	58	5130
295	876.2	1400	375	2	2.56	82	54	8909
296	876.2	1400	375	3	3.83	82	54	6194
297	876.2	1400	375	5	6.38	82	54	3890
298	876.2	1400	450	2	2.56	67	51	6560

# Num	D <sub>0</sub> [mm]	D <sub>F</sub> [mm]	T [°C]	ω <sub>M</sub> [rad/s]	v <sub>mM</sub> [mm/s]	YS [MPa]	YM [GPa]	FIOT
299	876.2	1400	450	3	3.83	67	51	4623
300	876.2	1400	450	5	6.38	67	51	2946
301	897.7	1700	1200	2	2.24	40	84	13339
302	897.7	1700	1200	3	3.37	40	84	9212
303	897.7	1700	1200	5	5.67	40	84	6121
304	897.7	1700	900	2	2.24	126	129	37280
305	897.7	1700	900	2	3.37	126	129	26856
306	897.7	1700	900	2	5.67	126	129	16452
307	897.7	1700	1050	2	2.24	50	108	22321
308	897.7	1700	1050	3	3.37	50	108	15506
309	897.7	1700	1050	5	5.67	50	108	9953
310	909.3	1400	980	2	2.55	216	126	64701
311	909.3	1400	980	3	3.82	216	126	43622
312	909.3	1400	980	5	6.35	216	126	25855
313	909.3	1400	1025	2	2.55	187	120	58667
314	909.3	1400	1025	3	3.82	187	120	39087
315	909.3	1400	1025	5	6.35	187	120	23006
316	909.3	1400	1070	2	2.55	161	100	52436
317	909.3	1400	1070	3	3.82	161	100	35513
318	909.3	1400	1070	5	6.35	161	100	20578
319	909.3	1400	300	2	2.55	101	58	11283
320	909.3	1400	300	3	3.82	101	58	7510
321	909.3	1400	300	5	6.35	101	58	4547
322	909.3	1400	375	2	2.55	82	54	8120
323	909.3	1400	375	3	3.82	82	54	5390
324	909.3	1400	375	5	6.35	82	54	3251
325	909.3	1400	450	2	2.55	67	51	5727
326	909.3	1400	450	3	3.82	67	51	3801
327	909.3	1400	450	5	6.35	67	51	2292
328	909.3	1400	1200	2	2.55	40	84	9430
329	909.3	1400	1200	3	3.82	40	84	6981
330	909.3	1400	1200	5	6.35	40	84	4452
331	909.3	1400	900	2	2.55	126	129	26813
332	909.3	1400	900	3	3.82	126	129	18972
333	909.3	1400	900	5	6.35	126	129	11538
334	909.3	1400	1050	2	2.55	50	108	15832
335	909.3	1400	1050	3	3.82	50	108	11598
336	909.3	1400	1050	5	6.35	50	108	7214
337	897.7	1700	980	2	2.24	216	126	96545
338	897.7	1700	980	3	3.37	216	126	62933
339	897.7	1700	1025	2	2.24	187	120	86951
340	897.7	1700	1025	3	3.37	187	120	56328
341	897.7	1700	1025	5	5.67	187	120	34848
342	897.7	1700	1070	2	2.24	161	100	78623



# Num	D <sub>0</sub> [mm]	D <sub>F</sub> [mm]	T [°C]	ω <sub>M</sub> [rad/s]	v <sub>mM</sub> [mm/s]	YS [MPa]	YM [GPa]	FIOT
343	897.7	1700	1070	3	3.37	161	100	51806
344	897.7	1700	1070	5	5.67	161	100	32175
345	897.7	1700	300	2	2.24	101	58	19138
346	897.7	1700	300	3	3.37	101	58	13181
347	897.7	1700	300	5	5.67	101	58	8160
348	897.7	1700	375	2	2.24	82	54	13983
349	897.7	1700	375	3	3.37	82	54	9749
350	897.7	1700	375	5	5.67	82	54	6109
351	897.7	1700	450	2	2.24	67	51	10179
352	897.7	1700	450	3	3.37	67	51	6946
353	897.7	1700	450	5	5.67	67	51	4563
354	944.7	2000	1200	2	2.045	40	84	20284
355	944.7	2000	1200	3	2.915	40	84	14014
356	944.7	2000	1200	5	4.845	40	84	9333
357	944.7	2000	900	2	2.045	126	129	58213
358	944.7	2000	900	3	2.915	126	129	39562
359	944.7	2000	900	5	4.845	126	129	25054
360	944.7	2000	300	2	2.17	101	58	26725
361	944.7	2000	300	3	3.27	101	58	18168
362	944.7	2000	300	5	5.43	101	58	11060
363	944.7	2000	375	2	2.17	82	54	19237
364	944.7	2000	375	3	3.27	82	54	12959
365	944.7	2000	375	5	5.43	82	54	7881
366	944.7	2000	450	2	2.17	67	51	13580
367	944.7	2000	450	3	3.27	67	51	9150
368	944.7	2000	450	5	5.43	67	51	5571
369	944.7	2000	980	2	2.17	216	126	146898
370	944.7	2000	980	3	3.27	216	126	98706
371	944.7	2000	980	5	5.43	216	126	61310
372	944.7	2000	1025	2	2.17	187	120	131404
373	944.7	2000	1025	3	3.27	187	120	89364
374	944.7	2000	1025	5	5.43	187	120	55723
375	944.7	2000	1070	2	2.17	161	100	127616
376	944.7	2000	1070	3	3.27	161	100	84855
377	944.7	2000	1070	5	5.43	161	100	52596
378	944.7	2000	1050	2	2.045	50	108	36431
379	944.7	2000	1050	3	2.915	50	108	23950
380	944.7	2000	1050	5	4.845	50	108	15657



# Appendix 3

Gradient Boosting algorithm defined in section 3.7

```
# -*- coding: utf-8 -*-
"""
@author: Net Shape Manufacturing LABoratory
Sogang University
Seoul, South Korea
Refer to "https://www.kaggle.com/serigne/stacked-regressions-top-4-on-leaderboard/notebook" by Serigne;
"""

import matplotlib.pyplot as plt
import numpy as np
import pandas as pd
pd.set_option('display.float_format', lambda x: '%.3f' % x) #Limiting floats output to 3 decimal points
import seaborn as sns
import warnings
def ignore_warn(*args, **kwargs): pass
warnings.warn = ignore_warn
from scipy.stats import norm, skew
from scipy.special import boxcox1p
from sklearn.metrics import r2_score
from sklearn.externals import joblib
from sklearn.pipeline import make_pipeline
from sklearn.preprocessing import MaxAbsScaler
from sklearn.ensemble import GradientBoostingRegressor
#####
def model_learning():
    print('-'*40)
    print("Train a model for force integral")
    print('-'*40)

    # input data
    column_names = ['D0', 'd0', 's0', 'h0', 'DF', 'dF', 'sF', 'hF', 'T', 'Vs', 'vmM', 'YS', 'YM', 'ENE']
    # read excel file by using pandas module
    rawdata = pd.read_excel('./Database_ALL.xlsx', sheet_name='db global',
                           names = column_names, skipinitialspace=True)
    dataset = rawdata.copy()
    # normally distribution
    dataset['ENE'] = np.log1p(dataset['ENE']) # log1p = log(1+x)
    sns.distplot(dataset['ENE'], fit = norm)
    (mu, sigma) = norm.fit(dataset['ENE'])
    # Skewed features
    numeric_feats = dataset.dtypes[dataset.dtypes != "object"].index
    skewed_feats=dataset[numeric_feats].apply(lambda x:skew(x.dropna())).sort_values(ascending=False)
    print('Skew in numerical features:')
    skewness = pd.DataFrame({'Skew' : skewed_feats})
    print(skewness)
    skewness = skewness[abs(skewness) > 0.750]
    skewness = skewness.dropna()
    skewed_features = skewness.index
```

```

lamd = 0.15
for feat in skewed_features:
    dataset[feat] = boxcox1p(dataset[feat], lamd) # ( x^lamd - 1 ) / lamd
# split the training dataset
train_dataset = dataset.sample(frac=0.8,random_state=0)
test_dataset = dataset.drop(train_dataset.index)

train_labels = train_dataset.pop('ENE')
test_labels = test_dataset.pop('ENE')

# model import
print('model loading!')
# hyperparameters are tuned by using random searching method
GBoost = make_pipeline(MaxAbsScaler(), GradientBoostingRegressor(n_estimators=6902,
learning_rate=0.091, max_depth=2, max_features='sqrt', min_samples_leaf=15, min_samples_split=11,
loss='huber', random_state =5))
# learn the model
print('model learning!')
GBoost.fit(train_dataset,train_labels)
# applicate to the test dataset
# return the ENE value from log scale (np.log1p)
test_labels_G = np.expm1(test_labels.values)
GBoost_pred = np.expm1(GBoost.predict(test_dataset))
# write the data in " ML_results.txt "
f = open('./ML_results.txt','w')
f.write('test_label\n')
for i in range(len(test_labels_G)):
    f.write(str(test_labels_G[i]))
    f.write('\n')
f.write('GBoost_pred\n')
for i in range(len(GBoost_pred)):
    f.write(str(GBoost_pred[i]))
    f.write('\n')
f.write('percenterror\n')
diff = GBoost_pred - test_labels_G
abspercentDiff = np.abs((diff/test_labels_G)*100)
for i in range(len(abspercentDiff)):
    f.write(str(abspercentDiff[i]))
    f.write('\n')
f.close()

# plot the prediction results for the test cases
plt.scatter(test_labels_G, GBoost_pred, label='Gradient Boosting')
plt.xlabel("True Values")
plt.ylabel("Predictions")
plt.axis('equal')
plt.axis('square')
plt.xlim([0,plt.xlim()[1]])
plt.ylim([0,plt.ylim()[1]])
_ = plt.plot([0, 150000], [0, 150000])
plt.show()
# save the learning model
joblib.dump(GBoost, './model.joblib')
print('save done!')

```

```

#####
def predict():
    print('-'*40)
    print('Predict an Energy consumption')
    print('-'*40)
    ""
    input values : D0, d0, s0, h0 / Df, df, sf, hf / T / Vs / vmM / YS / YM
    output value : ENE
    ""

# load the model
print('load the model')
GBoost_model = joblib.load('./model.joblib')

print('Input the parameters!')
# enter the values
D0 = float(input(" D0 value : ")); d0_ = float(input(" d0 value : "));
s0 = float(input(" s0 value : ")); h0 = float(input(" h0 value : "));
DF = float(input(" DF value : ")); dF_ = float(input(" dF value : "));
sF = float(input(" sF value : ")); hF = float(input(" hF value : "));

T = float(input(" T value : ")); Vs = float(input(" Vs value : "))
vmM = float(input(" vmM value : ")); YS = float(input(" YS value : "));
YM = float(input(" YM value : "))
# make pandas dataframe from a dictionary variable
lamd = 0.15
input_dict = {'D0':[boxcox1p(D0,lamd)], 'd0':[boxcox1p(d0_,lamd)], 's0':[s0], 'h0':[boxcox1p(h0,lamd)],
              'DF':[boxcox1p(DF,lamd)], 'dF':[boxcox1p(dF_,lamd)], 'sF':[sF], 'hF':[boxcox1p(hF,lamd)],
              'T':[T], 'Vs':[Vs], 'vmM':[boxcox1p(vmM,lamd)], 'YS':[YS], 'YM':[YM]}

dataset = pd.DataFrame(input_dict)

# predict the ENE
ENE = GBoost_model.predict(dataset)
ENE = np.expm1(ENE)
print("The energy efficiency : %f %(ENE))
#####
if __name__ == "__main__":
    model_learning()
    predict()

```



## References

- [1] J.M. Allwood, A.E. Tekkaya, T.F. Stanistreet. The development of ring rolling technology. *Steel research international* Vol.76 2016, pp 111-120
- [2] E. Eruç, R. Shivpuri. A summary of ring rolling technology - I. Recent trends in machines, processes and production lines. *International Journal of Machine Tools and Manufacture*, 1992, 32:3, 379-398.
- [3] E. Eruç, R. Shivpuri. A summary of ring rolling technology - II. Recent trends in process modeling, simulation, planning, and control. *International Journal of Machine Tools and Manufacture*, 1992, 32:3, 399-413
- [4] G. Zhou, L. Hua, D.S. Qian 3D coupled thermo-mechanical FE analysis of roll size effects on the radial-axial ring rolling process. *Computational Materials Science*, 50, 2011, 911-924
- [5] C.R. Keeton. Ring rolling in: *ASM Metals handbook: forming and forging*. Metals Park, OH:ASM International. 1988, pp 108-127
- [6] N. Kim, S. Machida, S. Kobayashi. Ring rolling process simulation by the three-dimensional finite element method. *International Journal of Machine, Tools and Manufacture* 30:4 (1990), 569-577.
- [7] L. Hua, Z.Z. Zhao. The extremum parameters in ring rolling. *Journal of Materials Processing Technology* 1997; 69:273–6.
- [8] R. Hill, *The Mathematical Theory of Plasticity* (1950), Clarendon Press, Oxford.
- [9] A.G. Mamalis, W. Johnson, J.B. Hawkyard. Pressure distribution roll force and torque in cold ring rolling. *J. Mech. Eng. Sc.* 18:4 (1976), 196-209.
- [10] Quagliato L, Berti GA. Temperature estimation and slip-line force analytical models for the estimation of the radial forming force in the RARR process of flat rings. *Int J Mech Sci* 2017;123.
- [11] Quagliato L, Berti GA, Kim D, Kim N. Slip line model for forces estimation in the radial-axial ring rolling process. *Int J Mech Sci* 2018;138–139:17–33.
- [12] F.L. Yan, L. Hua, Y.Q. Wu. Plannig feed speed in cold ring rolling. *International Journal of Machine Tools & Manufacture*, 47, (2007), 1695-1701.
- [13] Monti M, Berti GA. Design of a flanged ring produced by hot forming using FE analysis. *International Journal of Materials Engineering and Technology*, 2012; 7:1–15.
- [14] L. Guo, H. Yang. Towards a steady forming condition for radial–axial ring rolling. *International Journal of Mechanical Science* 53:4, 2011, 286-299.
- [15] G. Zhou, L. Hua, D.S. Qian. 3D coupled thermo-mechanical FE analysis of roll size effects on the radial–axial ring rolling process. *Computational Materials Science*, 2011;50: 911–24.
- [16] G.A. Berti, L. Quagliato, M. Monti. Set-up of radial–axial ring-rolling process: Process worksheet and ring geometry expansion prediction. *International Journal of Mechanical Science*, 99 (2015), 58-71.
- [17] L. Quagliato, G.A. Berti. Mathematical definition of the 3D strain field of the ring in the radial-axial ring rolling process. *International Journal of Mechanical Science* 115–116, 2016, 746-759.
- [18] J.B. Hawkyard, W. Johnson, J. Kirkland, E. Appleton. Analyses for roll force and torque in ring rolling, with some supporting experiments. *Int. J. Mech. Sci.* 1973, 15, 873–893.
- [19] D.Y. Yang, J.S. Ryoo. An investigation into the relationship between torque and load in ring rolling. Department of Production Engineering, Korea Advanced Institute of Science and Technology
- [20] J. S. Ryoo, D. Y. Yang. The influence of process parameters on torque and load in ring rolling. *Journal of Mechanical Working Technology* 12, 1986, 307-321.
- [21] A. Parvizi, K. Abrinia, M. Salimi. SLAB analysis of ring rolling assuming constant shear friction. *Journal of Materials Engineering and Performance*, 20:9 (2010), 1505-1511.
- [22] A. Parvizi, K. Abrinia. A two dimensional upper bound analysis of the ring rolling process with experimental and FEM verifications. *International Journal of Mechanical Sciences*, 79 (2014), 176-181.

- [23] L. Quagliato, G.A. Berti, D. Kim, N. Kim. Contact geometry estimation and precise radial force prediction for the radial-axial ring rolling process, *International Journal of Material Forming* (2018) 11:789–805
- [24] T. Wang, Q. Wang. Calculation of axial rolling force in radial-axial ring rolling process. *Advanced Materials Research*. 1004-1005 (2014), 1344-1347.
- [25] A. Kalyani, A. Mattika, A. Deshmukh. The effect of force parameter on profile ring rolling process. *International Journal of Engineering Research & Technology* 4:5, 2015, 840-844.
- [26] L. Quagliato, G.A. Berti Statically determinated slip-line field solution for the axial forming force estimation in the radial-axial ring rolling process. *AIP Conference Proceedings*, 190004 (2017), 1896.
- [27] D. Qian, Y. Pan. 3D coupled macro–microscopic finite element modelling and simulation for combined blank-forging and rolling process of alloy steel large ring, *Computational Materials Science*, 70 (2013) 24–36.
- [28] D.S. Qian, G. Zhou, L. Hua, D.F. Shi, H.X. Li. 3D coupled thermomechanical FE analysis of blank size effects on radial-axial ring rolling. *Ironmaking and Steelmaking* 40:5 (2013), 360-368.
- [29] G. Zhuo, L. Hua, J. Lan, D.S. Qian. 3D coupled thermo-mechanical FE modelling and simulation of radial-axial ring rolling. *Materials Research Innovations*, 15, 2011, 221-224.
- [30] Z.W. Wang, J.P. Fan, D.P. Hu, C.Y. Tang, C.P. Tsui. Complete modeling and parameter optimization for virtual ring rolling. *International Journal of Mechanical Sciences* 52, (2010), 1325–1333.
- [31] Z.C. Sun, H. Yang, X.Z. Ou. Thermo-mechanical coupled analysis of hot ring rolling process. *Trans. Nonferrous Met. Soc. China* 18, (2008).
- [32] G. Zhou, L. Hua, J. Lan, D.S. Qian. FE analysis of coupled thermo-mechanical behaviors in radial–axial rolling of alloy steel large ring. *Comp. Mat. Sc.* 50 (2010), 65-76.
- [33] G. Zhou, L. Hua, D. Qian, D. Shi, H. Li. Effects of axial rolls motions on radial–axial rolling process for large-scale alloy steel ring with 3D coupled thermo-mechanical FEA. *International Journal of Mechanical Sciences*, 59 (2012), 1–7
- [34] A. Naizabekov, S. Lezhnev, E. Panin. Study of the influence of the main parameters of “Rolling-ECAP” process on the stress strain state and the microstructure evolution using computer simulation. *Procedia Manufacturing*, 37, (2019), 459-466.
- [35] Z. Pater, J. Tomczak, T. Bulzak, M. Knapinski, S. Sawicki, K. Laber. Determination of the critical damage for 100Cr6 steel under hot forming conditions. *Engineering Failure Analysis* 128 (2021) 105588.
- [36] I.A. Daniyan, K. Mpofo, A.O. Adeodu. Investigating the thermal properties of carbon steel STKM13a for the welding assembly of rail car suspension system. *Procedia CIRP* 81, (2019), 886-891.
- [37] S.A. Jawade, R.S. Joshi, S.B. Desai. Comparative study of mechanical properties of additively manufactured aluminum alloy. *Materials Today: Proceedings*
- [38] I.A. Daniyan, K. Mpofo, A.O. Adeodu, O.L. Rominiyi. Investigation of distortion, stress and temperature distribution during assembly of the suspension system of a rail car. *Procedia Manufacturing* 38 (2019) 1792–1800.
- [39] L. Potgorschek, J. Domitner, F. Honsch, C. Sommitsch, S. Kaufmann. Numerical simulation of hybrid joining processes: self-piecing riveting combined with adhesive bonding. *Procedia Manufacturing* 47 (2020) 413–418
- [40] X. Shu, Y. Chang, Y. Zhu, B. Ye, Z. Li. Production mechanism of residuals stress in spinning of thin wall cone parts with variable section. *Procedia Manufacturing* 50 (2020) 286–290
- [41] N. Lv, D. Liu, Y. Yang, J. Wang. Studying the residual stress homogenization and relief in aerospace rolling ring of GH4169 alloy using ageing treatment. *International Journal of Advanced Manufacturing Technology* (2021) 112:3415–3429
- [42] T. Lim, I. Pillinger, P. Hartley. A finite-element simulation of profile ring rolling using a hybrid mesh model. *Journal of Materials Processing Technology* 80–81 (1998) 199–205.
- [43] K. Davey, M.J. Ward. A practical method for finite element ring rolling simulation using the ALE flow formulation. *International Journal of Mechanical Sciences* 44 (2002) 165–190.
- [44] B. Kim, H. Moon, E. Kim, M. Choi, M. Joun. A dual-mesh approach to ring-rolling simulations with emphasis on remeshing. *Journal of Manufacturing Processes* 15 (2013) 635–643.



- [45] Y. Yea, Y. Ko, N. Kim, J. Lee. Prediction of spread, pressure distribution and roll force in ring rolling process using rigid-plastic finite element method. *J. Mat. Proc. Tech.* 140 (2003), 478-486.
- [46] N. Kim, H. Kim, K. Jin. Optimal Design to Reduce the Maximum Load in Ring Rolling process. *International Journal of Precision Engineering and Manufacturing* 13:10, 2012, 1821-1828.
- [47] A.G. Mamalis, J.B. Hawkyard, W. Johnson. Spread and flow patterns in ring rolling. *International Journal of Mechanical Science.* 18, 1976, 11-16.
- [48] D. Qian, Z. Zhang, L. Hua: An advanced manufacturing method for thick-wall and deep-groove ring – Combined ring rolling. *J Mater Process Technol* 2013; 213:1258-67.
- [49] L. Hua, D.S. Qian, L.B. Pan. Deformation behaviors and conditions in L-section profile cold ring rolling. *Journal of Materials Processing Technology* 209 (2009) 5087–5096.
- [50] K.H. Kim, H.G. Suk, M.Y. Huh. Development of the profile ring rolling process for large slewing rings of alloy steels. *J Mater Process Technol* 2007;187–188:730–3.
- [51] K. Davey, M.J. Ward. The practicalities of ring rolling simulation for profiled rings. *Journal of Materials Processing Technology* 125–126 (2002) 619–625.
- [52] C.J. Cleaver, J. Allwood. Incremental profile ring rolling with axial and circumferential constraints. *CIRP Annals - Manufacturing Technology* 66 (2017) 285–288
- [53] C.J. Cleaver, J.M. Allwood. Incremental ring rolling to create conical profile rings. *Procedia Engineering* 207 (2017) 1248–1253.
- [54] C.J. Cleaver, J. Lohmar, S. Tamimi. Limits to making L-shape ring profiles without ring growth. *Journal of Materials Processing Tech.* 292 (2021) 117062
- [55] C.J. Cleaver, M. R. Arthington, S. Mortazavi, J.M. Allwood. Ring rolling with variable wall thickness. *CIRP Annals - Manufacturing Technology* 65 (2016) 281–284.
- [56] I.Y. Oh, TW Hwang, YY Woo, HJ Yun, YH Moon. Analysis of defects in L-section profile ring rolling. *Procedia Manufacturing* 15 (2018) 81–88
- [57] M. Park, C. Lee, J. Lee, I. Lee, M. Joun, B. Kim, et al. Development of L-sectioned ring for construction machines by profile ring rolling process. *International Journal of Precision Engineering and Manufacturing* 2016; 17:233–40.
- [58] K.H. Lee, D. C. Ko, D.H. Kim, S.B. Lee, N.M Sung, B.M. Kim. Design method for intermediate roll in multi-stage profile ring rolling process: The case for excavator idler rim. *International Journal of Precision Engineering and Manufacturing.* 15 (2014), 503-512
- [59] D. Kim, L. Quagliato. Integrated analytical approach for the definition and the control of the radial-axial ring rolling process. *J. Korean Soc. Precis. Eng.*, 36 (2019), No. 9, pp. 821-835
- [60] L. Liang, L. Guo, Z. Liu, P. Wang, H. Zhang. On a precision forming criterion for groove-section profiled ring rolling process. *J Mater Process Technol* 2021; article in press. doi.org/10.1016/j.jmatprotec.2021.117207
- [61] K. Tani, S. Ishigai, T. Sato, Y. Tsumori. The evolution of near-net-shape ring-rolling processes for large rings made of Ti-6Al-4V. *Kobelco Technology Review* 2005; 26:43–8.
- [62] X. Li, L. Guo, L. Liang, W. Yang. Motion control of guide rolls in intelligent simulation for profiled ring rolling process. *Procedia Manufacturing*, 15 (2018) 97-104.
- [63] J.H. Kang, Research on filling limit of profile ring rolling on circumferential surface. *International Journal of Emerging Technology and Advanced Engineering* 2014; 12:40–5.
- [64] M. Roesch, M. Lukas, C. Schultz, S. Braunreuther, G. Reinhart. An approach towards a cost-based production control for energy flexibility. *Procedia CIRP* 79 (2019) 227–232
- [65] U. Unver, O. Kara. Energy efficiency by determining the production process with the lowest energy consumption in a steel forging facility. *Journal of Cleaner Production* 215, 2019, 1362-1370.
- [66] M. Messner, L. Massalski, A. Wirtz, P. Wiederkehr, J. Myrzik. Representation of energy efficiency of energy converting production processes by process status indicators. *Procedia CIRP* 79, 2019, 221-226.

- [67] A. Hasanbeigi, C. Menke, A. Therdyothin. The use of conservation supply curves in energy policy and economic analysis: The case study of Thai cement industry. *Energy Policy* 38, 2010, 392-405.
- [68] J. Larkiola, P. Myllykoski, A. S. Korhonen, L. Cser. The role of neural networks in the optimization of rolling processes. *Journal of Materials Processing Technology* 80-81, 1998, 16-23.
- [69] L. Giorleo, E. Ceretti and C. Giardini. Energy consumption reduction in ring rolling geometry: a FEM Analysis. *International Journal of Mechanical Sciences*. 2013, Vol.74 pp. 55-64
- [70] Z. Xinglin, L. Dong, Y. Yanhui, H. Yang, Z. Yong. Optimization on cooperative feed strategy for radial-axial ring rolling process of Inco718 alloy by RSM and FEM. *Chin. J. Aeronaut.* 2016, 29, 831-842.
- [71] G. Allegri, L. Giorleo, E. Ceretti, C. Giardini, Driver roll speed influence in Ring Rolling process, *Procedia Engineering* 207, 2017, 1230-1235.
- [72] V. J. Mawson, B. R. Hughes. Deep learning techniques for energy forecasting and condition monitoring in the manufacturing in the manufacturing sector. *Energy & Buildings* 217 (2020) 109966.
- [73] D. Tan, M. Suvarna, Y.S. Tan, J. Li, X. Wang. A three-step machine learning framework for energy profiling, activity state prediction and production estimation in smart process manufacturing. *Applied Energy* 291 (2021) 116808
- [74] T. T. Nguyen Prediction and optimization of machining energy, surface roughness, and production rate in SKD61 milling. *Measurement* 136 (2019) 525-544
- [75] M. Brillinger, M. Wuwer, M.A. Hadi, F. Haas. Energy prediction for CNC machining with machine learning. *CIRP Journal of Manufacturing Science and Technology* 35 (2021) 715-723
- [76] Z. Geng, H. Li, Q. Zhu, Y. Han. Production prediction and energy-saving model based on Extreme Learning Machine integrated ISM-AHP: Application in complex chemical processes. *Energy* 160 (2018) 898-909
- [77] Y. Wang, J. Liu, Y. Han Production capacity prediction of hydropower industries for energy optimization: Evidence based on novel extreme learning machine integrating Monte Carlo. *Journal of Cleaner Production* 272 (2020) 122824
- [78] S. Bruschi, S. Casptto, T. Dal Negro, P.P. Bariani. Real-time prediction of geometrical distortions of hot-rolled steel rings during cooling. *CIRP Annals - Manufacturing Technology* 54(1):229-232.
- [79] J. Bergstra, Y. Bengio. Random search for hyper-parameter optimization. *Journal of Machine Learning Research* 13 (2012) 281-305
- [80] C.C. Chang, C.J. A Lin. Library for Support Vector Machines. *ACM Trans. Intell. Syst. Technol.* 2019, article 27.
- [81] Z. Liu, Y. Guo. A hybrid approach to integrate machine learning and process mechanics for the prediction of specific cutting energy. *CIRP Annuals* 2018, 67, 57-60.
- [82] A. Torres-Barrán, Á. Alonso, J.R. Dorrnsoro. Regression tree ensembles for wind energy and solar radiation prediction. *Neurocomputing* 2019, 326-327, 151-160.
- [83] W. Zhang, C. Wu, H. Zhong, Y. Li, L. Wang. Prediction of undrained shear strength using extreme gradient boosting and random forest based on Bayesian optimization. *Geosci. Front.* 2021, 12, 469-477
- [84] J. Stanke, A. Feuerhack, D. Trauth, P. Mattfeld, F. Klocke. A predictive model for die roll height in fine blanking using machine learning methods. *Procedia Manuf.* 2018, 15, 570-577.
- [85] O.A. Olanrewaju, A.A. Jimoh, P.A. Kholopane. Integrated IDA-ANN-DEA for assessment and optimization of energy consumption in industrial sectors. *Energy* 2012, 46, 629-635.
- [86] L.G.B. Ruiz, R. Rueda, M.P. Cuéllar, M.C. Pegalajar. Energy consumption forecasting based on Elman neural networks with evolutive optimization. *Expert Syst. Appl.* 2018, 92, 380-389.
- [87] T. Tieleman, G. Hinton. Lecture 6.5-rmsprop: Divide the gradient by a running average of its recent magnitude. COURSERA Neural Netw. Mach. Learn. 2012, 4, 26-31.
- [88] A. Hensel, T. Spittel, Kraft und Arbeitsbedarf bildsamer formgebungsverfahren (1st edition), Deutscher Verlag für Grundstoffindustrie, Leipzig, 1978 (in German language).

- [89] R. Storn, K. Price. Differential Evolution – A Simple and Efficient Heuristic for Global Optimization over Continuous Spaces, *Journal of Global Optimization* 11: 341–359, 1997
- [90] A. C. Biju, T. Aruldoss, A. Victoire, K. Mohanasundaram. An Improved Differential Evolution Solution for Software Project Scheduling, Problem, *The scientific World Journal* Volume, 2015
- [91] S. Sen, A Survey of Intrusion Detection Systems Using Evolutionary Computation, *Bio-Inspired Computation in Telecommunications*, 2015